Analysis of the Global Spectrum of the Atmospheric Horizontal Kinetic Energy from the Boundary Layer to the Mesopause

Dissertation
zur Erlangung des Grades
doctor rerum naturalium (Dr. rer. nat.)

an der Mathematisch-Naturwissenschaftlichen Fakultät
der Universität Rostock

erstellt am
Leibniz-Institut für Atmosphärenphysik, Kühlungsborn

Rostock, 2012

vorgelegt von:
Sebastian Brune
aus Ludwigslust

urn:nbn:de:gbv:28-diss2012-0082-2

Gutachter:

Prof. Dr. Erich Becker,
Leibniz-Institut für Atmosphärenphysik, Kühlungsborn

Prof. Dr. Volkmar Wirth,
Institut für Physik der Atmosphäre, Universität Mainz

Datum der Einreichung: 30.01.2012
Datum der Verteidigung: 20.04.2012

Abstract

This thesis substantially contributes to the ongoing discussion, how the large-scale and mesoscale (scales < 500 km) atmospheric motions interact and how the vertical coupling of the atmosphere is influenced by mesoscale waves. For this purpose a mechanistic general circulation model (GCM) with high horizontal and very high vertical resolution covering the atmosphere from the boundary layer up to the lower thermosphere (105 km height) has been run and the simulated spectral kinetic energy budget has been analyzed. The main results are twofold. Firstly, the thesis shows that in our GCM the mesoscale upper tropospheric kinetic energy spectrum can be explained by stratified turbulence. This is only possible due to the presence of both a horizontal cascade of kinetic energy in the upper troposphere and a mesoscale vertical pressure flux convergence that originates in the mid troposphere and contributes to the mesoscale adiabatic conversion in the upper troposphere. Secondly, in our GCM the mesoscale energy deposition in the upper mesosphere can be explained by the damping or breaking of upward propagating gravity waves originating from the troposphere. We show that in this case the vertical pressure flux carried by these waves from the troposphere to the mesosphere is first converted into kinetic energy of the gravity waves and then dissipated, heating the mean flow in the upper mesosphere.

Zusammenfassung

Diese Arbeit trägt zu einem wesentlich verbesserten Verständnis der Zusammenhänge zwischen großräumigen und mesoskaligen (Skalen < 500 km) Bewegungen in der Atmosphäre bei. Ebenso steht die vertikale Kopplung von der Grenzschicht bis zur unteren Thermosphäre (105 km Höhe) durch mesoskalige Wellen (Schwerewellen) im Vordergrund. Dazu wurde ein mechanistisches globales Zirkulationsmodell (GCM) der Atmosphäre mit hoher horizontaler und sehr hoher vertikaler Auflösung unter dem Gesichtspunkt des spektralen Budgets der horizontalen kinetischen Energie analysiert. Die Ergebnisse können in zwei Punkten zusammengefaßt werden: Erstens wird gezeigt, daß die mesoskalige Energiekaskade in der oberen Troposphäre wesentlich auf geschichtete Turbulenz (*stratified turbulence*) zurückzuführen ist. Hierbei wird die Energiekaskade von den großen Skalen zu den Mesoskalen innerhalb der oberen Troposphäre wesentlich durch eine positive vertikale Druckflußkonvergenz in den Mesoskalen selbst verstärkt, die ihren Ursprung in der mittleren Troposphäre hat und über adiabatische Konvertierung die mesoskalige kinetische Energie in der oberen Troposphäre erhöht. Zweitens wird die Energiedeposition durch troposphärische Schwerewellen in der oberen Mesosphäre genauer beschrieben. Der durch diese mesoskaligen Wellen nach oben transportierte Druckfluß wird bei der Dämpfung oder beim Brechen der Wellen in der Mesosphäre zuerst in kinetische Energie der Wellen umgesetzt und dann dissipiert, das heißt, in Wärme des Grundstroms umgewandelt.

Contents

1 Introduction

So, naturalists observe, a flea
Has smaller fleas that on him prey;
And these have smaller still to bite 'em;
And so proceed ad infinitum.

– Jonathan Swift

Big whirls have little whirls that feed on their velocity,
and little whirls have lesser whirls and so on to viscosity.

– Lewis Fry Richardson

The last short poem (Richardson 1922), which is well known also outside the natural sciences, summarizes some of the meteorological work of Lewis Fry Richardson. It illustrates with only a few words firstly that in general atmospheric effects of very different temporal and spatial dimensions are linked to each other, and secondly that the processes behind this interaction may hold true over large ranges. Atmospheric motions span from the global flow patterns in the middle atmosphere (MA, that is stratosphere and mesosphere, 15 km to 95 km height) with a persistence of months or even years down to small turbulent events like the flow around a butterfly's wing with a duration of only some milliseconds. But still, one could argue that almost the same physical laws are determining the motions on either side of this scale range. Analyzing the spectrum of the kinetic energy (KE) of the atmosphere (or parts thereof) is a reasonable measure when looking for physical regimes that dominate greater parts of the motions.

The mesoscales in the upper troposphere and lower stratosphere (UTLS) contain amongst other entities also gravity waves (GWs). It is generally understood that tropospheric GWs play an important role for the global circulation of the MA (Andrews et al. 1987). The mesospheric residual circulation is mainly driven by upward propagating GWs generated in the troposphere and their interaction with the mean flow due to damping and breaking (Dunkerton 1979; Lindzen 1981). This leads to well known phenomena such as large-scale upwelling and downwelling in the MA and the very cold summer mesopause. The global analysis of the spectral horizontal KE may give insight in the generation of GWs in the UTLS region, their propagation through the MA, and their breaking and interaction with the mean flow in the mesosphere. The focus of this study is

therefore mainly on the KE cascades in the upper troposphere, as well as on the energetics of GW breaking in the mesosphere. For this purpose we shall use a mechanistic global circulation model that is designed to properly simulate both processes. Such a comprehensive analysis has not been done previously.

The spectral KE of the atmosphere and especially of the upper troposphere has been discussed since many years. Based upon the pioneering work of Kolmogorov (1941) and building on decades of observational, numerical, and theoretical studies of the atmosphere's KE spectrum, there have been many attempts to attribute particular physical processes to the different parts of the spectrum. In analogy to the three-dimensional turbulent flow occurring at small-scales down to Kolmogorov's micro scale, the term "macroturbulence" has been coined for the description of the atmospheric KE spectrum for substantially larger scales, that is for horizontal wavelengths considerably larger than the Ozmidov scale, which is of the order of just a few meters in the upper troposphere.

The theories and concepts that have been used to explain the macroturbulent horizontal kinetic energy spectrum in the troposphere usually rely on identifying different spectral regimes and applying the concepts of energy and enstrophy (squared vorticity) cascades based on the same kind of similarity analysis as done by Kolmogorov. In this sense the following spectral regimes can be distinguished in the spectrum, see Fig. 1.

The injection range consists of the scales where the main KE input into the spectrum occurs. For the upper troposphere these are the baroclinic scales ($5 \leq n \leq 10$), where KE is generated by the conversion of available potential energy. Furthermore, there is at least one dissipation range where KE is decreased. In the real atmosphere the dissipation is ultimately realized at the molecular scale, i.e. for very large n. However, a global model does not cover these scales. It rather mimicks them by damping the smallest resolved scales, which depends on the model resolution.

If the injection and the dissipation ranges are separated well enough, an inertial range develops in between them. Here, KE is transferred through the inertial scales from the injection range toward the dissipation range. In the upper troposphere the planetary scales ($1 \leq n < 5$) on one side and the synoptic and subsynoptic scales ($10 < n \leq 80$), as well as the mesoscales ($n > 80$), on the other side form two separate inertial ranges. In such a range the spectrum theoretically

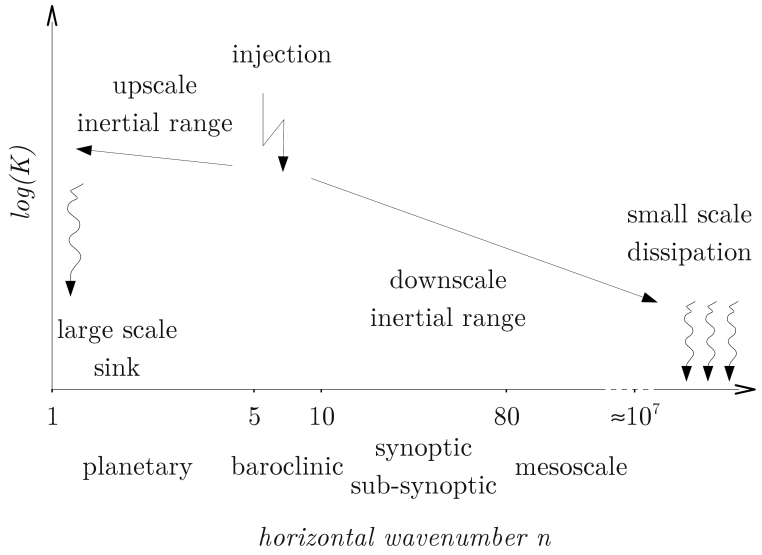

Fig. 1: General concept of cascades in the atmospheric KE spectrum: Inertial ranges occur if injection and dissipation ranges are well separated. The schematic shows a double logarithmic plot of kinetic energy K vs total wavenumber n. The slope $\Delta log(K)/\Delta log(n)$ is constant over the inertial range in n. For orientation some of the atmospheric scales are given.

assumes a robust slope depending on the transferred quantity but independent of the direction. Following Kolmogorov (1941) and Kraichnan (1967), the atmospheric KE spectrum assumes a n^{-3} slope ("the -3 regime") with respect to the total wavenumber n where the enstrophy cascade is dominating and a $n^{-5/3}$ slope ("the -5/3 regime") where the kinetic energy cascade is dominating.

Comprehensive observational evidence of the spectral regimes in the upper troposphere has been found in both global assimilated datasets starting with the work of Boer and Shepherd (1983) and in wind data obtained during aircraft flights (Nastrom et al. 1984; Nastrom and Gage 1985).

It was not before the 1980's that, while taking advantage of the development of computational resources, the *global* KE spectrum for the planetary and larger synoptic scales in the *real* troposphere could been considered by Boer and Shepherd (1983). They performed an analysis on the basis of globally assimilated data with a triangular spectral truncation at total wavenumber $n = 32$ (T32), equivalent to 1250 km horizontal wavelength. They found that kinetic energy is injected at the baroclinic scale and identified two cascades: An inverse kinetic energy cascade transferring KE to larger scales (smaller wavenumbers), in this

case to the planetary scales; and a forward enstrophy cascade transferring enstrophy to smaller scales (larger wavenumbers), here to the synoptic scales. In their analysis the latter is related to a slope of -3, whereas the KE spectrum in the planetary scale does not show the expected -5/3 slope due to the dominance of particular quasi-stationary waves.

At the same time the analysis of wind data from the UTLS obtained by aircraft measurements during the 1970s (Nastrom et al. 1984; Nastrom and Gage 1985) was a milestone since also the smaller horizontal scales with wavelengths between 500 km and 1 km ($n > 80$), the mesoscales, could be considered in terms of global macroturbulence. The analysis confirmed the synoptic and sub-synoptic -3 regime and revealed a robust slope close to -5/3 for the mesoscale part of the spectrum.

The purpose of the present study is to test the existing theories and concepts to explain the observations by analyzing the dynamics of a general circulation model (GCM) with idealized differential heating and very high spatial resolution. In particular, we will test the concept of stratified turbulence (Waite and Bartello 2004; Lindborg 2006) for the mesoscales. This concept and three others shall be shortly outlined in the following.

The classical 2D turbulence theory was developed by Kraichnan (1967). It proposes two separated inertial ranges: an upscale energy cascade with a -5/3 slope for scales larger than the injection range and a downscale enstrophy cascade with a -3 slope for scales smaller than the injection range (Fig. 2a).

The work of Kraichnan (1967) relies on the same dimensional arguments, only in two dimensions, as the ideas of Kolmogorov (1941) with regard to three-dimensional turbulence. In the latter, enstrophy is not a conserved quantity and only KE may be cascaded through the spectrum. This gives rise to the well-known -5/3 slope together with a downscale kinetic energy cascade for scales smaller than the injection range (Fig. 2b).

However, Kolmogorov's classical turbulence theory does not cover adequately the atmospheric flow at scales larger than a few kilometers. Here typical aspect ratios of horizontal to vertical length scale of larger than 100 violate the assumption of a homogeneous and isotropic flow, which is mandatory for applying the 3D turbulence theory. On the other side, the divergent flow does play an impor-

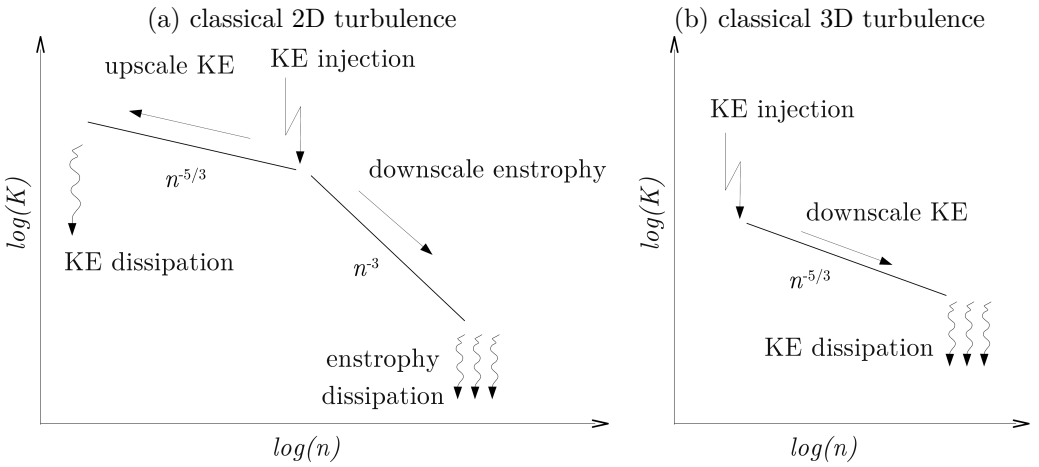

Fig. 2: Kinetic energy and enstrophy cascades in (a) classical 2D turbulence theory after Kraichnan (1967) and (b) classical 3D turbulence theory after Kolmogorov (1941).

tant role not only in the mesoscales, thus a strictly 2D approach is not advisable either.

The quasi-geostrophic (QG) theory allows for divergent modes. In the context of macroturbulence it has been discussed heavily by Tung and Orlando (2003) or Gkioulekas and Tung (2007). In contrast to classical 2D turbulence theory the authors showed that double cascades of both enstrophy and energy develop on either side of the KE injection range. Within these double cascades, one dominates over the other. In this sense not only the downscale enstrophy cascade in the sub-synoptic and larger mesoscales is accompanied by a "hidden" downscale energy cascade, see Fig. 3a, but also the upscale energy cascade at planetary scales goes along with a "hidden" upscale enstrophy cascade.

Depending on the dissipation, any "hidden" cascade may become dominant in another scale range. In the case of QG turbulence, Gkioulekas and Tung (2007) showed that in their two-layer QG model the downscale energy cascade dominates over the enstrophy cascade if the imbalance of the enstrophy accumulation in each layer is sufficiently large enough.

Based on the QG theory the concept of surface quasi-geostrophic (SQG) turbulence (Blumen 1978; Held et al. 1995) was recently incorporated into a numerical model of the tropopause by Tulloch and Smith (2009), which also showed the -5/3 slope for the mesoscales. As already discussed by Gkioulekas and Tung

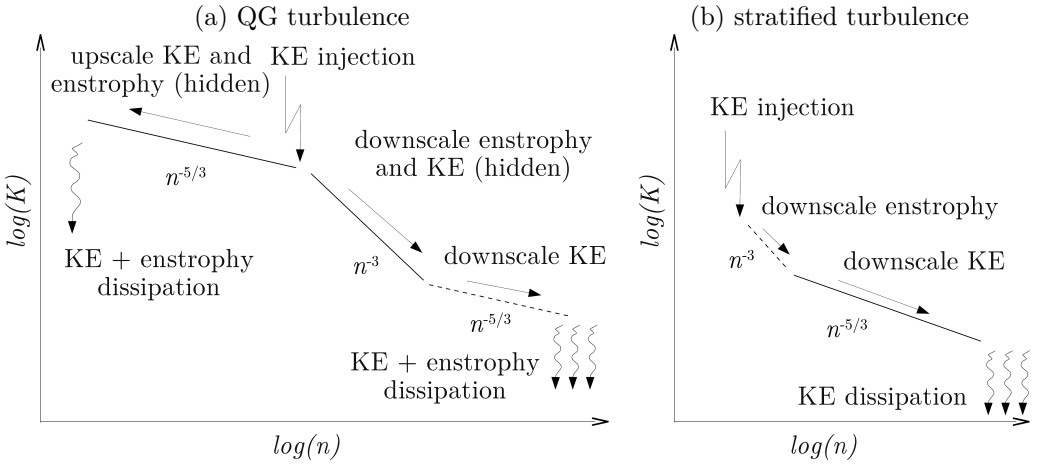

Fig. 3: Kinetic energy and enstrophy cascades in (a) quasi-geostrophic theory after Tung and Orlando (2003) and Gkioulekas and Tung (2007) and (b) stratified turbulence theory (Lindborg 2006).

(2007), SQG turbulence can be considered as an extreme case of QG turbulence, where the downscale energy cascade dominates the whole spectrum, especially also the larger scales. It remains questionable, whether SQG turbulence can actually be applied to the upper troposphere (Lindborg 2009).

All concepts based on QG theory suffer from the fact, that the QG approximation does not hold true for scales smaller than some hundred kilometers wavelength. This means that these concepts struggle to explain the KE spectrum for the smaller scales.

As illustrated in Fig. 3b, the concept of stratified turbulence produces a downscale energy cascade with a -5/3 slope for scales smaller than the injection range (Lindborg 2006). It hereby requires a strongly stratified background, which is much closer to the real atmosphere than the requirement of homogeneity and isotropy in classical 3D turbulence and does not represent a constraint in spatial scaling beforehand. Also inertial and buoyancy forces should be of the same order of magnitude.

It turns out that with the use of dedicated models like the two-layer QG model of Tung and Orlando (2003) or the box model of Lindborg (2006), scaling properties of the spectrum can be better interpreted than when analyzing "real" data. On the other hand, the applicability of strongly idealized models to the real atmosphere is very limited.

Our approach of using a mechanistic GCM compromises between the two worlds: The model is simple enough to allow for straightforward interpretations, but also comprehensive enough to apply these interpretations to the real atmosphere.

In the last decade parts of the mesoscales could already be included in GCM simulations. Using the SKYHI GCM, Koshyk et al. (1999b) and Koshyk and Hamilton (2001) identified the transition to a shallower slope in the mesoscales and they related this to an increasing importance of non-rotational modes, such as (among others) gravity waves. Later results from the AFES GCM (Takahashi et al. 2006; Hamilton et al. 2008) confirmed the transition within the KE spectrum, even when the GCM is run in dry mode.

In the present study we tackle the tropospheric macroturbulence with a GCM setup consisting of a horizontal resolution of T330 (equivalent wavelength 120 km or grid spacing 60 km), which covers the QG motion (planetary, synoptic and sub-synoptic scales), as well as the large-scale part of the mesoscales, where QG scaling does not apply. We also apply a very high vertical resolution with a vertical level spacing of 250 m in the UTLS. Furthermore, the subgrid-scale parameterization has been designed to evaluate the role of both the QG and the stratified turbulence in shaping the global horizontal KE spectrum in the troposphere. With our analysis we assess the energy and enstrophy cascades in the UTLS region and look for evidence of an energy transfer from baroclinic waves through the synoptic scales toward the mesoscales. We reinforce the hypothesis that within this energy cascade toward and through the mesoscales vertically propagating GWs are generated.

From the KE perspective the middle atmosphere differs substantially from the UTLS due to the absence of KE input into the spectrum in a narrow scale range as it happens due to baroclinic waves in the troposphere. Instead, the energetics of upward propagating waves become important, both on the large and the small-scale side of the KE spectrum. The role of planetary waves in the stratosphere has been described extensively, see Andrews et al. (1987). Therefore our focus in the MA lies on the mesoscales. This is motivated by the importance of momentum deposition of mesoscale waves in the MA, which has a large impact on the global-scale residual meridional circulation in the MA. The breaking of GWs has been studied in detail on a local scale both numerically (Achatz 2007;

Fritts et al. 2009) and especially in the mesosphere also experimentally (Hecht et al. 2000; Rapp et al. 2004; Goldberg et al. 2006; Li et al. 2007). Regarding the global picture of mesospheric GWs, however, there are only some data derived from satellites (Preusse et al. 2006; Wu et al. 2006) and a few GCM results, namely from the SKYHI model (Koshyk and Hamilton 2001) and recently from an improved version of the CCSR/NIES AGCM (Watanabe et al. 2008). Alexander et al. (2010) summarize a great part of the observational and modeling efforts to achieve a global picture of middle atmospheric GWs. We also note that up to now GCM simulations with a very high spatial resolution do usually not resolve the upper mesosphere but focus on the layers below.

In this study the whole atmosphere up to the lower thermosphere is simulated with a mechanistic GCM using both relatively high horizontal resolution (T210 spectral truncation corresponding to an horizontal equivalent wavelength of 190 km or grid spacing 95 km) *and* high vertical resolution (model level interval about 600 m). Furthermore we do not apply any GW parameterization. Instead, GWs are explicitly simulated at all model levels. These two conditions, very high spatial resolution and explicit GW simulation up to the lower thermosphere, are being fulfilled for the first time within a single GCM (Becker 2009). This setup allows to study GW generation in the UTLS, GW propagation through the MA, and GW-mean flow interaction in the upper mesosphere. We will test and analyze a simplified GW kinetic energy budget for the mesosphere, which subsequently will be used to illuminate the interaction of GWs with the mean flow at that height, and especially the process of frictional heating in that region, which in conventional models is parameterized in terms of an energy deposition due to GWs.

The outline of this thesis is as following: In Chapter 2 the model will be described with emphasis on the vertical discretization and the diffusion scheme. Our analysis of the spectral kinetic energy, the spectral KE budget, and the energy and enstrophy fluxes through the spectrum will be introduced in Chapter 3. Here, we will already present some examples to familiarize the reader with the tools used in the analysis. In this chapter we also address the averaging in time and space. We will present the results of our interpretation together with a discussion in Chapter 4 and conclude this study with a summary in Chapter 5.

2 Model description

2.1 Model setup

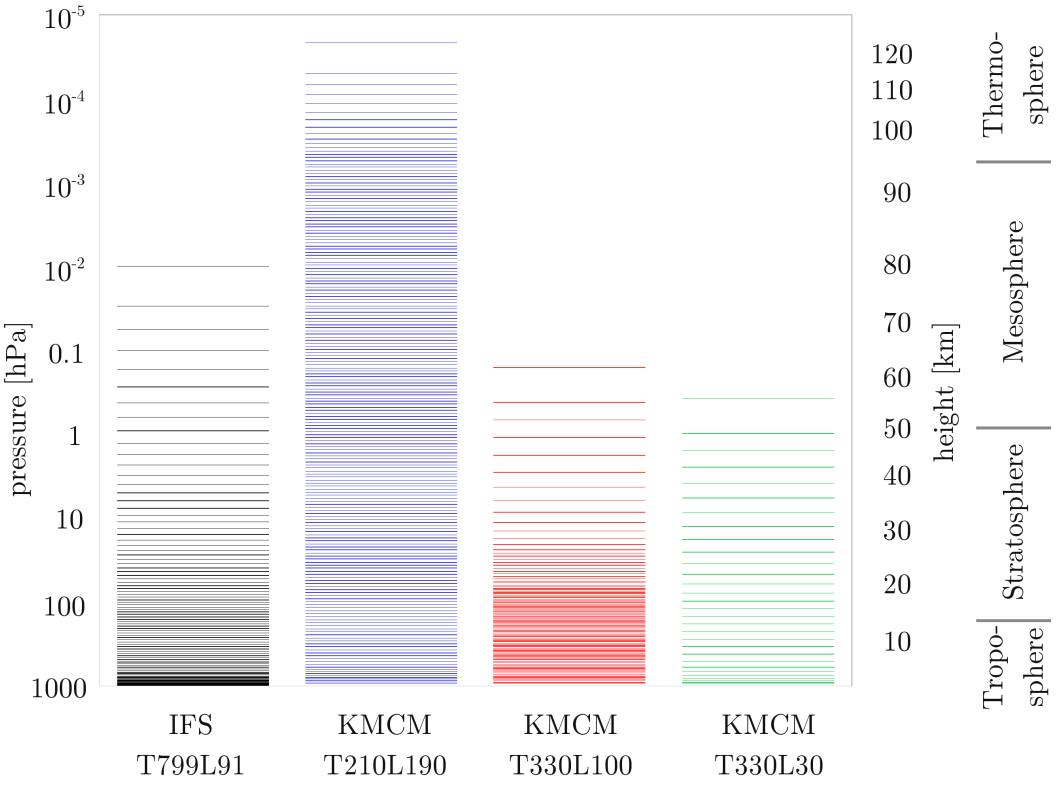

Fig. 4: Model levels of ECMWF IFS L91, KMCM L190, L100 and L30 setups (from left to right).

Our analysis is based on results of the KMCM (Kühlungsborn Mechanistic Circulation Model, Becker (2003)). The model consists of a standard spectral dynamical core. We assume permanent January conditions. In the tropics latent heating is prescribed, in mid latitudes condensational heating is self-induced. Radiative heating is parameterized by temperature relaxation, the surface temperature is prescribed everywhere (see Körnich et al. (2006) for details).

This study relies on a sufficient model resolution both in the upper troposphere and the middle atmosphere. Accordingly the model was run in different spatial resolutions (see Fig. 4, for comparison the model levels of the global weather forecast model IFS L91 are also displayed). The macroturbulence in the UTLS region has been simulated using a spectral truncation of T330 (minimum

equivalent wavelength 120 km or 60 km grid spacing) and 100 vertical hybrid levels up to the stratopause corresponding to a vertical level spacing of 250 m up to 100 hPa ($\approx$ 15 km). Some of the earlier work on macroturbulence in the upper troposphere has been based on GCM simulations with a much coarser vertical resolution. Therefore the KMCM has been run with T330 but only 30 vertical hybrid layers up to the stratopause as well. This corresponds to a vertical level spacing of about 1300 m. For the continuous analysis from the boundary layer up to the lower thermosphere ($2 \cdot 10^{-5}$ hPa or 125 km) we applied a horizontal spectral resolution of T210 and 190 vertical hybrid levels corresponding to a minimum equivalent wavelength of 190 km or 95 km horizontal grid spacing and an approximate vertical level spacing of 600 m up to $3 \cdot 10^{-4}$ hPa ($\approx$ 105 km).

The vertical discretization is defined within an η-coordinate (hybrid) terrain-following system (Simmons and Burridge 1981). The vertical coordinate fulfills:

$$\begin{aligned} &\eta \, \epsilon \, (0,1)\,, \\ &\eta = 1 \text{ for } p = p_s\,, \\ &\eta = 0 \text{ for } p = 0\,, \\ &\dot{\eta} = 0 \text{ for } \eta = 0,1\,. \end{aligned} \tag{1}$$

The pressure p on each level can be computed from the surface pressure p_s and the vertical coordinate as:

$$p(\lambda, \phi, \eta, t) = a(\eta) + b(\eta) p_s(\lambda, \phi, t)\,. \tag{2}$$

The two coefficients a and b are defined as:

$$\begin{aligned} a(\eta) &= \eta(1-\eta) p_{00}\,, \\ b(\eta) &= \eta^2\,, \end{aligned} \tag{3}$$

where p_{00} is the mean surface pressure at sea level, i.e. $p_{00} = 1013$ hPa.

For reference the zonally averaged zonal winds and temperatures are shown for the T210L190 and T330L100 runs in Fig. 5. The simulated stratospheric and tropospheric jets can be seen in Figs.5a and 5c, respectively. In Fig. 5b the cold summer mesopause, here under permanent January conditions over the antarctic region is well captured at about 0.001 hPa (90 km).

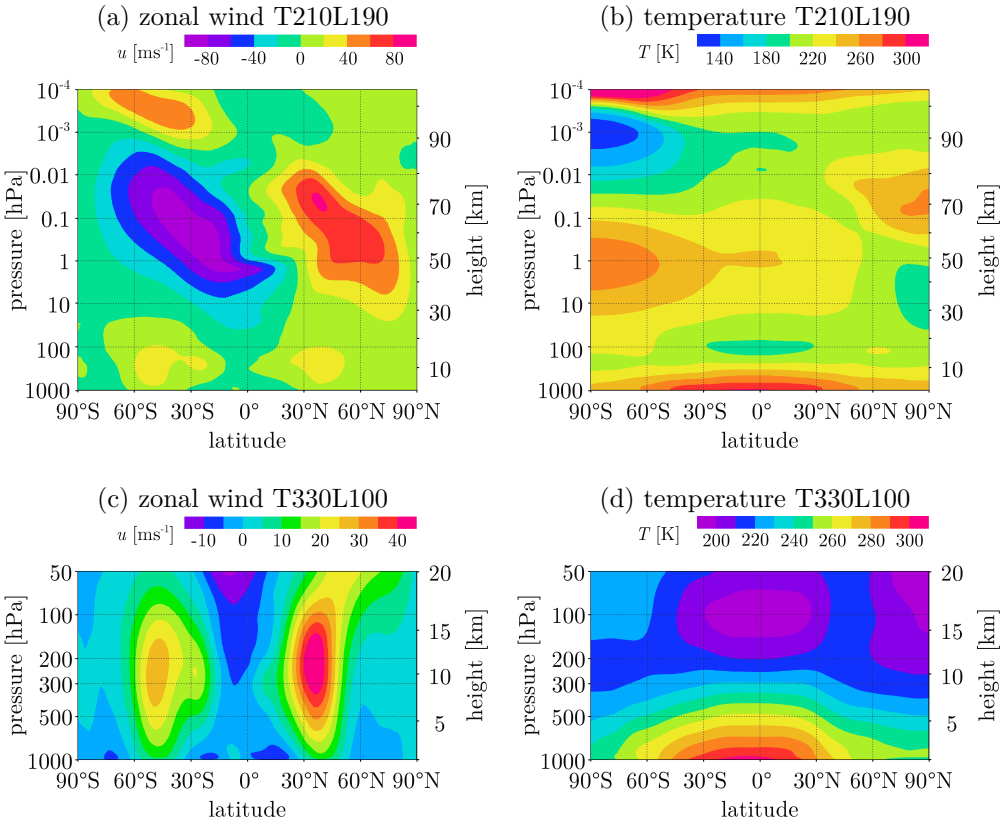

Fig. 5: Vertical cross section of zonally averaged zonal wind u (left panel) and temperature (right panel) from the T210L190 run, averaged over 16 model days (a,b), and of the T330L100 run, averaged over 17 model days (c,d).

2.2 Prognostic equations for vorticity and divergence

The primitive equations form the basis of our model. In this study the prognostic equations for vorticity ξ and divergence δ are used to perform the analysis of the horizontal kinetic energy. They are derived from the momentum equation in physical space and on each level l (Becker 2003):

$$\begin{aligned} \partial_t \xi_l &= (\nabla \times \mathbf{F}_l) \cdot \mathbf{e}_z \,, \\ \partial_t \delta_l &= \nabla \cdot \mathbf{F}_l - \nabla^2 B_l \end{aligned} \tag{4}$$

with

$$\begin{aligned} \mathbf{F}_l &= \mathbf{v}_l \times (f + \xi_l)\, \mathbf{e}_z - (\dot{\eta}\partial_\eta \mathbf{v})_l - \left(\frac{RT}{p}\nabla p\right)_l + \mathbf{R}_l\,, \\ B_l &= \frac{\mathbf{v}_l^2}{2} + \Phi_l\,. \end{aligned} \tag{5}$$

Here $\mathbf{F}$ is composed from all contributions which cannot be written as a potential. The symbols in (5) refer on each level l to horizontal velocity $\mathbf{v}$, Coriolis parameter f, vertical advection on hybrid (η) levels $\dot{\eta}\partial_\eta \mathbf{v}$, gas constant R, temperature T, pressure p, and momentum diffusion $\mathbf{R}$. The horizontal Nabla operator is denoted as ∇. The geopotential Φ and the horizontal kinetic energy $\mathbf{v}_l^2/2$ compose the potential B. The transformation of (4) into spectral space for total wavenumber n and zonal wavenumber m yields:

$$\begin{aligned} \dot{\xi}_{lnm} &= \int d\sigma \left[\mathbf{F}_l \times \nabla Y_{nm}\right] \cdot \mathbf{e}_z\,, \\ \dot{\delta}_{lnm} &= -\int d\sigma \left[\mathbf{F}_l \cdot \nabla Y_{nm} + B_l\, \nabla^2 Y_{nm}\right]\,. \end{aligned} \tag{6}$$

2.3 Subgrid-scale turbulence

Horizontal and vertical turbulent diffusion of momentum and sensible heat are the only subgrid-scale parameterizations of the KMCM. Fur the purpose of this study special emphasis is put on the horizontal diffusion scheme employed in the KMCM. It was developed by Becker and Burkhardt (2007) and is based on the ideas of Smagorinsky (1963). One main goal of the KMCM is to explicitly simulate upper mesospheric GW effects. As such the model has to allow for sufficiently strong GW activity and a self-consistent interaction of the resolved GW and the mean flow up to the mesopause, while maintaining conservation laws for energy and angular momentum (Becker and Fritts 2006). In this respect the nonlinear diffusion scheme of Becker and Burkhardt (2007) serves well. However, the modeled spectrum is unrealistically flattened for higher wavenumbers ("spectral blocking"), which represents a major obstacle when interpreting the upper tropospheric energy cascade on the basis of the KE spectrum. For this reason and on top of the Smagorinsky-based diffusion, a new hyperdiffusion scheme was developed (Brune and Becker 2012) which is consistent with the conservation laws while mitigating the spectral blocking for the mesoscales. As a result,

the simulated KE spectrum compares well to the aforementioned observational and computational estimates. In the following the horizontal diffusion scheme is shortly presented, more details can be found in Appendix A.

In the nonlinear "conventional" scheme of Becker and Burkhardt (2007) the tendency of the horizontal wind due to the horizontal momentum diffusion $\mathbf{H}$ can be written on each hybrid level as:

$$\mathbf{H}_l = \Delta p_l^{-1} \nabla \left(\Delta p_l K_{hl} \mathbf{S}_{hl} \right) \tag{7}$$

with the pressure increment between two half levels Δp_l, the horizontal turbulent diffusion coefficient K_{hl} and the strain tensor $\mathbf{S}_{hl}$. It should be noted that the total momentum diffusion $\mathbf{R}_l$ in (5) consists of $\mathbf{H}_l$ and a standard vertical diffusion $\mathbf{Z}_l$.

The additional hyperdiffusion extends (7) into:

$$\mathbf{H}_l = \Delta p_l^{-1} \nabla \left(\Delta p_l K_{hl} \mathbf{S}_{hl} \right) + \Delta p_l^{-1} \nabla \left(\Delta p_l K_{h0l} \mathbf{S}_{hfl} \right) \, . \tag{8}$$

Here, the additional horizontal turbulent diffusion coefficient K_{h0l} is constant for each level and the additional strain tensor $\mathbf{S}_{hfl}$ is a function of a filtered velocity which is different from zero only for the smallest scales, i.e. $n > 270$ in the T330 model setup, see Appendix A. That means, the hyperdiffusion is applied to the smallest scales only, ensuring for a separation from the horizontal scale where the transition in the spectrum from a -3 law to a -5/3 law ($n \approx 150$) occurs. As described by Hamilton et al. (2008), this scale separation may be needed to allow for the desirable independence of the transition wavenumber from the hyperdiffusion. In contrast to the conventional term (first term on the right-hand side of (8)), which never becomes negative (Becker 2001), the additional diffusion term (second term on rhs. of (8)) is of arbitrary sign.

As shown in Appendix A the formulation for both the standard and the filtered stress tensor fulfills the angular momentum conservation law. Moreover, it also fulfills the hydrodynamic energy conservation law, since the additional terms K_{h0l} and $\mathbf{S}_{hfl}$ are included in the horizontal frictional heating, or dissipation, which is part of the thermodynamic equation of motion and can be written as:

$$\epsilon_{hl} = K_{hl}(\mathbf{S}_{hl}\nabla) \cdot \mathbf{v} + K_{h0l}(\mathbf{S}_{hfl}\nabla) \cdot \mathbf{v} = K_{hl}|\mathbf{S}_{hl}|^2 + ((K_{h0l}\mathbf{S}_{hfl})\nabla) \cdot \mathbf{v} \, . \tag{9}$$

The frictional heating due to the hyperdiffusion, represented by the second term on the right-hand side of (9), is not positive definite any more. Nevertheless, it is always dominated by the positively definite contribution of the standard Smagorinsky scheme, the first term on the right-hand side of (9), thus the frictional heating ϵ_{hl} stays always positive.

2.4 Evidence of gravity waves

This chapter is closed with some remarks on the GW generation in our model. Gravity waves can be directly associated with the divergent component of the atmospheric flow, despite the fact, that baroclinic waves, cyclones, and fronts do contribute to the divergent modes as well, albeit on larger scales. Therefore it may be convenient to use the divergent mode for an illustration of mesoscale GWs. This is confirmed in Fig. 6, which shows a snapshot of the divergence δ from the T210L190 run. Mesoscale waves are evident in this run at all heights. The same applies to the T330 runs (not shown here). The most important generation mechanism for GWs in the KMCM are geostrophic adjustment and fronts as a result of the evolution of baroclinic instabilities in the mid latitudes (O'Sullivan and Dunkerton 1995). The other major generation mechanisms in the real troposphere and lower stratosphere (Fritts and Alexander 2003) are less important due to the model constraints: The use of a T106 orography in all our model runs inhibits orographically generated GWs at wavenumbers larger than $n = 106$; convective generation, especially due to tropical deep convection, is absent since latent heating is only paramaterized by simple means.

The GWs which pass the tropopause may propagate upward through the stratosphere and mesosphere. The background conditions determine the propagation characteristics, especially the aspect ratio of the waves and the existence of critical layers. Thus the generated GWs may be refracted, damped or absorbed. This can be seen in Fig. 6a, where in the stratosphere (15 to 55 km) particular wave trains alter their inclination depending on the aspect ratio of horizontal and vertical wavenumber. The lower mesosphere (55 to 80 km) represents a major obstacle for the vertical propagation of most of the GWs in this snapshot. This behavior is typical for the mid latitudes in winter. Only at 10°W some waves slip through to the upper mesosphere (80 to 95 km) and even the lower thermosphere (above 95 km).

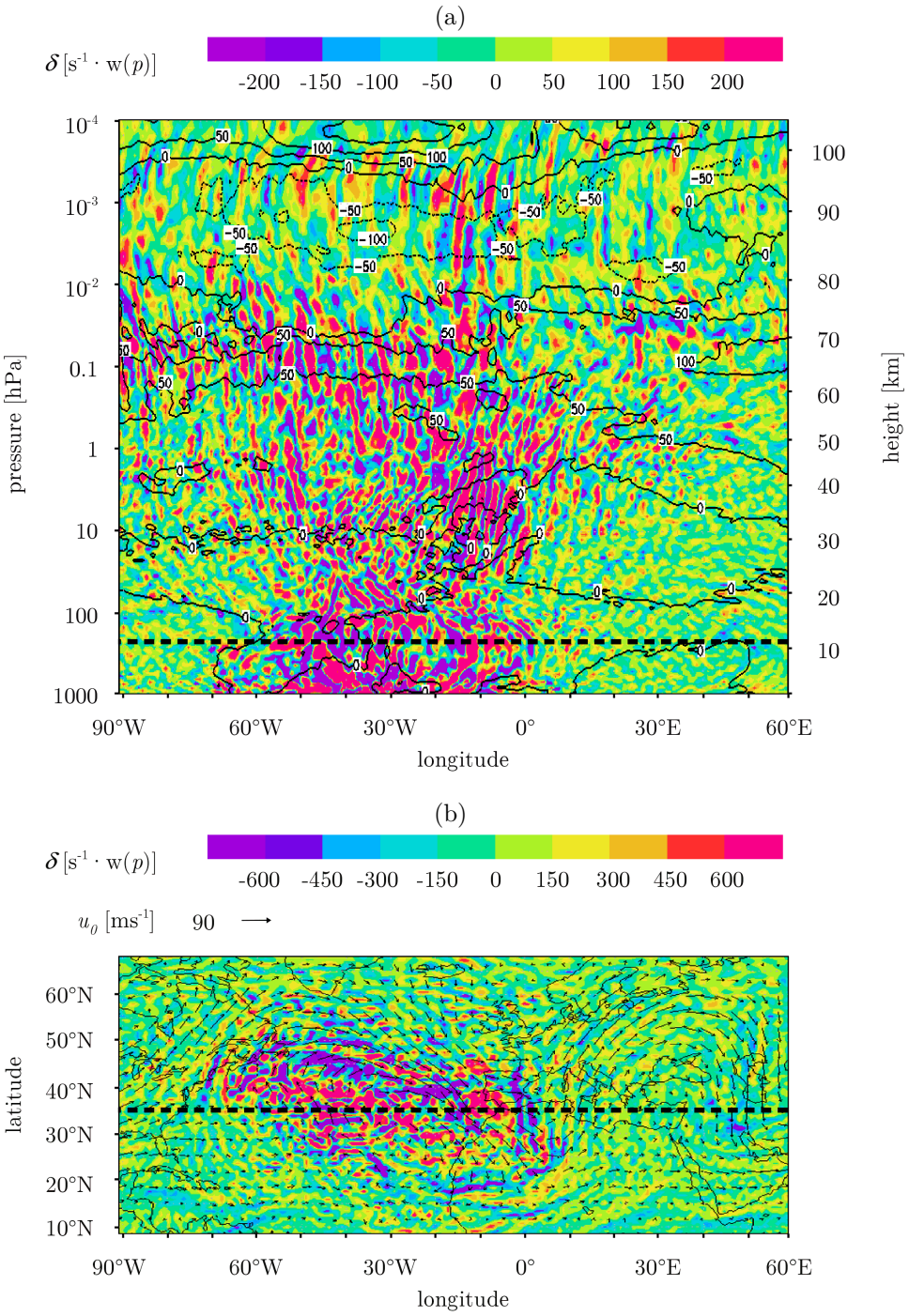

Fig. 6: (a) Cross section of divergence δ over the Northern Atlantic at 35°N from KMCM T210L190, one snapshot. Mesoscale waves are visible up to the mesosphere, their aspect ratio depends on the zonal background wind (in contours) above a strong tropospheric vortex as shown in the divergence and horizontal wind (arrows) map at 230 hPa (11 km) over the Northern Atlantic in (b). All values have been pressure weighted by $\mathrm{w}(p[\mathrm{hPa}]) = p^{0.2}$. The plane crossings are indicated by the dotted line.

In this study, however, we will interpret rather climatological time scales and no particular GW nor geographic region is considered in detail. The results are always based on an average in time, depending on how long the model has been run and how many snapshots have been taken, and in space, i.e. over the whole globe (see Section 3.6).

It should also be noted that the model does not contain atmospheric tides, which on the corresponding time scales may strongly influence the propagation of particular GWs in the middle atmosphere (Preusse et al. 2001; Senf and Achatz 2011).

3 Analysis

In this chapter the spectral diagnostics which we applied to the model data is introduced. It is based on the horizontal spectral kinetic energy and its tendency (budget). Mathematically, the momentum equation (4) as a part of the dynamical core of the model is exploited, see Section 2.2. Several contributions to this equation will be classified. Their impact on the kinetic energy and its budget in the troposphere, stratosphere, and mesosphere form the basis of the interpretation. Furthermore spectral fluxes of energy and enstrophy will be calculated as they are crucial for the understanding of spectral cascades, especially in the upper troposphere. Although the main interpretation follows in Chapter 4, some results are already exemplarily shown here for the T330L100 run at 220 hPa (Fig. 7).

3.1 Spectrum of kinetic energy

In the KMCM, the grid-space representation of the horizontal $\mathbf{v}$ wind can be written as

$$\mathbf{v} = \sum_{n=1}^{N} \frac{{a_e}^2}{n(n+1)} \sum_{m=-n}^{+n} \left(\xi_{nm}(\mathbf{e}_z \times \nabla Y_{nm}) + \delta_{nm} \nabla Y_{nm}\right) . \tag{10}$$

Here, ξ_{mn} and δ_{mn} are the spectral amplitudes of horizontal vorticity, ξ, and horizontal divergence, δ, while n is the total and m the zonal wavenumber. The spherical harmonics Y_{nm} are real and normalized. Furthermore, ∇ represents the horizontal gradient operator in spherical geometry and $\mathbf{e}_z$ the unit vector in vertical direction, a_e denotes the Earth's radius.

With (10), the spectral kinetic energy per unit mass at a particular model layer l is given in terms of the discrete power spectra of ξ and δ:

$$K_{lmn} = \frac{a_e^2}{8\pi n(n+1)} \left(\xi_{lmn}^2 + \delta_{lmn}^2\right) . \tag{11}$$

The horizontal kinetic energy contained in each total wavenumber n then yields:

$$K_{ln} = \sum_{m=-n}^{n} K_{lmn} = \frac{a_e^2}{8\pi n(n+1)} \sum_{m=-n}^{n} \left(\xi_{lmn}^2 + \delta_{lmn}^2\right) . \tag{12}$$

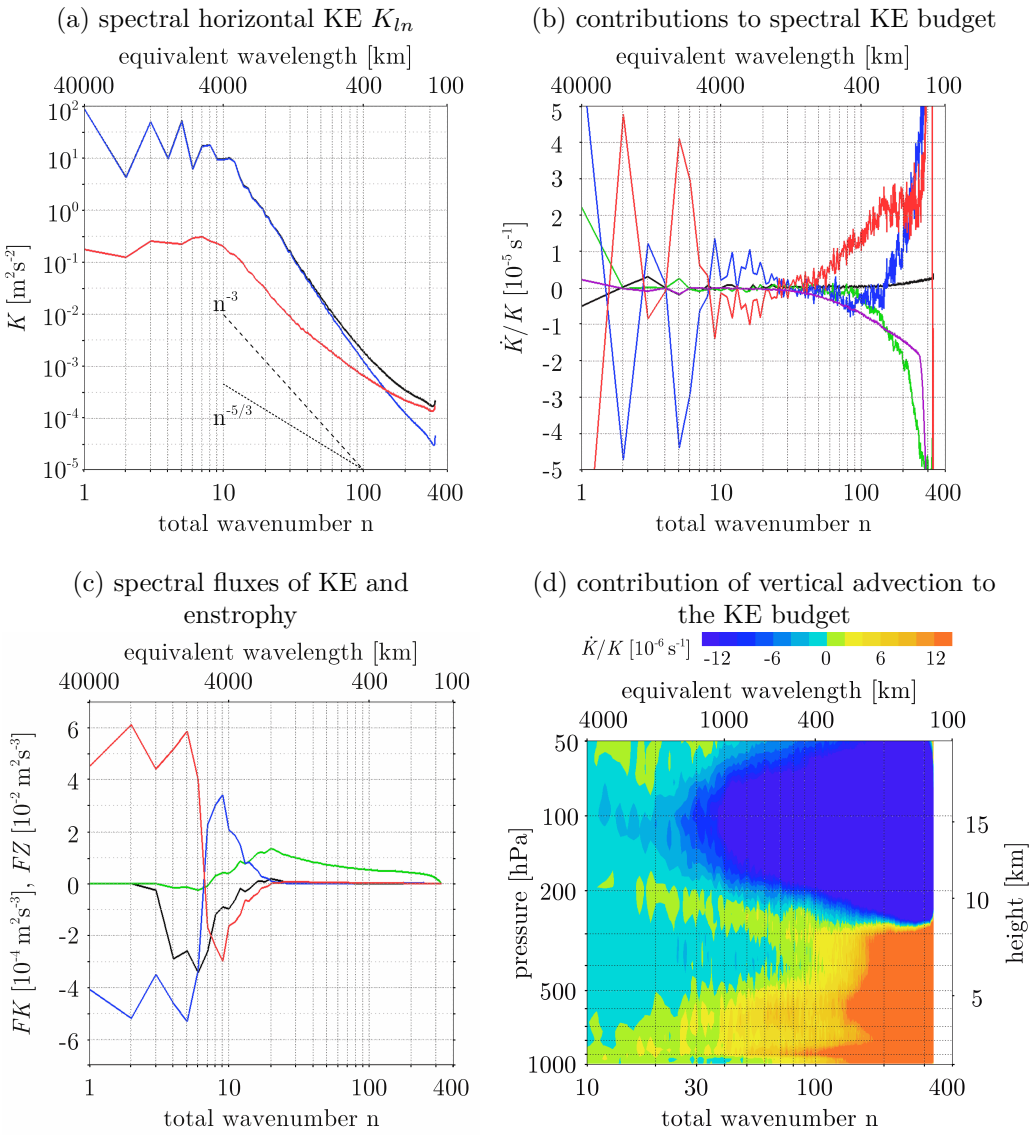

Fig. 7: Examples for the T330L100 run at 229 hPa (11 km), averaged over 17 model days, (a) Kinetic energy spectra, black: horizontal kinetic energy K_{ln}, blue: squared vorticity, red: squared divergence, the lines in the lower part have slopes of -3 and -5/3, (b) Contributions (normalized by K_{ln} as in (24)) to the tendency $\dot{K}_{ln}$ (black), red: horizontal advection, green: vertical advection, blue: adiabatic conversion, purple: total diffusion, (c) Spectral fluxes, black: 2D kinetic energy flux, green: 2D enstrophy flux, blue: total kinetic energy flux due to adiabatic conversion, red: total kinetic energy flux due to horizontal advection (note the different scaling for enstrophy (FZ) and kinetic energy fluxes (FK)), (d) Vertical cross section up to 50 hPa (20 km) of the normalized contribution of vertical advection to $\dot{K}_{ln}$.

We also calculate the separate contributions from the rotational and divergent flow to K_{ln}:

$$K_{ln}^{\xi} = \frac{a_e^2}{8\pi n(n+1)} \sum_{m=-n}^{n} \xi_{lmn}^2 \,, \tag{13}$$

$$K_{ln}^{\delta} = \frac{a_e^2}{8\pi n(n+1)} \sum_{m=-n}^{n} \delta_{lmn}^2 \,. \tag{14}$$

In Fig. 7a, K_{ln} as well as K_{ln}^{ξ} and K_{ln}^{δ} are shown as calculated from the T330L100 run for an upper tropospheric model level around 220 hPa ($\approx$ 11 km height). It is notable that both the rotational and divergent energies follow their distinctive slopes ($K_{ln}^{\xi} \propto n^{-3}$, $K_{ln}^{\delta} \propto n^{-5/3}$) at almost all scales smaller than the injection range ($n \approx 10$). Depending on the dominant mode the kinetic energy spectrum is assuming the respective slope. In particular, the transition to the mesoscale -5/3 spectrum is characterized by a transition wavenumber n_T, where the following identity is fulfilled:

$$K_{ln_T}^{\xi} = K_{ln_T}^{\delta} \,. \tag{15}$$

At 220 hPa in the upper troposphere (Fig. 7a) the transition occurs around $n_T \approx 160$. As will be shown later from the results of the T330L30 run, this behavior does not hold true for a coarser vertical resolution.

3.2 Spectral kinetic energy budget

The time tendencies of vorticity and divergence in spectral space are calculated using the model's dynamical core, where we again extend on the formulation of the momentum equation (4). Instead of calculating only the overall time tendencies, different contributions shall be classified, calculated and interpreted. We believe that in this way we can pin-point some of the processes that determine the spectral kinetic energy. Furthermore, we can take advantage of KMCM's abilities in the mesosphere and extend the spectral analysis up to the mesopause, especially regarding the mesoscales.

The tendency of horizontal kinetic energy is generally given by:

$$\frac{d}{dt}K = \dot{K} \propto \xi\dot{\xi} + \delta\dot{\delta}\,. \tag{16}$$

Again, with KMCM normalization we get for each spectral component (n, m) at level l:

$$\dot{K}_{lnm} = \frac{a_e^2}{4\pi n(n+1)}\left(\xi_{lnm}\dot{\xi}_{lnm} + \delta_{lnm}\dot{\delta}_{lnm}\right)\,, \tag{17}$$

and the tendency of kinetic energy of total wavenumber n:

$$\dot{K}_{ln} = \frac{a_e^2}{4\pi n(n+1)}\sum_{m=-n}^{n}\left(\xi_{lnm}\dot{\xi}_{lnm} + \delta_{lnm}\dot{\delta}_{lnm}\right)\,. \tag{18}$$

We additionally normalize the tendency to K_{ln}.

$$\frac{\dot{K}_{ln}}{K_{ln}} = \frac{1}{K_{ln}}\frac{a_e^2}{4\pi n(n+1)}\sum_{m=-n}^{n}\left(\xi_{lnm}\dot{\xi}_{lnm} + \delta_{lnm}\dot{\delta}_{lnm}\right)\,. \tag{19}$$

Let us recall the momentum equation (6) in spectral space for vorticity and divergence in the KMCM:

$$\begin{aligned}
\dot{\xi}_{lnm} &= \int d\sigma \left[\mathbf{F}_l \times \nabla Y_{nm}\right] \cdot \mathbf{e}_z\,, \\
\dot{\delta}_{lnm} &= -\int d\sigma \left[\mathbf{F}_l \cdot \nabla Y_{nm} + B_l\,\nabla^2 Y_{nm}\right]
\end{aligned} \tag{20}$$

with

$$\begin{aligned}
\mathbf{F}_l &= \mathbf{v}_l \times (f + \xi_l)\,\mathbf{e}_z - (\dot{\eta}\partial_\eta \mathbf{v})_l - \left(\frac{RT}{p}\nabla p\right)_l + \mathbf{R}_l\,, \\
B_l &= \frac{\mathbf{v}_l^2}{2} + \Phi_l\,.
\end{aligned} \tag{21}$$

The spectral tendencies of vorticity and divergence in (20) shall now be split into contributions from different processes according to (21):

$$
\begin{aligned}
\dot{\xi}_{lnm} = & \int d\sigma \left[\mathbf{v}_l \times (f + \xi_l)\, \mathbf{e}_z \times \nabla Y_{nm} \right] \cdot \mathbf{e}_z && \text{horizontal advection,} \\
& - \int d\sigma \left[(\dot{\eta} \partial_\eta \mathbf{v})_l \times \nabla Y_{nm} \right] \cdot \mathbf{e}_z && \text{vertical advection,} \\
& - \int d\sigma \left[\left(\frac{RT}{p} \nabla p \right)_l \times \nabla Y_{nm} \right] \cdot \mathbf{e}_z && \text{pressure gradient,} \\
& + \int d\sigma \left[\mathbf{H}_l \times \nabla Y_{nm} \right] \cdot \mathbf{e}_z && \left. \begin{array}{l} \text{horizontal diffusion} \\ + \text{ vertical diffusion} \\ = \text{ total diffusion;} \end{array} \right. \\
& + \int d\sigma \left[\mathbf{Z}_l \times \nabla Y_{nm} \right] \cdot \mathbf{e}_z &&
\end{aligned}
\tag{22}
$$

$$
\begin{aligned}
\dot{\delta}_{nm} = & - \int d\sigma \left[\mathbf{v}_l \times (f + \xi_l)\, \mathbf{e}_z \cdot \nabla Y_{nm} \right] && \left. \begin{array}{l} \\ \\ \end{array} \right\} \text{ horizontal advection,} \\
& - \int d\sigma \left[\frac{{\mathbf{v}_l}^2}{2} \cdot \nabla^2 Y_{nm} \right] && \\
& + \int d\sigma \left[(\dot{\eta} \partial_\eta \mathbf{v})_l \cdot \nabla Y_{nm} \right] && \text{vertical advection,} \\
& + \int d\sigma \left[\left(\frac{RT}{p} \nabla p \right)_l \cdot \nabla Y_{nm} \right] && \left. \begin{array}{l} \text{pressure gradient} \\ + \text{ geopotential} \\ = \text{ adiabatic conversion,} \end{array} \right. \\
& - \int d\sigma \left[\Phi_l \cdot \nabla^2 Y_{nm} \right] && \\
& - \int d\sigma \left[\mathbf{H}_l \cdot \nabla Y_{nm} \right] && \left. \begin{array}{l} \text{horizontal diffusion} \\ + \text{ vertical diffusion} \\ = \text{ total diffusion.} \end{array} \right. \\
& - \int d\sigma \left[\mathbf{Z}_l \cdot \nabla Y_{nm} \right] &&
\end{aligned}
\tag{23}
$$

Combining (19) with (22) and (23), each of the contributing terms can be described as:

$$
\frac{\dot{K}_{ln}^{[\ldots]}}{K_{ln}} = \frac{1}{K_{ln}} \frac{a_e^2}{4\pi n(n+1)} \sum_{m=-n}^{n} \left(\xi_{lnm} \dot{\xi}_{lnm}^{[\ldots]} + \delta_{lnm} \dot{\delta}_{lnm}^{[\ldots]} \right) , \tag{24}
$$

where $[\ldots]$ describes any particular process in (22) or (23). We calculate the contributions $\dot{\xi}_{nm}^{[\ldots]}$ and $\dot{\delta}_{nm}^{[\ldots]}$ separately and add the corresponding terms according

to (24). For example, the overall contribution of horizontal advection to the spectral kinetic energy budget is given by

$$\begin{aligned}\frac{\dot{K}_{ln}^{hadv}}{K_{ln}} &= \frac{1}{K_{ln}} \frac{a_e^2}{4\pi n(n+1)} \sum_{m=-n}^{n} \left(\xi_{lnm} \dot{\xi}_{lnm}^{hadv} + \delta_{lnm} \dot{\delta}_{lnm}^{hadv} \right) \\ &= \frac{1}{K_{ln}} \frac{a_e^2}{4\pi n(n+1)} \sum_{m=-n}^{n} \left(\xi_{lnm} \int d\sigma \left[\mathbf{v}_l \times (f + \xi_l)\, \mathbf{e}_z \times \nabla Y_{nm} \right] \cdot \mathbf{e}_z \right. \\ &\qquad \left. - \delta_{lnm} \int d\sigma \left[\mathbf{v}_l \times (f + \xi_l)\, \mathbf{e}_z \cdot \nabla Y_{nm} - \frac{{\mathbf{v}_l}^2}{2} \cdot \nabla^2 Y_{nm} \right] \right) . \end{aligned} \tag{25}$$

Some results are shown for the T330L100 run at 220 hPa in Fig. 7b. The time averaged total tendency is reasonably close to zero for all wavenumbers. We use this constraint to determine a climatological time span for the model and to check consistency (see Section 3.6.3). However, our main interest is to distinguish the different contributions from horizontal advection, vertical advection, adiabatic conversion and total diffusion as shown in Fig. 7b, which in the normal case are different from zero.

We also define a quasi-2D tendency by considering the horizontal advection only, neglecting the divergent flow, and incorporating only rotational modes acting on the rotational flow. Accordingly, we consider only the rotational component $\mathbf{v}^{rot}$ of the horizontal velocity and define the quasi-2D horizontal advection contribution to the vorticity budget as

$$\dot{\xi}_{lnm}^{2D} = \int d\sigma \left[\mathbf{v}_l^{rot} \times (f + \xi_l)\, \mathbf{e}_z \times \nabla Y_{nm} \right] \cdot \mathbf{e}_z \, . \tag{26}$$

Inserting (26) into (17) and (18), the quasi-2D kinetic energy tendency for each total wavenumber n reads

$$\dot{K}_{ln}^{2D} = \frac{a_e^2}{4\pi n(n+1)} \sum_{m=-n}^{n} \left(\xi_{lnm} \dot{\xi}_{lnm}^{2D} \right) , \tag{27}$$

or normalized by the kinetic energy as in (19)

$$\frac{\dot{K}_{ln}^{2D}}{K_{ln}} = \frac{1}{K_{ln}} \frac{a_e^2}{4\pi n(n+1)} \sum_{m=-n}^{n} \left(\xi_{lnm} \dot{\xi}_{lnm}^{2D} \right) . \tag{28}$$

3.3 Spectral enstrophy and quasi-2D enstrophy budget

In the KMCM the spectral enstrophy multiplied by a_e^2, $Z \propto \xi^2$, can be calculated for each wavenumber (m, n) and level l as

$$Z_{lmn} = \frac{a_e^2}{8\pi} \xi_{lmn}^2 \,. \tag{29}$$

The enstrophy tendency follows with:

$$\dot{Z}_{lmn} = \frac{a_e^2}{4\pi} \xi_{lmn} \dot{\xi}_{lmn} \,, \tag{30}$$

and the enstrophy budget for each total wavenumber n is calculated in analogy to the kinetic energy budget in (18):

$$\dot{Z}_{ln} = \frac{a_e^2}{4\pi} \sum_{m=-n}^{n} \left(\xi_{lnm} \dot{\xi}_{lnm} \right) \,. \tag{31}$$

The quasi-2D enstrophy tendency due to the rotational modes of the horizontal velocity can be calculated with (26) as

$$\dot{Z}_{ln}^{2D} = \frac{a_e^2}{4\pi} \sum_{m=-n}^{n} \left(\xi_{lnm} \dot{\xi}_{lnm}^{2D} \right) \,. \tag{32}$$

3.4 Energy and enstrophy fluxes through the spectrum

We define the energy flux FK_{ln} and the enstrophy flux FZ_{ln} through the spectrum by summing up the spectral kinetic energy budget (18) and enstrophy budget (31), respectively, starting from the spectral truncation wavenumber N:

$$\begin{aligned} FK_{ln} &= \sum_{i=n}^{N} \dot{K}_{li} \,, \\ FZ_{ln} &= \sum_{i=n}^{N} \dot{Z}_{li} \,. \end{aligned} \tag{33}$$

Kinetic energy fluxes can be derived for the different contributions to the kinetic energy budget (22), (23) as

$$\begin{aligned} FK_{ln}^{hadv} &= \sum_{i=n}^{N} \dot{K}_{li}^{hadv} \\ FK_{ln}^{vadv} &= \sum_{i=n}^{N} \dot{K}_{li}^{vadv} \\ FK_{ln}^{pot} &= \sum_{i=n}^{N} \dot{K}_{li}^{pot} \\ FK_{ln}^{tdif} &= \sum_{i=n}^{N} \dot{K}_{li}^{tdif} \\ FK_{ln}^{2D} &= \sum_{i=n}^{N} \dot{K}_{li}^{2D} \,, \end{aligned} \tag{34}$$

and the 2D enstrophy flux is derived from the 2D enstrophy budget (32) as

$$FZ_{ln}^{2D} = \sum_{i=n}^{N} \dot{Z}_{li}^{2D} \,. \tag{35}$$

We will primarily use the kinetic energy fluxes due to horizontal advection, both total and quasi-2D, and adiabatic conversion, as well as the quasi-2D enstrophy flux in our interpretation of the tropospheric macroturbulence. In Fig. 7c these fluxes are shown for the T330L100 run at model level 229 hPa.

3.5 Estimation of Froude number

In the context of stratified turbulence the question arises, how adequate the spatial discretization of our model is to describe such kind of a mesoscale flow, which is controlled by both horizontal inertial forces and buoyancy forces. Their ratio can be expressed in terms of a characteristic velocity U, the Brunt-Väisälä frequency N, and either a characteristic horizontal length scale L_h or characteristic vertical length scale L_v. This gives rise to the horizontal and vertical Froude number, i.e.,

$$Fr_h \approx \frac{U}{NL_h} \,, Fr_v \approx \frac{U}{NL_v} \,. \tag{36}$$

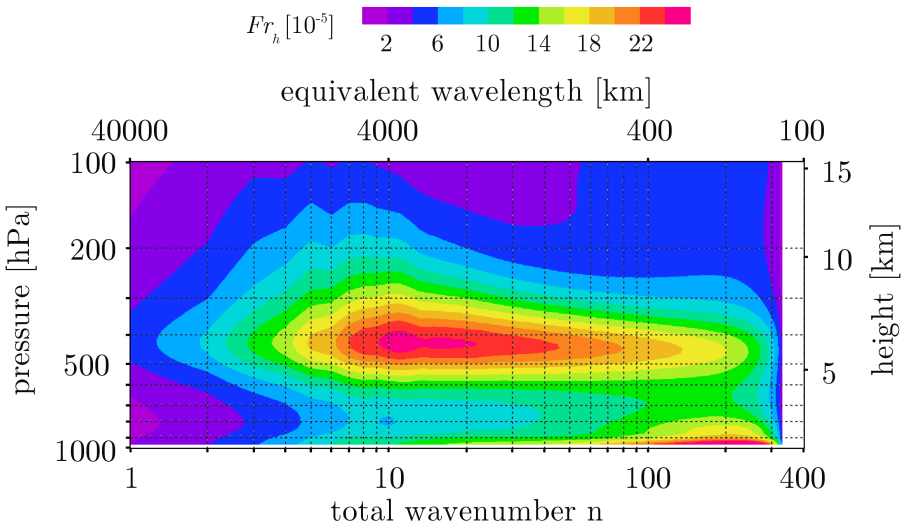

Fig. 8: Horizontal Froude numbers Fr_h for troposphere and lower stratosphere from KMCM T330L100, averaged over 17 model days.

The Brunt-Väisälä frequency N is a zonally and meridionally averaged value from the T330L100 run. It varies in the troposphere between 0.01 and 0.015 s^{-1} and increases to 0.025 s^{-1} across the tropopause into the stratosphere. For a given horizontal wavenumber n the horizontal length scale is $L_h = 2\pi a_e/n$ and we derive $U = \sqrt{\sum_{i=n}^{N} K_i}$ from the energy spectrum. The horizontal Froude number based on these estimates is shown in Fig. 8 for our T330L100 run. It can be seen that for $n > 10$ in the middle and upper troposphere Fr_h is approximately between 0.00005 and 0.00025 with decreasing dependency on n for $n > 50$.

The horizontal Froude number meets the general inequality for the existence of stratified turbulence (Riley and Lindborg 2008): $Fr_h << 1$ and is also considerably smaller than $Fr_{h_{crit}} \approx 0.02$ as established by Lindborg (2006) for the transition from stratified turbulence ($Fr_h < Fr_{h_{crit}}$) to 3D turbulence ($Fr_h > Fr_{h_{crit}}$).

The calculation of the vertical Froude number Fr_v in (36) is not that simple. A rather crude approximation for L_v is twice the vertical distance between two levels in our vertical discretization, which gives $L_v \approx 400$ m and $0.01 < Fr_v < 0.6$ for corresponding wavenumbers $300 > n > 10$. This is indeed smaller than it was considered by Billant and Chomaz (2001) ($Fr_v \approx 1$) or calculated by Lindborg (2006) ($Fr_v \approx 0.6$ for his box model), but nevertheless we believe that Fr_v lies still within an acceptable range for stratified turbulence. Of course a finer vertical resolution would be extremely helpful in future simulations.

3.6 Averaging

Our analysis includes several averaging procedures. When calculating quantities in dependence of the total wavenumber alone, such as in (12), a global average is applied. We also carry out vertical averaging to enhance signal-to-noise ratios and time averaging to obtain climatological values. The energy and enstrophy flux calculation in Section 3.4 represents another average while summing over the total wavenumber n. In the following some aspects of the different averaging procedures will be discussed.

3.6.1 Spectral expansion, global average

Let us compare the horizontal kinetic energy in physical space $E = (u^2 + v^2)/2$, its longitudinal Fourier spectrum, and the total wavenumber spectrum for an upper tropospheric level, for the latter see also Appendix B or Washington and Parkinson (2005).

As shown in Fig. 9a, E is unevenly distributed over the globe. Even when time evolves (not shown), zones of high kinetic energy in the mid latitudes can be contrasted to the subpolar and equatorial regions with relatively low kinetic energy content.

These zones are also visible in Fig. 9b, where for every latitude the longitudinal Fourier spectrum of E is shown. The mid latitudes are characterized by strong planetary waves ($m = 2, 3$, northern hemisphere) and also strong baroclinic waves ($m = 5$, northern and southern hemisphere). Compared to the mid latitudes the equatorial region contains relatively low kinetic energy at all wavenumbers. When compared to the real troposphere, the small synoptic and mesoscales ($m > 40$) in the tropics are likely to be underestimated, which is caused by the absence of tropical deep convection in KMCM and a constant tropical latent heating instead.

Figure 10 displays the full spectral expansion corresponding to Fig. 9 at 229 hPa. Here, K_{nm} is shown separately for zonal wavenumbers m with $-n \leq m \leq -1$ (above) and for m with $1 \leq m \leq n$ (below), the zonal average $m = 0$ is not displayed. For reference the global pattern of the spherical harmonic function for $(n, m) = (7, 3)$ is shown in the upper left panel. Apart from the tropics it corresponds to the distribution of strong and weak winds in Fig. 9a and its coefficient for K_{nm} strongly contributes to the overall maximum of K_{nm} in Fig. 10 at $n = 7$ and $1 \leq m \leq 4$.

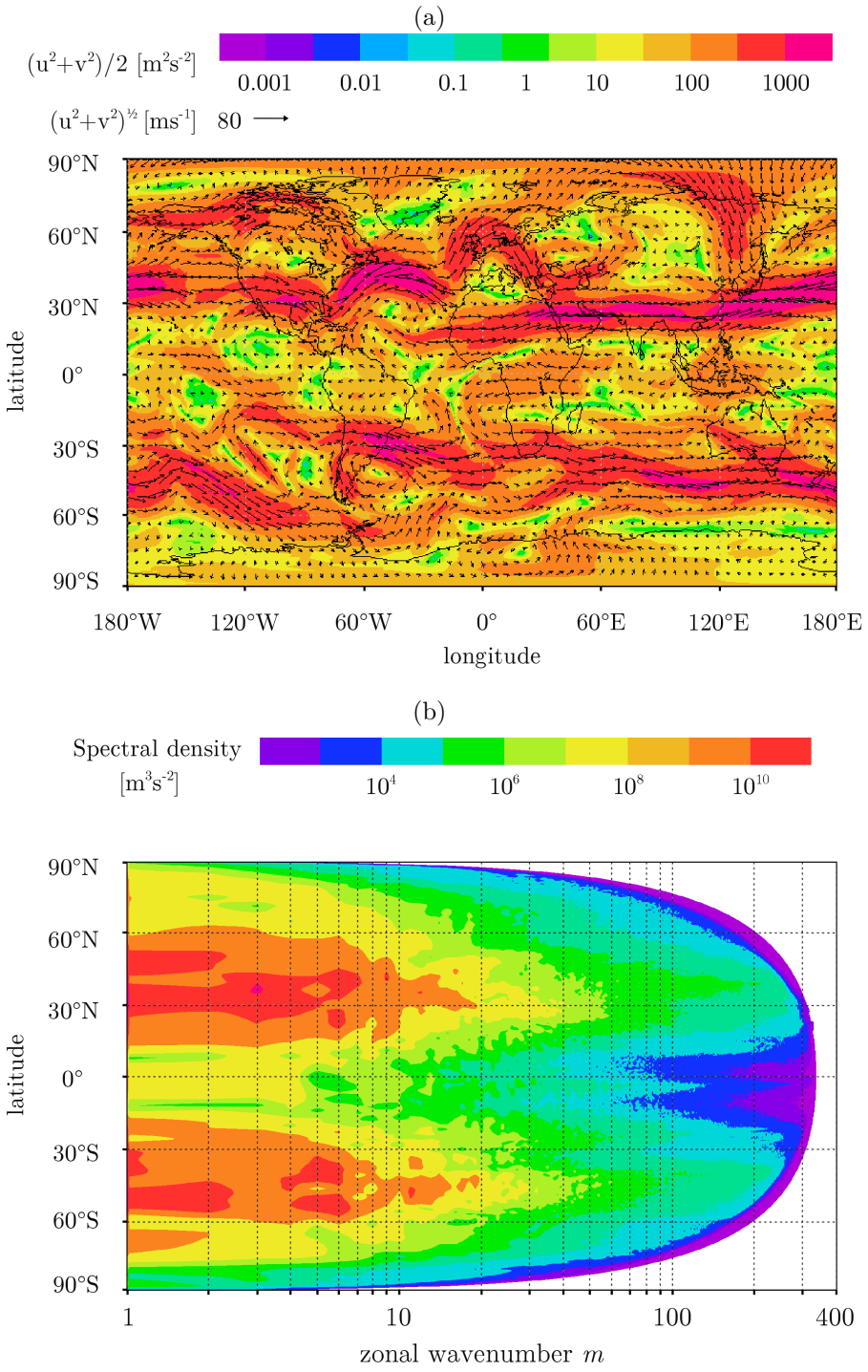

Fig. 9: (a) Arbitrary snapshot of the horizontal kinetic energy $E = (u^2 + v^2)/2$ from the T330L100 simulation at 229 hPa (11 km) as a function of latitude and longitude together with the wind vectors, (b) Corresponding instantaneous wind Fourier power spectrum. The zonal wavenumber corresponds to different zonal wavelengths depending on latitude, i.e. $m = 5$ corresponds to a wavelength of 8000 km at the equator and 4000-5000 km at mid latitudes.

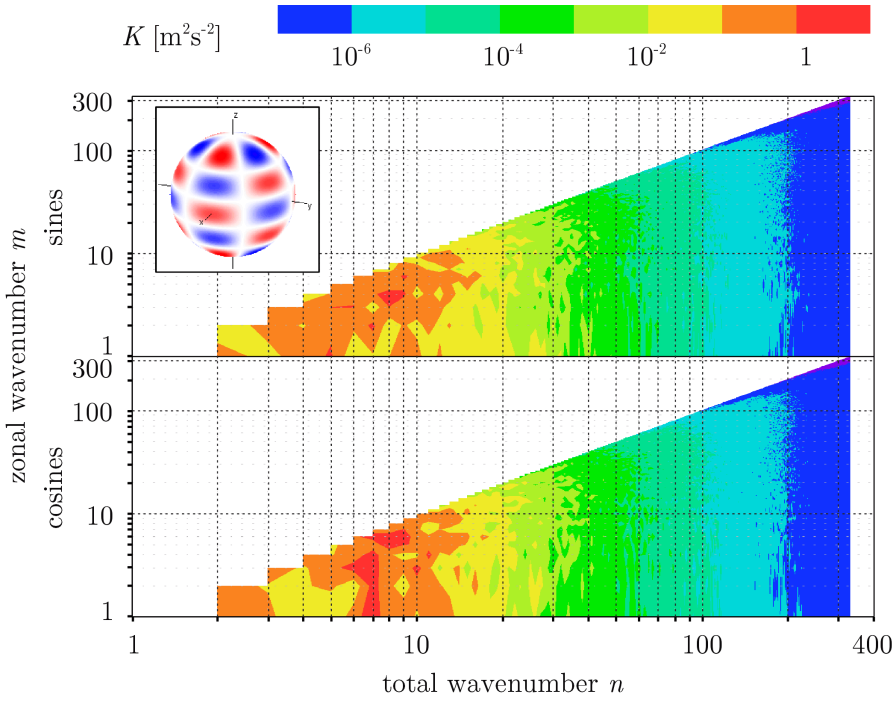

Fig. 10: Spectral horizontal kinetic energy K as a function of zonal wavenumber m (sines and cosines) and total wavenumber n for KMCM T330L100 at 229 hPa (11 km), the spherical harmonic Y_{nm} of degree $n = 7$ and order $m = 3$ is visualized in the upper left with positive values in red and negative values in blue (after *http://www.bpreid.com/poas.php*).

We will come back to the full expansion later to compare our model with the results of the SKYHI model (Koshyk and Hamilton 2001).

3.6.2 Vertical averaging

Our analysis is performed on a level by level basis. The model uses hybrid levels: terrain following in and near the boundary layer and nearly equivalent to pressure levels from the tropopause on (see Chapter 2.1).

A vertical average over a certain atmospheric altitude range (the upper troposphere, for instance, comprises around 20 of our model levels) would improve the quality of the spectra in terms of minimizing fluctuations. This may be important especially for short model runs where extensive time averaging (see Section 3.6.3) can not be applied. However, level to level changes are lost, which may represent an obstacle to further interpretations.

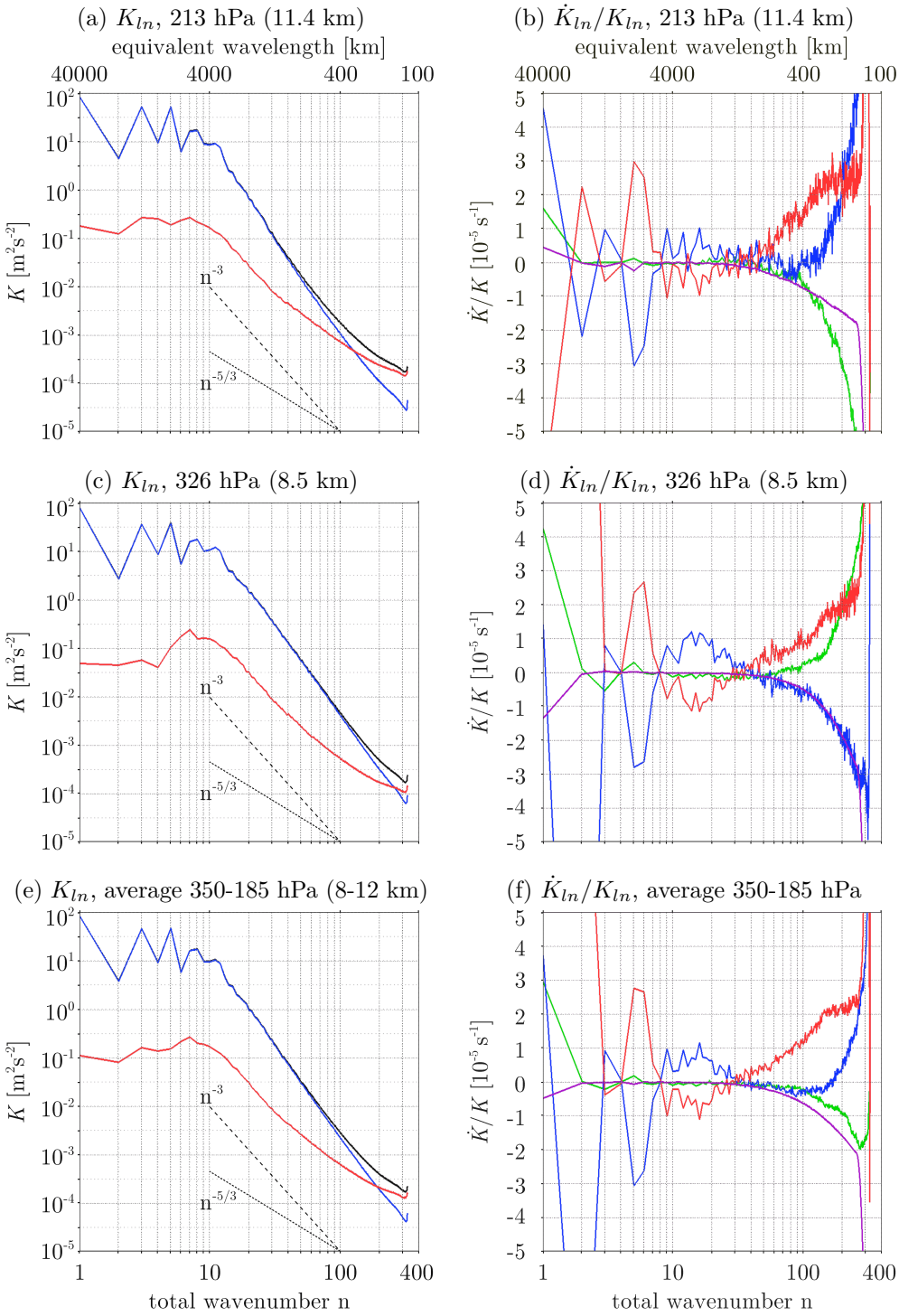

Fig. 11: Left: K_{ln} (black) with rotational (red) and divergent (blue) components, right: contributions of horizontal advection (red), vertical advection (green), adiabatic conversion (blue), momentum diffusion (purple) to $\dot{K}_{ln}/K_{ln}$ (black); individual model levels (above and middle) and upper tropospheric vertical average (19 model levels, below) from KMCM T330L100, averaged over 17 model days.

As an example we recall in Fig. 11 K_{ln} and $\dot{K}_{ln}$ for two selected model levels in the upper troposphere. The lowermost figures represent the vertical average over all upper tropospheric levels.

In the kinetic energy spectrum (left-hand side of Fig. 11) vertical averaging seems to be reasonable for the total KE (black curves), but the transition from dominant rotational modes to dominant divergent modes is strongly dependent on height: $n_T \approx 250$ for 326 hPa to $n_T \approx 120$ for 213 hPa, the averaged value $n_T \approx 220$ may be of less relevance.

The contributions to the spectral kinetic energy budget at the right-hand side of Fig. 11 partly show such a strong vertical dependency, too. Horizontal advection and total diffusion do not change dramatically over the upper troposphere and may thus be averaged. However, vertical advection and adiabatic conversion change even sign. We will see later that it is only because of these height variations that we may apply the concept of stratified turbulence to some parts of the upper troposphere. The average curves of these two contributions are of less importance.

Because of the strong vertical change of some of the contributions as shown in Fig. 11 we will not apply vertical averaging on a regular basis. We will also need a level by level assessment for the interpretation of macroturbulence within the troposphere. Last but not least we prefer the use of a vertical cross section as in Fig. 7d over a vertically averaged graph, since the former allows for a better visualization of the parameters in wavenumber-height space.

3.6.3 Time averaging

Time averaging is applied on a regular basis in our analysis. The goal is to derive "climatologically" representative values for the analyzed parameters. This means that essentially the derived averaged spectra only change minimally from one "climatological" period to the next. The necessary length of such a period may vary drastically depend on the analyzed parameter or the atmospheric layer. All runs have been initialized using climatologically equilibrated pre-runs, which are not subject to our analysis.

The analysis is applied to model snapshots with a time interval of 22.5 min for both the T210 and T330 runs. The instantaneously calculated diagnostic variables show very different behavior from snapshot to snapshot. This is exem-

plarily illustrated in Fig. 12 for two parameters: the horizontal spectral kinetic energy and its total tendency. The latter one is again normalized by the former to enhance the mesoscales, as introduced in (19). This normalization is applied after the time averaging: $\overline{\dot{K}}/\overline{K}$. However, we drop the overline and use $\dot{K}/K$ instead.

The spectral kinetic energy exhibits quasi-wave structures in time with periods depending on the total wavenumber n as shown in Fig. 12a, but a meaningful spectrum showing the main spectral slopes is already obtained from a few snapshots. As can be seen in Fig. 12b, the individual spectra are all within a narrow band around the average spectrum.

On the contrary, the contributions to the kinetic energy budget are highly variable from snapshot to snapshot, especially for larger wavenumbers (Fig. 12c). Therefore time averaging is essential to enhance the signal-to-noise ratio. For the total spectral budget (Fig. 12d) in the upper troposphere the averaging of 1024 model snapshots, equivalent to 16 model days, conserves horizontal kinetic energy for most wavenumbers and the total budget is approximately zero for $n > 4$. Thus it is a time period for the upper troposphere, where the maintenance of horizontal kinetic energy in a climatological sense is reasonably fulfilled.

This finding is not surprising since a typical baroclinic life cycle lasts for about 10 to 15 days and the transformation into spectral space corresponds to averaging over several baroclinic waves around the globe. Therefore the resulting spectra can be considered "climatologically" representative already after 16 model days.

Shorter time periods, and fewer snapshots, may still be appropriate to obtain a "climatological" mean for other parameters. For the T210L190 run it turned out that the spectral kinetic energy budget is equilibrated already after about 640 snapshots or 10 model days. When comparing three successive 10 day periods (not shown here), the averaged spectra of each of the contributions to the spectral kinetic energy budget yield the same results for each of the periods. Equilibration is reached at even shorter periods when other averaging procedures are applied, such as the calculation of the energy and enstrophy fluxes which represent sums over a certain wavenumber range.

We now extend this picture to the whole atmosphere up to the lower thermosphere. The vertical cross sections in Fig. 13 show the values for K_{ln} and $\dot{K}_{ln}/K_{ln}$ for different averaging periods from 22.5 min (one snapshot) to 16 d (1024 snap-

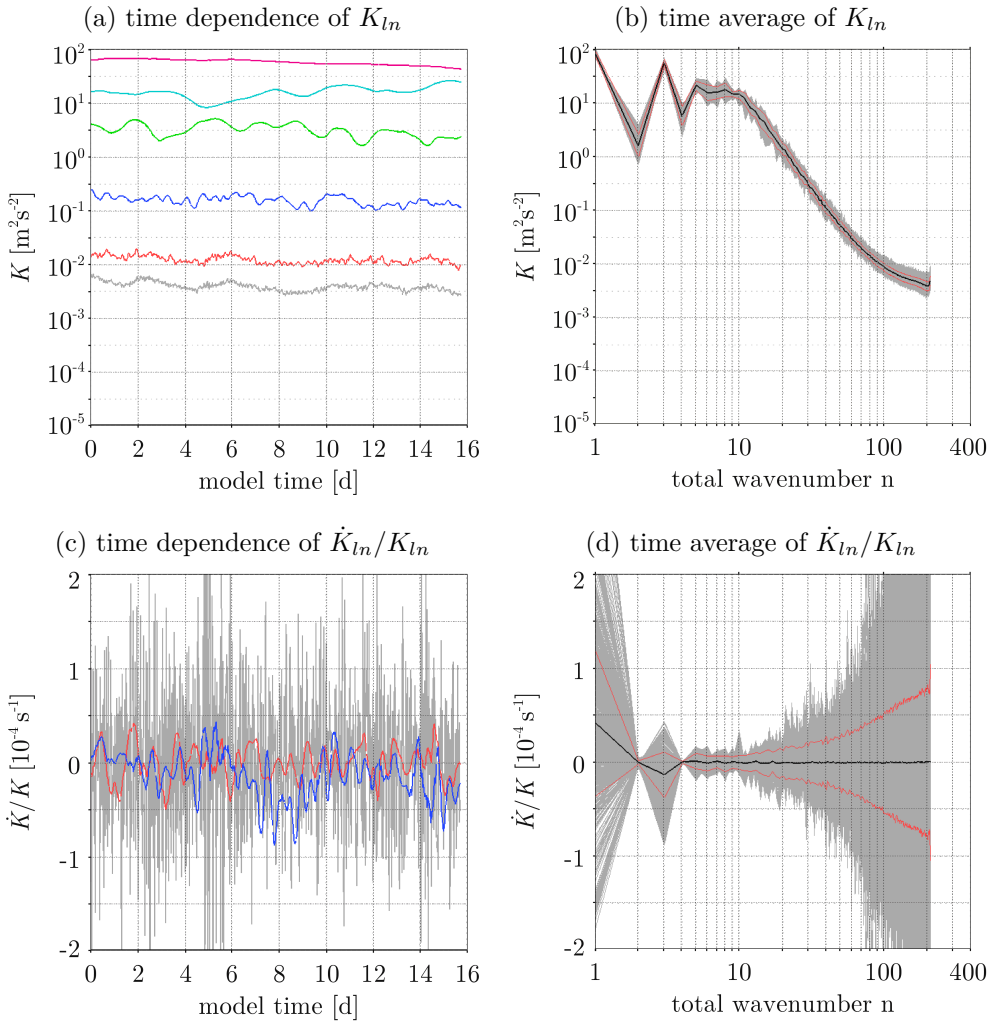

Fig. 12: Time series from KMCM T210L190 at 231 hPa (11 km) for 1024 snapshots comprising 16 model days: (a) Evolution in time of K_{ln} for selected wavenumbers $n = 3, 7, 16, 37, 86, 200$ from top to bottom, (b) Horizontal kinetic energy spectra for individual snapshot (gray), average spectrum in black with the standard deviation in red; (c), (d) same as in (a), (b) but for $\dot{K}_{ln}/K_{ln}$, selected wavenumbers in (c) are $n = 3$ (blue), 24 (red), 200 (gray).

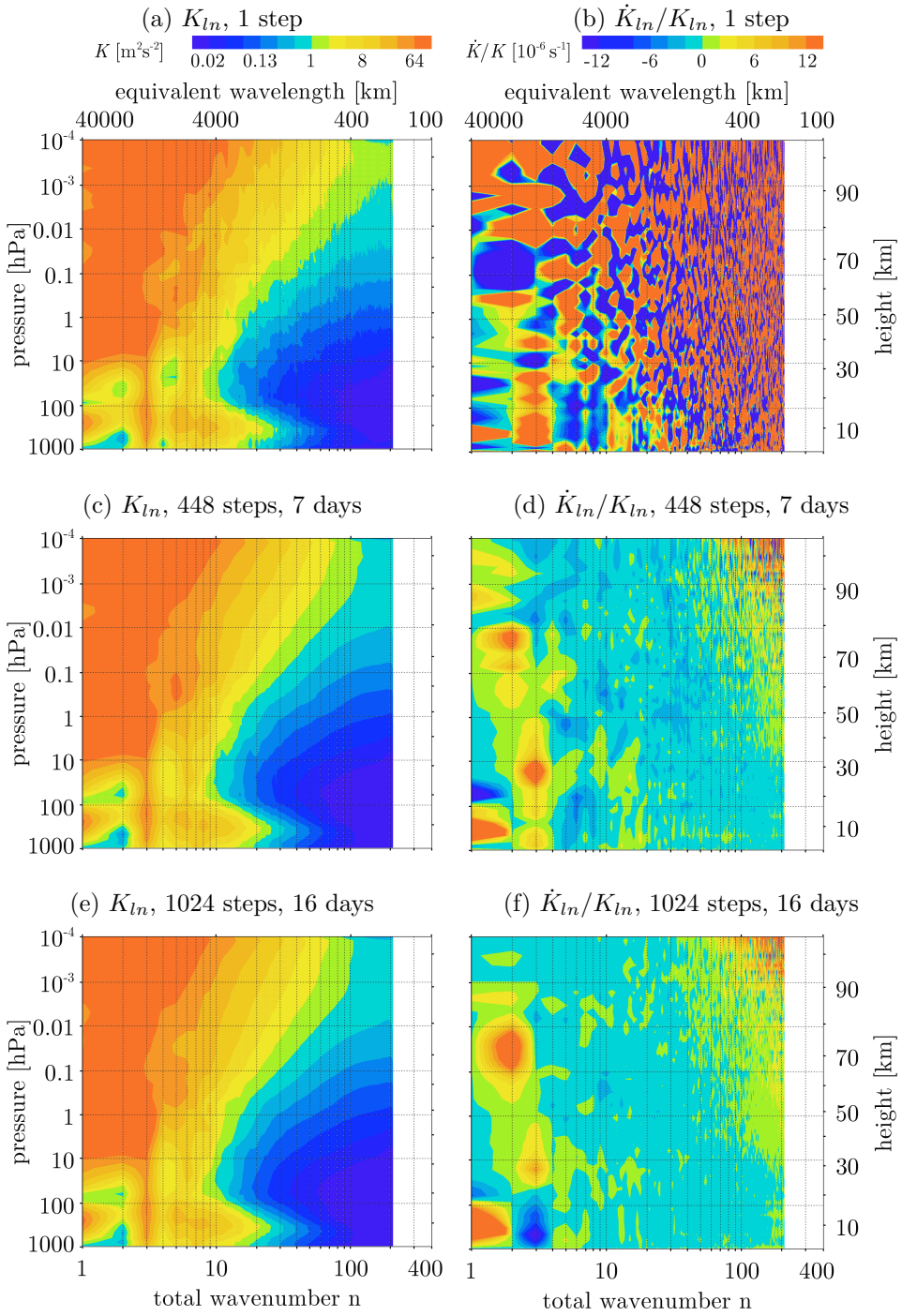

Fig. 13: Vertical cross sections from the boundary layer to the lower thermosphere of K_{ln} (left, all panels with the same colcor scale) and $\dot{K}_{ln}/K_{ln}$ (right, all panels with the same color scale). The number of snapshots (averaged model time) from top to bottom: 1 (22.5 min), 448 (7 d), and 1024 (16 d). The KMCM T210L190 run extends over 16 days, the first snapshot is always the same. The panels respectively use the color scales as in (a) and (b).

shots). The aforementioned different robustness in the spectral quantities can be seen throughout the whole global column: the time averaged spectral horizontal kinetic energy is nearly independent of the averaging period, whereas its total budget requires averaging over many model snapshots for being close to zero. It turns out that the upper mesosphere / lower thermosphere mesoscales as well as the planetary scales in troposphere and stratosphere may hardly reach the desired "climatological" mean of the budget even after 1024 snapshots (16 d). The adequate averaging period is obviously strongly dependent on wavenumber and height as well.

It should be noted that the snapshot interval could have been chosen considerably shorter, since the model's time step is in the range of tens of seconds. It could be therefore possible to get similar results from an even shorter period in model time, of course with the same amount of snapshots to be averaged. This has not been studied extensively so far. From Fig. 12a a total model time of 4 days could be sufficient enough to cover enough of the long-term fluctuations in K_{ln}, for instance wavenumbers $n = 16$ (green curve) and $n = 200$ (gray curve), and at the same time to incorporate enough short-term fluctuations of $\dot{K}_{ln}/K_{ln}$ (Fig. 12c), such as to improve the signal-to-noise ratio.

3.7 Backscattering

The instantaneously derived contributions to the spectral KE budget do not necessarily resemble the time averaged contribution. In fact, in most cases KE is also instantaneously transferred in the opposite direction, although only within a small wavenumber range. In Fig. 14a the instantaneously generated curves of the horizontal advection contribution to the KE budget for all snapshots are shown in gray with one particular snapshot shown in blue, the time averaged contribution is shown in black. There are several streaks of a negative contribution, i.e. around total wavenumbers $n \approx 240$, $n \approx 280$, and $n \approx 310$. Here, KE is transferred toward smaller wavenumbers, which can be also interpreted as backscattering of KE, i.e. small parts of the downscaled KE are transferred back upscale (Berner et al. 2009).

The evolution in time of the horizontal advection contribution is shown in Fig. 14b. The aforementioned streaks of upscale KE transfer are colored in blue while the downscale KE transfer is colored in yellow and red. As can be seen

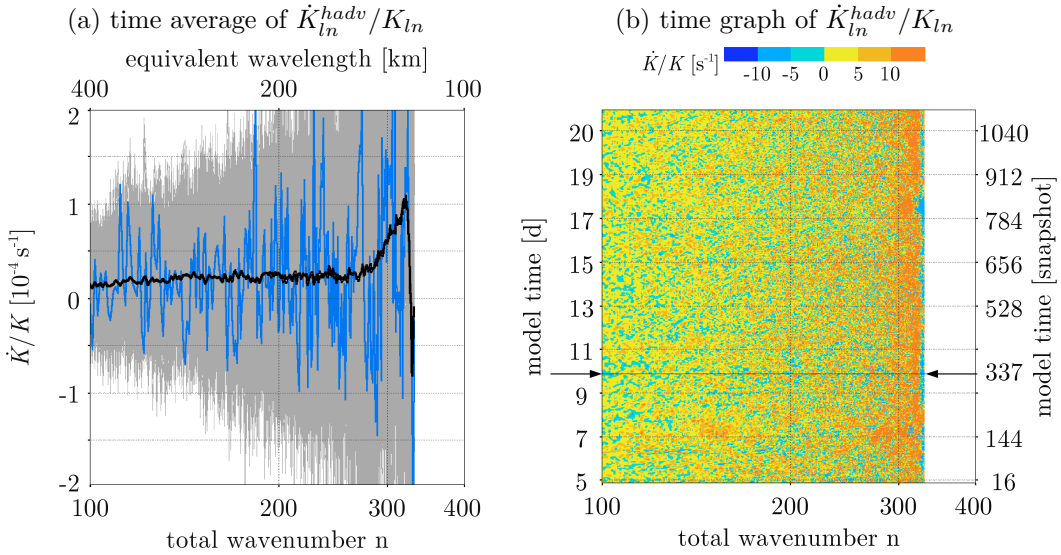

Fig. 14: Contribution of horizontal advection to the spectral KE budget from KMCM T330L100 at 229 hPa (11 km) for 1104 snapshots comprising 17 model days: (a) Spectra of each individual snapshot (gray), selected individual spectrum of snapshot 337 in blue, average spectrum in black, (b) Time-wavenumber map over all snapshots, the position of snapshot 337 is indicated by the solid line.

in Fig. 14b, an upscale KE transfer is very likely to occur at any model time. However, at the same time the downscale KE transfer not only dominates the average picture, black curve in Fig. 14a, but also any particular model snapshot, i.e. most wavenumbers show a positive contribution of horizontal advection to the KE budget (dominating yellow and red colors in Fig. 14b).

Thus the KMCM consistently generates backscattering, although this happens on rather short time scales and extends over a limited wavenumber range only. The downscale KE transfer is dominating in such a way that in the averaged picture no backscattering can be diagnosed.

3.8 Comparison of KMCM model runs in the troposphere

The simulation of the whole atmosphere up to the lower thermosphere was realized using the T210L190 model setup. The two simulations using a T330 spectral truncation were dedicated to the troposphere and lower stratosphere with a better horizontal resolution of the mesoscales and, with the T330L100 setup, also with a drastically improved vertical resolution. The latter setup provides the

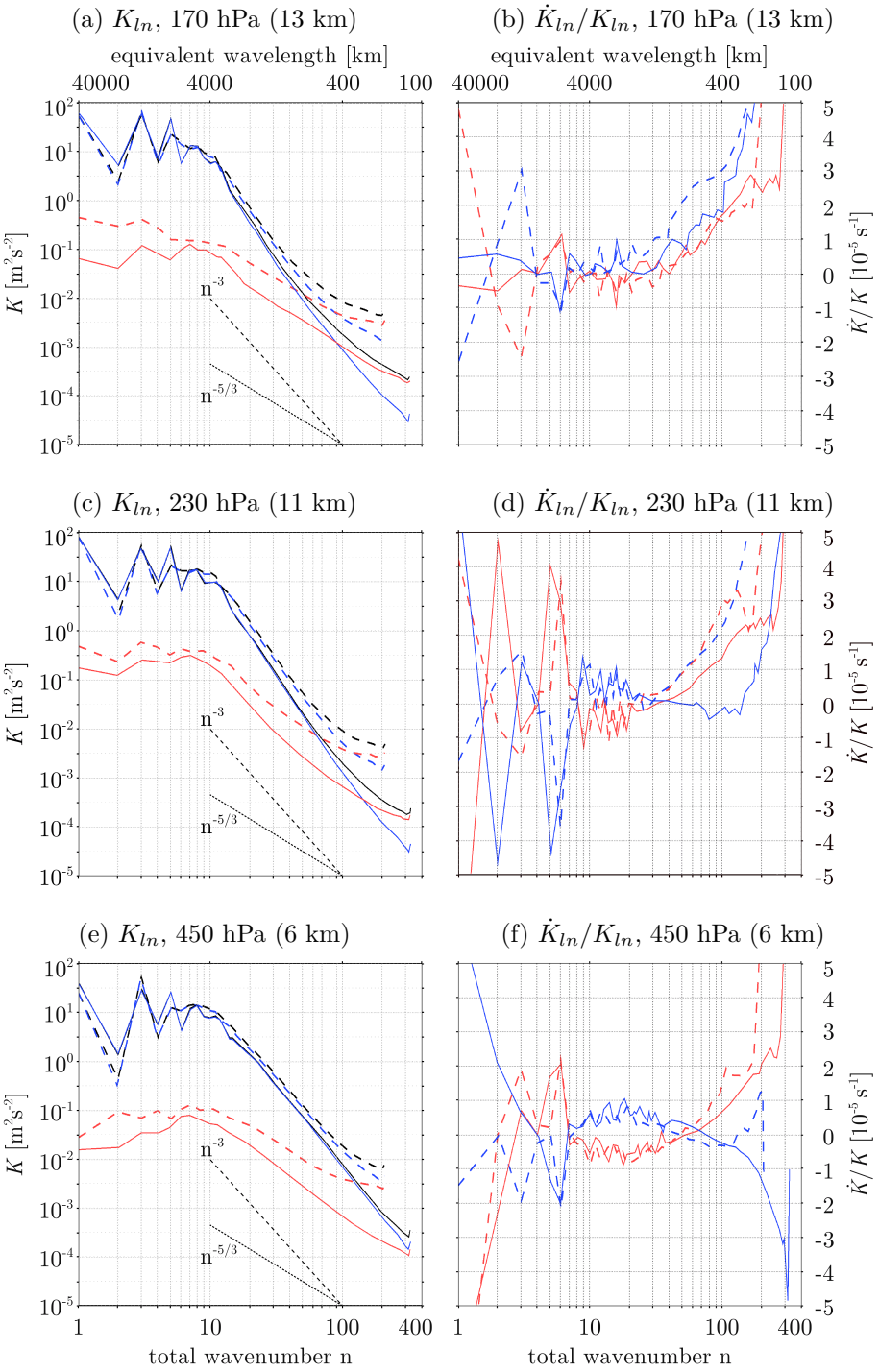

Fig. 15: Comparison of KMCM T210L190 (dashed curves, 16 day average) and T330L100 (solid curves, 17 day average) for the lower stratosphere (170 hPa, 13 km), the upper troposphere (230 hPa, 11 km) and the mid troposphere (450 hPa, 6 km), left: K_{ln} (black) and its rotational (blue) and divergent (red) components, right: Contributions of horizontal advection (red) and adiabatic conversion (blue) to $\dot{K}_{ln}/K_{ln}$.

main data for our interpretation in the troposphere while the T210L190 setup is used for the stratosphere and mesosphere. In order to motivate our analysis of different model setups in Chapter 4, Fig. 15 presents an overview of the spectra and budgets at three levels.

Let us consider first the horizontal kinetic energy spectra of the T210L190 and T330L100 runs on the left-hand side of Fig. 15. Immediate attention is attracted by the fact that the T210L190 run (dashed curves) is always more energized than the T330L100 run (solid curves) for scales smaller than the synoptic scale, this also applies both to the spectra of the rotational and divergent components. However, the transition wavenumber n_T, where both components have the same size, does not seem to depend too much on the setup. It is moving toward smaller wavenumbers with height in both runs equivalently. The different spectral regimes can be easily retrieved from either run.

Looking at the horizontal advection and adiabatic conversion contributions to the spectral budget on the right-hand side of Fig. 15 a somewhat different picture arises. In the mid troposphere (480 hPa, Fig. 15f) and especially in the lower stratosphere (170 hPa, Fig. 15b) the curves look qualitatively similar. In the upper troposphere at 230 hPa (Fig. 15d) this applies only for the horizontal advection. The adiabatic conversion contribution differs considerably for $n > 40$. We will see later that it is within the upper troposphere where this contribution changes sign and obviously this is captured differently in the two runs.

It should be noted that the horizontal advection contribution is consistent for all three levels and both runs. The scales where it is negatively and positively contributing to the kinetic energy and absolute values are approximately the same. The other contributions are not displayed here but show a similar behavior. Therefore the interpretation of the middle atmosphere on the basis of T210L190 data benefits from the use of the higher resolution T330L100 data in troposphere and lower stratosphere.

While the T330L100 run provides the basis of our interpretation in the troposphere and lower stratosphere, the T330L30 run is primarily dedicated to the comparison with results from other models, i.e., the analysis of the SKYHI model by Koshyk and Hamilton (2001). The main differences lie in the vertical resolution, in the UTLS about 250 m for L100 and about 1300 m for L30, and in the momentum diffusion, which is generally smaller in the L30 setup to properly

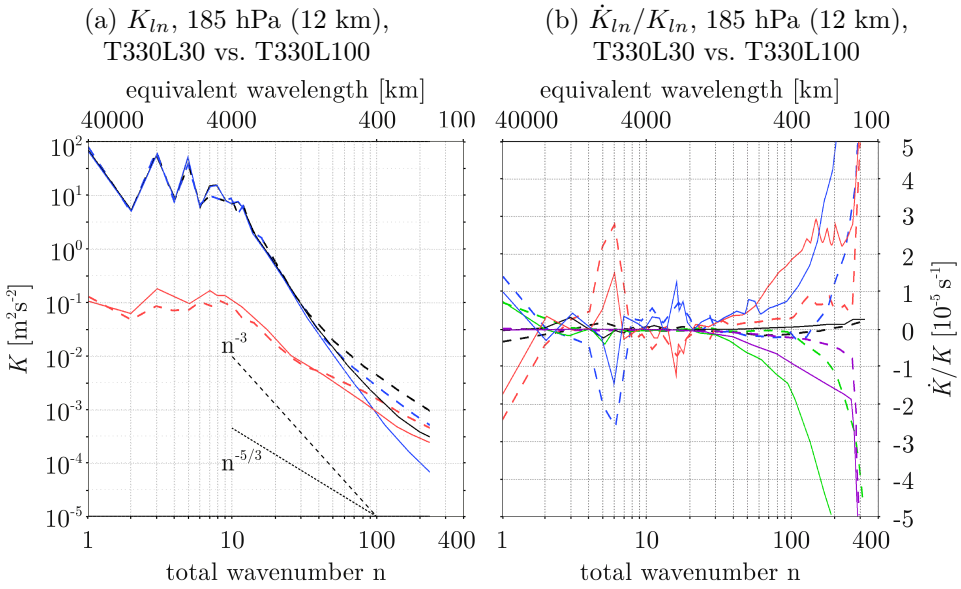

Fig. 16: Comparison of KMCM runs for 185 hPa (12 km): T330L30 (dashed curves) and T330L100 (solid curves). On the left the rotational (blue) and divergent (red) component of the horizontal kinetic energy (black) are displayed, on the right following contributions to the spectral kinetic energy budget (total budget in black) are shown: horizontal advection (red), vertical advection (green), adiabatic conversion (blue), momentum diffusion (purple).

mimic the real atmosphere. For the purpose of an extended examination of the spectral kinetic energy budget in context with the quasi-geostrophic two-layer model of Tung and Orlando (2003), we also run a second T330L30 setup with a substantially larger momentum diffusion. The interpretation of this run can be found in Brune and Becker (2012). Hence, we will not refer to this run within our study, but use the standard diffusion T330L30 only for our interpretation.

The runs are compared among each other in Fig. 16. The level of 185 hPa (12 km) is in both model setups equivalent to the uppermost troposphere, near the tropopause. The spectra for the T330L100 run (solid) in Fig. 16a are less energized than those for the T330L30 run (dashed). Also the mesoscale contributions to the KE budget are generally larger in the T330L100 run (Fig. 16b), whereas the synoptic scale contributions do not differ much and the planetary scale contributions show increased values for the T330L30 run. The purple curves in Fig. 16b, representing the total momentum diffusion, nicely show that the T330L100 run

(solid) corresponds to a larger diffusion, especially in the mesoscales, than the T330L30 run. This is ultimately due to its increased vertical resolution.

From the last paragraph it becomes clear that the momentum diffusion directly influences the KE spectra and the KE budget, especially in the mesoscales. However, the decrease in vertical level spacing seems to be at least equivalently important since the shape of the kinetic energy spectra is substantially altered. As can be seen in Fig. 16a, both the rotational and divergent kinetic energy spectra approach straighter slopes for the T330L100 run. The rotational component does not show the substantial change to a shallower regime as it does for the T330L30 run. In this sense the T210L190 run, compare Fig. 15a with Fig. 16a, can be seen as being in between T330L100 and T330L30, although it has to be run with a yet more different diffusion due to the coarser horizontal resolution.

For the model level at 185 hPa it can be concluded that the three model runs yield qualitatively similar results for the contributions to the kinetic energy budgets, with the absolute values depending on the momentum diffusion applied. In addition, the spectral kinetic energy and especially its rotational component may heavily depend on the spatial resolution of the model, at least the change of the vertical level spacing from 250 m to 1300 m at T330 spectral truncation seems to be quite crucial for the details of the spectrum.

These findings and results from other model levels will be discussed in Chapter 4 in order to interpret the tropospheric kinetic energy cascade.

4 Results

In this chapter the results of the analysis will be presented in detail. They will be compared with both experimental and theoretical findings, and we will discuss the underlying physical processes. This chapter is divided into two parts. The first covers the troposphere and lower stratosphere (TLS) region, where most of the kinetic energy is injected into the model and where most of the atmospheric mesoscale waves are generated. The second part covers the stratosphere and mesosphere or middle atmosphere (MA). The kinetic energy of the MA is not subject to any particular injection range, except for the adiabatic generation by the quasi-2-day and quasi-5-day waves in the summer mesopause region. Instead it is dynamically controlled by the interaction of vertically propagating waves of all scales with the mean flow and it is therefore strongly dependent on wave generation in the troposphere and the background conditions in the MA. It is furthermore also clear that both regions are interactively coupled (Baldwin and Dunkerton 2001).

The KE spectrum with the rotational and divergent components and the spectral KE budget, as well as spectral fluxes of energy and enstrophy have been calculated for all model levels. Throughout the preceding sections only selected examples have been shown to aid the explanation of the analysis. In this chapter only those with the highest importance for interpretation will be shown. A larger collection of spectra and vertical cross sections can be found in Appendix E.

Throughout this study the kinetic energy is treated as kinetic energy *per unit mass*, in order to allow for easy comparison of different model levels. Let us deviate from this only once to demonstrate the actual importance of the kinetic energy input into the model. Figure 17 juxtaposes the kinetic energy per unit mass on the left-hand side and the kinetic energy per unit mass times pressure, which stands for the actual kinetic energy per volume, on the right-hand side in vertical cross sections from the boundary layer up to the lower thermosphere. Although it may be trivial, we would like to point out that the tropospheric baroclinic range, total wavenumbers five to ten, contains only a local maximum in the kinetic energy per unit mass cross section in Fig. 17a, but it in fact represents the overall maximum in the cross section of the kinetic energy per volume in Fig. 17b. Here, the middle atmosphere and especially the mesosphere is negligible.

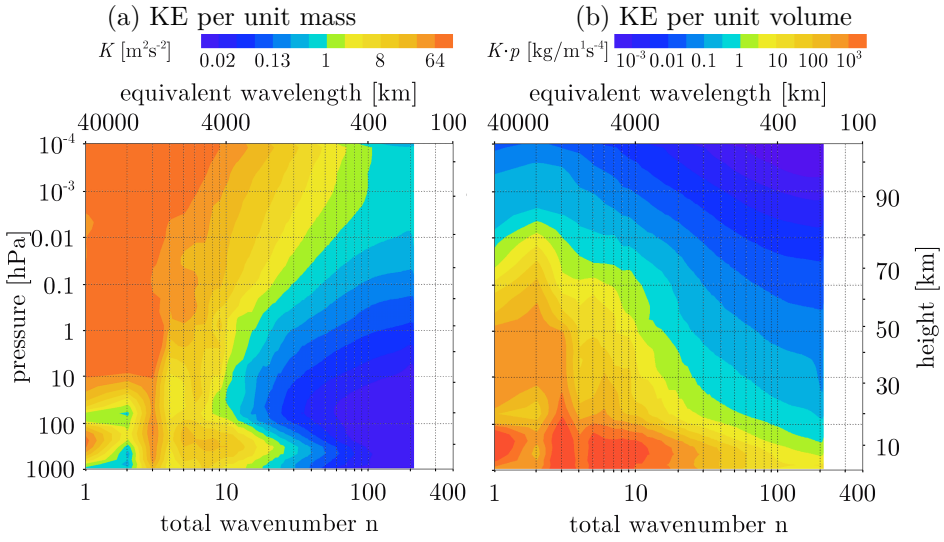

Fig. 17: Vertical cross section of (a) kinetic energy per unit mass, and (b) multiplied by the actual pressure from KMCM T210L190 averaged over 16 model days.

This underscores the paramount importance of the injection of kinetic energy due to the breaking of baroclinic waves in the troposphere.

4.1 Troposphere and lower stratosphere (TLS)

The middle and upper troposphere is the region where most of the kinetic energy is injected, with the maximum located at around 300 hPa (9 km), see Figs. 17b and 18. Also the main dynamical sources of mesoscale waves are located in this layer. These waves may not be the most important factor for the kinetic energy in the TLS itself but they definitely have a major impact on the MA.

In the TLS the model results can well be compared to other data, from both observational and model analysis. The interpretation mainly focuses on the energy and enstrophy cascades from the baroclinic scale of kinetic energy injection toward both the larger planetary scale and the smaller synoptic and mesoscales in the context of macroturbulence. Hereby special attention will be paid to the application of quasi-geostrophic theory and the concept of stratified turbulence.

The T330L100 simulation forms the basis of the interpretation and will be used to test the concept of stratified turbulence of Lindborg (2006). Additionally, the results of the T330L30 setup will be compared with the results of Koshyk

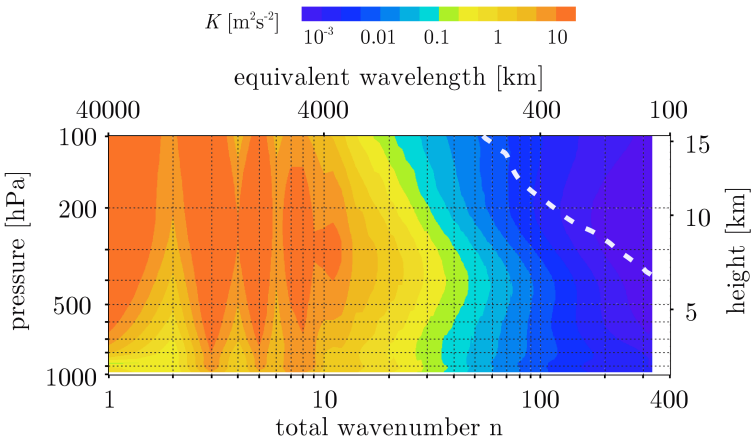

Fig. 18: Vertical cross section of the spectral horizontal kinetic energy K_{ln} from KMCM T330L100, averaged over 17 days, for the troposphere and lower stratosphere. The dashed gray contour shows the transition wavenumber n_T where $K^{\xi}_{ln_T} = K^{\delta}_{ln_T}$.

and Hamilton (2001) for the SKYHI model and of Hamilton et al. (2008) for the AFES model. The T210L190 run, which simulates the atmosphere up to the lower thermosphere, will be compared to results from ECMWF's IFS model T213L31.

4.1.1 Comparison with observational and assimilated data

In Fig. 19 we compare the results of the T330L100 run for the upper troposphere (power spectral density of horizontal wind, averaged from 45°N to 45°S and from 300 to 150 hPa, 9 to 13.5 km height) with the spectra of meridional and zonal wind from Nastrom and Gage (1985). These are results from the Global Atmospheric Sampling Programme (GASP) with aircraft flight paths mostly in the northern mid latitudes and to lesser extent in the Asian-Oceanian tropics at heights between 9 and 14 km.

For the synoptic scales the simulated spectral slope assumes values slightly larger than -3. In the mesoscales the absolute power spectral density is underestimated in our model when compared to Nastrom and Gage (1985), but the spectral slope fits well to -5/3. In this averaged picture the transition from one spectral regime to the other occurs at wavenumbers between 100 and 200 corresponding to 200 to 400 km wavelength. As already pointed out in Section 3.6.2, the transition wavenumber n_T depends strongly on height in our model. This is

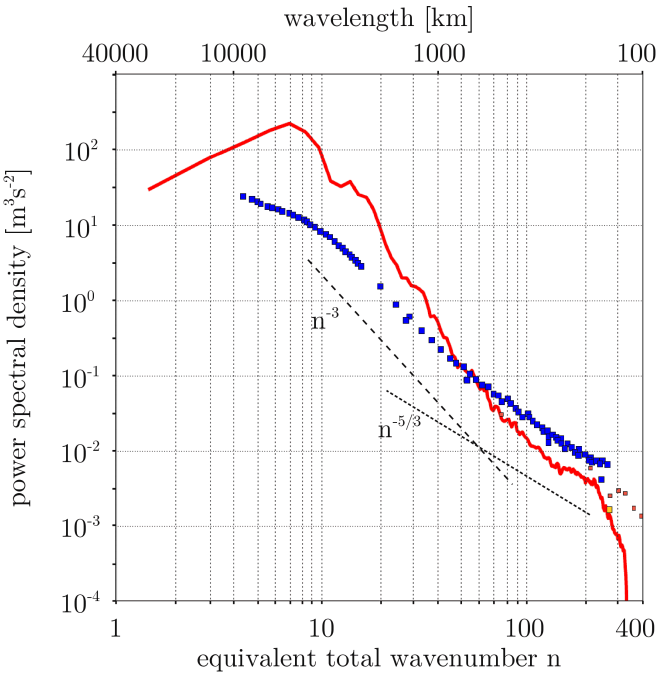

Fig. 19: Comparison of spectral density of the zonal wind (blue, orange, yellow squares), adopted from Fig. 3 of Nastrom and Gage (1985) and divided by Earth's radius, with the power spectral density of the horizontal wind (red solid line) from KMCM T330L100, averaged from 45°N to 45°S and from 300 to 150 hPa, see also Section 3.6.1.

illustrated in Fig. 18, where n_T (white contour) is shown together with K_{ln} for the troposphere and lower stratosphere. There is a strong decrease in n_T from $n_T \approx 300$ at 300 hPa (9 km) to $n_T \approx 70$ at 150 hPa (14 km), just across the layer the GASP data were mainly derived from and where wavelengths shorter than 300-400 km ($n = 100$) exhibit a -5/3 slope (blue squares in Fig. 19). Thus the model captures the transition in a satisfactory way.

We also analyzed 12h-forecast data from the European Centre for Medium Range Weather Forecast (ECMWF), computed with a comparable horizontal resolution: T213L31. The data were taken in 6h intervals from December 1997 to February 1998, thus comprising 360 wintertime snapshots. Note that ECMWF's IFS model yields spectral quantities which can be directly compared to the KMCM results. As shown in Fig. 20 the planetary and synoptic scales are represented in the same manner by both models. However, the shallow slope in the mesoscales is only visible for the KMCM. The ECMWF model strongly un-

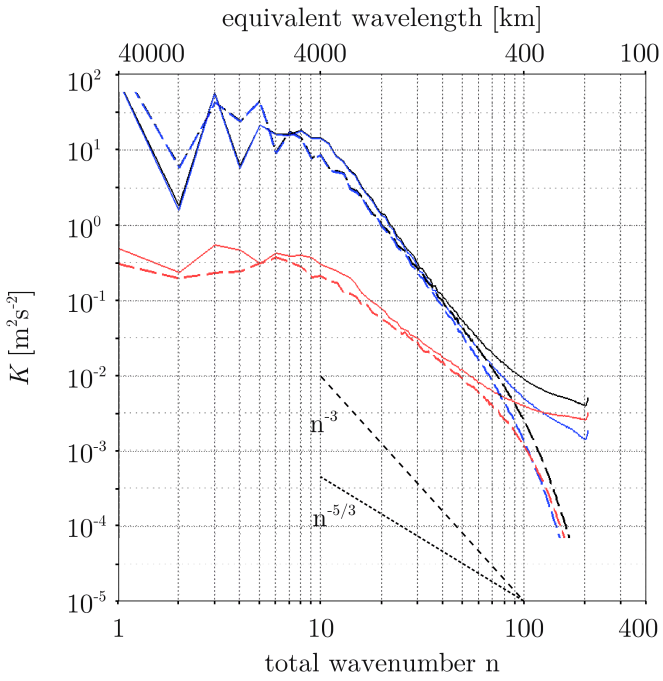

Fig. 20: Horizontal kinetic energy spectra at 230 hPa (11 km) from the KMCM T210L190 run (solid lines, averaged over 16 days) and from ECMWF IFS T213L31 12h forecast data (dashed lines, averaged over January 1998), black: total K_{ln}, blue: rotational modes, red: divergent modes.

derestimates the power in the mesoscales and especially that of the divergent component. In other words, the KE of the mesoscales is very efficiently damped within the ECMWF model.

Interestingly, the findings for the kinetic energy spectrum in the planetary to synoptic scale ($n < 30$) can also be confirmed when comparing the KMCM results with the work of Boer and Shepherd (1983), who analyzed assimilated data from the FGGE-IIIa global dataset (First Global atmospheric research program Global Experiment) separately for January and July 1979. Moreover, they analyzed the resolved spectral fluxes of kinetic energy and enstrophy as well. The spectral fluxes from the present analysis agree at least qualitatively with Boer and Shepherd (1983). A corresponding comparison is shown in Fig. 21. The kinetic energy flux (blue curves) is dominantly negative in the planetary and slightly positive in the synoptic scales, where the enstrophy flux (red curves) is dominantly positive.

The aforementioned comparisons show that the KMCM more or less realistically captures the kinetic energy input at the baroclinic scale. It also realistically

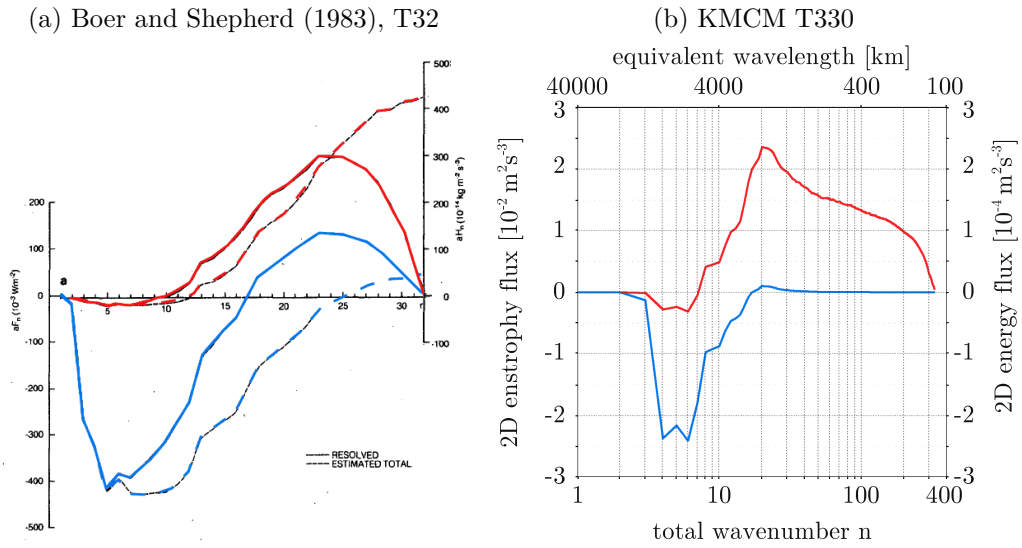

Fig. 21: Kinetic energy (blue) and enstrophy (red) fluxes (a) adopted from Boer and Shepherd (1983), their Fig.13, resolved fluxes solid curves, their "estimated total fluxes" dashed curves, (b) for 230 hPa (11 km) from KMCM T330L100, note the different scaling for the total wavenumber in both panels.

simulates the spectra of the planetary scale, including peaks at the dominant wavenumbers $n = 1, 3, 5$, as well as the synoptic and sub-synoptic scale down to $n \approx 50$. The shallow spectrum in the mesoscales, which is evident from Nastrom and Gage (1985), is at least qualitatively captured. This behavior is in contrast to ECMWF's IFS model, which does not reproduce the mesoscale KE well. It also turns out that the kinetic energy and enstrophy fluxes from the KMCM extend well on the T32 analysis of the FGGE-IIIa dataset analyzed by Boer and Shepherd (1983).

4.1.2 Comparison with other GCM data

The results from the KMCM shall be compared with results from the SKYHI GCM and the AFES (Atmospheric GCM For the Earth Simulator). The SKYHI model has been among the first GCMs from which a larger part of the mesoscale spectrum became available for a comprehensive analysis (Koshyk et al. 1999a; Koshyk and Hamilton 2001). Also, KE spectra in the stratosphere and lower mesosphere could be estimated within the analysis of Koshyk and Hamilton (2001). In terms of horizontal resolution the SKYHI N270 and KMCM T330

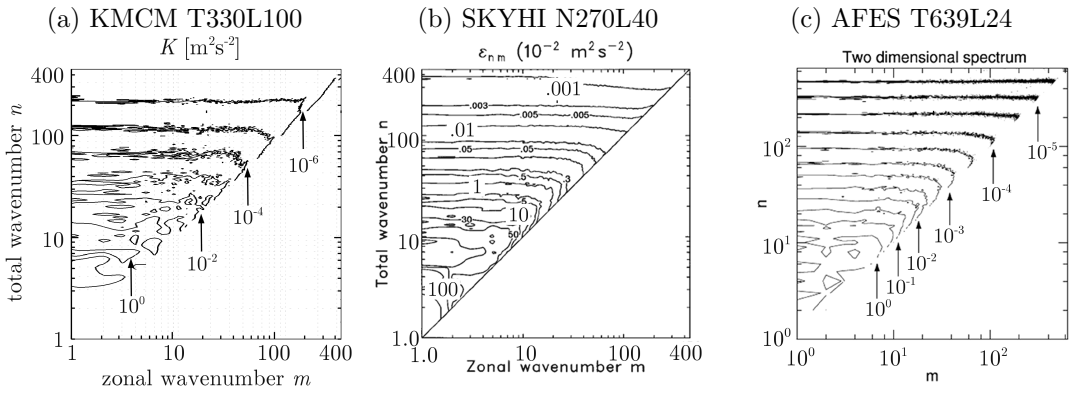

Fig. 22: Full spectral expansion in (m, n) of horizontal kinetic energy in the upper troposphere / lower stratosphere, (a) from KMCM T330L100, averaged over 300-150 hPa, (b) from SKYHI N270L40, averaged over 353-92 hPa, adopted from Koshyk and Hamilton (2001), their Fig. 3, (c) from AFES T639L24 at 200 hPa adopted from Hamilton et al. (2008), their Fig. 2.

are comparable. With a spectral truncation up to T1279 the AFES simulates the mesoscales more comprehensively down to equivalent wavelengths of about 30 km. Here, results from Hamilton et al. (2008) will be used for comparison.

Let us first recall the full spectral expansion (m, n) of K_{lmn} in (11). In the KMCM, Fig. 22a, K_{lmn} is strongly dependent on n and almost independent of m for the mesoscales, $n > 100$, except for the largest zonal wavenumbers for a given n. This also holds true for total wavenumbers $30 \leq n < 100$. That is, K_{lmn} generally decreases strongly with increasing m for $m \approx n$, which corresponds to spherical harmonics with oscillations in the zonal direction only, see Appendix B. In the planetary and synoptic scales ($n < 30$) K_{lmn} is roughly dependent of both n and m. This behavior of the KMCM is fully in line with the findings of Koshyk and Hamilton (2001) in Fig. 22b and of Hamilton et al. (2008) in Fig. 22c.

The total wavenumber spectra of the SKYHI N270L40, AFES T1279L24 DDC (Dry Dynamical Core version) and KMCM are compared in Fig. 23 for the upper troposphere. As already pointed out in Section 3.8, the three KMCM runs exhibit different kinetic energy levels in the mesoscales. All spectra in Fig. 23a exhibit the two slope regime downscale of the baroclinic range, where the slopes vary around -3 and -5/3. There is a good similarity between KMCM T330L30 (green curve) and AFES T1279L24 DDC (red curve) spectra. Note that both runs have very roughly the same vertical resolution. The SKYHI spectrum (blue curve)

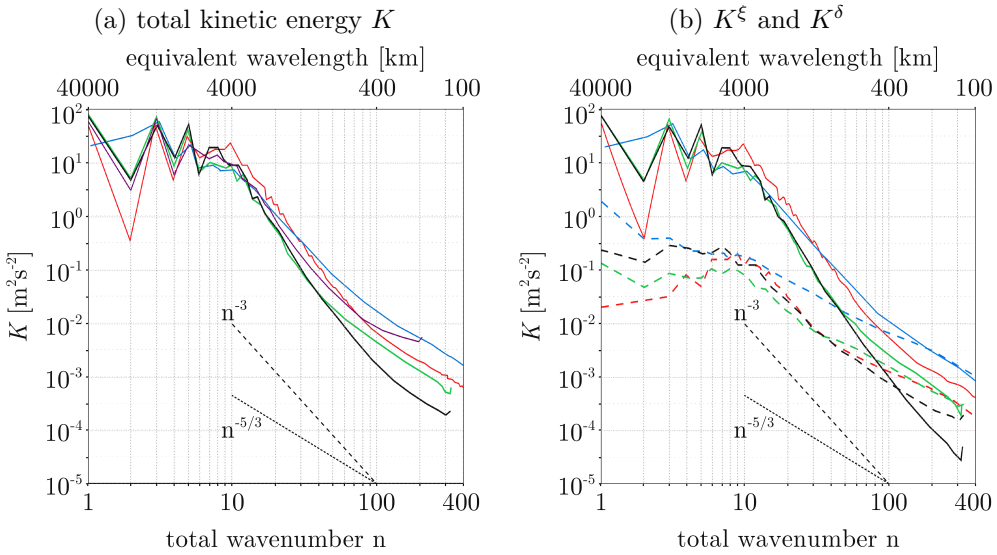

Fig. 23: Comparison of spectra from KMCM T330L100 200 hPa (black), T330L30 186 hPa (green), T210L190 180 hPa (purple) with AFES T1279L24 DDC 200 hPa (red, adopted from Hamilton et al. (2008), their Fig.12) and SKYHI N270L40 averaged upper troposphere (blue, adopted from Koshyk and Hamilton (2001), their Fig.16): (a) total horizontal kinetic energy, and (b) its rotational (solid) and divergent (dashed) components (T210L190 is omitted here).

shows the most energized mesoscales in Fig. 23a. However, keep in mind that the comparison of horizontal grid spacings from the grid-point model SKYHI on one hand with horizontal wavenumbers on the other is not straightforward. In particular the actual total wavenumber n could be smaller for each of the SKYHI values than the plotted, leading to a slightly better correspondence of the spectra. This is more discussed in Appendix B.

The rotational and divergent components in Fig. 23b generally show a similar behavior in terms of the overall shape as well. However, in AFES the rotational components dominate throughout the whole spectrum, in SKYHI there is an approximate equipartition between rotational and divergent components, and in the KMCM T330L100 the divergent kinetic energy even dominates the smaller resolved mesoscales. This behavior is to a lesser extent also seen in the T210L190 run, Fig. 15a, which shows it clearly for the mesoscales. The coarse resolution in the T330L30, however, is more comparable with the AFES T1279L24 DDC model (red curves in Fig. 23).

In general, the simulated spectra agree reasonably well. We confirmed the spectra of SKYHI and AFES with the coarse vertical resolution run T330L30. It turns out that the comparison of the otherwise equivalent high and coarse vertical resolution simulations (T330L100 and T330L30) promises new insight in the macroturbulence of troposphere and lower stratosphere.

The spectral budget is often neglected when the horizontal kinetic energy is analyzed. Besides the work of Boer and Shepherd (1983) on operational data (Section 4.1.1) the study of Koshyk and Hamilton (2001) provides the best opportunity to compare the KMCM spectral budget with. These authors preferred to present an average over the whole upper troposphere, shown in Fig. 24a, which deprives to consider any level by level changes in the contributions to the budget. Although we clearly prefer this level by level analysis due to strong height dependencies of the contributions to the KE budget in the upper troposphere, we also compiled the vertical average which is shown in Fig. 24b for the T330L30 run and in Fig. 24c for the T330L100 run.

Comparing the contributions in Fig. 24 it turns out that the total budget (yellow curve), as well as the contributions from horizontal (orange) and vertical (purple) diffusion assume the anticipated shape in both models: The former stays close to zero for all wavenumbers, the latter two are always negative and decrease even further with increasing wavenumber. Also the horizontal component of the diffusion dominates the smallest scales.

The pressure related contribution (green curves, equivalent to the adiabatic conversion in our analysis) differs considerably. It is by far strongest in the KMCM T330L100 run, and as in the SKYHI, stays positive for all wavenumbers $n > 100$. In the T330L30 run it shows similar magnitudes as the SKYHI model, but the latter does not show neither the slightly negative values in the wavenumber range $100 < n < 200$ nor the steep increase for $n > 300$. Note that here averaged values over the UTLS are discussed. The level by level analysis reveals strong changes of the adiabatic conversion contribution with height in the upper troposphere, as will be discussed further below.

The total advection contribution (red curves) is comparable in the T330L30 and the SKYHI run up to wavenumbers $n \approx 270$. On the contrary the T330L100 run shows a negative contribution of total advection. Here, the key point lies in the vertical advection contribution, which is uniformly negative throughout

(a) SKYHI N270L40

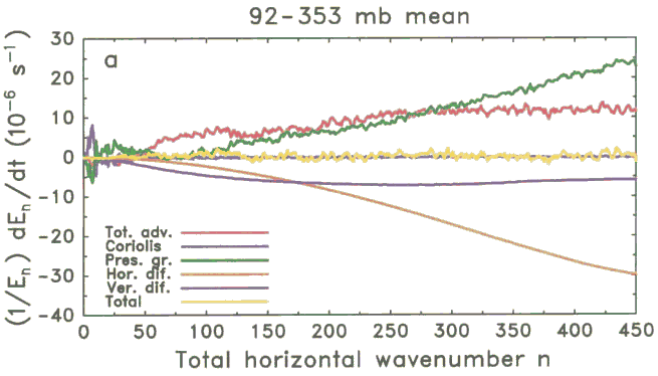

(b) KMCM T330L30

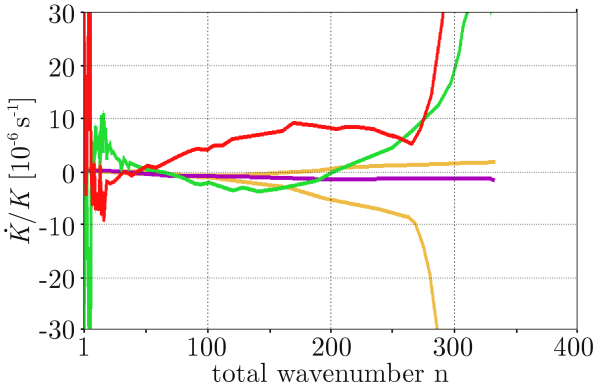

(c) KMCM T330L100

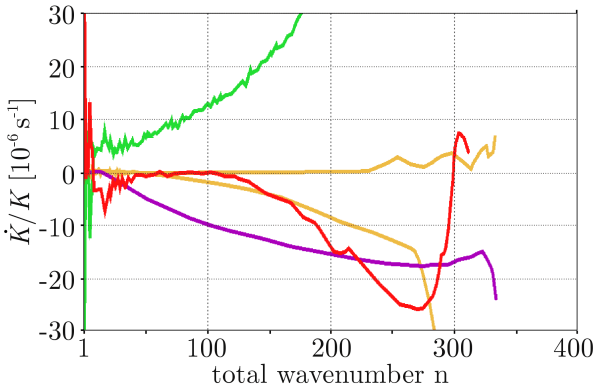

Fig. 24: Comparison of selected contributions to the horizontal kinetic energy budget, averaged over the upper troposphere and lower stratosphere from 353 hPa to 92 hPa (8 km to 17 km): total advection (red), pressure gradient or adiabatic conversion (green), horizontal (orange) and vertical (purple) diffusion, total budget (yellow), (a) SKYHI N270L40 adopted from Koshyk and Hamilton (2001), their Fig.6, (b) KMCM T330L30, (c) KMCM T330L100. Note the linear scaling of the total wavenumber axis.

the UTLS in the KMCM, see Fig. 7d. However, in the T330L100 run it is much stronger than in the T330L30 run, and thus dominates the total advection contribution of the former while the latter is dominated by the positive horizontal advection contribution. These differences can be exemplarily seen in Fig. 16b. The large increase in the total advection contribution for $n > 270$ in both the T330L100 and the T330L30 runs is not seen in the SKYHI analysis in Fig. 24a, where it is rather approaching an approximately constant value for almost all larger wavenumbers. This difference could be due to the diffusion scheme used in the KMCM run which besides an increased horizontal momentum diffusion also results in a dominantly larger horizontal advection contribution.

The comparison of the SKYHI analysis of Koshyk and Hamilton (2001) and the KMCM runs revealed that the contributions to the spectral KE budget show partial agreement in one scale range but at the same time differ substantially in another. The T330L30 run with its coarse vertical resolution is already closer to the SKYHI run, but the different diffusion scheme and perhaps the vertical averaging introduce major differences, especially in the advection and pressure related contributions.

4.1.3 Inertial ranges in the kinetic energy spectrum

The KE spectra of the TLS exhibit several spectral regimes. Hereby the KE injection at baroclinic scales and the KE dissipation at the small-scale end of the resolved spectrum (all levels) and at the large-scale end of the spectrum (levels within the boundary layer) represent the basic ranges. Both are separated well enough to allow for inertial ranges between them. This is especially true from the middle to the upper troposphere. The injection of KE in the spectrum follows the transformation of available potential energy into kinetic energy as described by Lorenz (1955). It occurs at the larger synoptic scales due to the breaking of baroclinic Rossby waves and maximizes between the middle and the upper troposphere.

In Fig. 25 tropospheric KE spectra from the T330L100 run are shown. In the middle troposphere at 518 hPa (5 km) the KE spectrum (black curve in Fig. 25a) allows for two distinctive inertial regimes, the shallow planetary-scale regime and the sub-synoptic and mesoscale regime with an almost uniform slope close to -3. At the same time the rotational components (blue curve in Fig. 25a) dominate

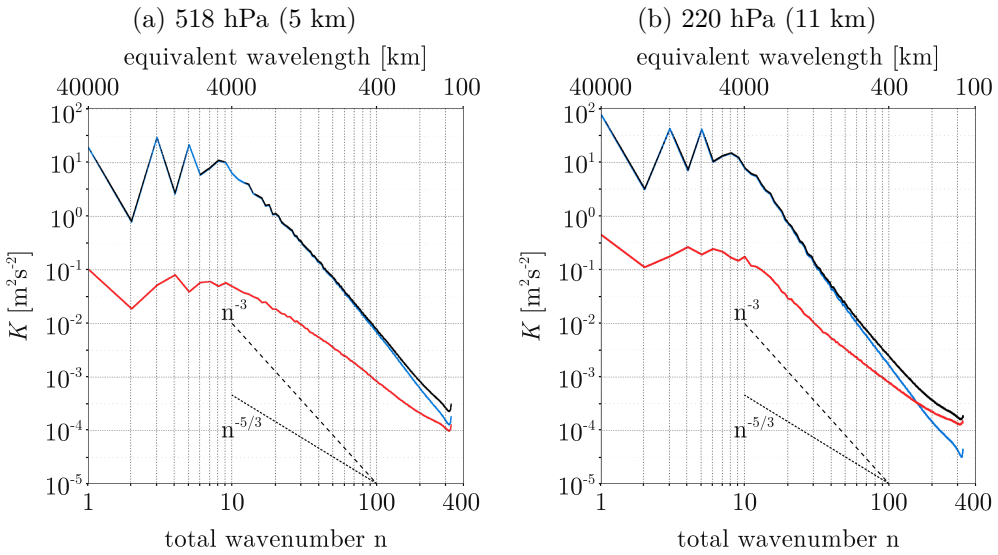

Fig. 25: Kinetic energy spectrum from KMCM T330L100, (a) in the middle troposphere at 518 hPa (5 km) and (b) in the upper troposphere at 220 hPa (11 km), total KE in black, rotational component in blue, divergent component in red.

over the divergent ones (red curve in Fig. 25a) at all wavenumbers. In the upper troposphere at 220 hPa (11 km) a third range can be distinguished in addition to the two already present in the middle troposphere. Here, the small-scale part of the resolved mesoscales clearly exhibits a slope close to -5/3. In this regime the divergent modes dominate over the rotational ones.

The planetary-scale inertial range throughout the TLS does not really display a -5/3 slope as expected from quasi-geostrophic turbulence. These scales are rather dominated by quasi-stationary waves, which prevent a clear slope. This is similar to the findings from the analysis of operational datasets (Boer and Shepherd 1983; Straus and Ditlevsen 1999; Berner et al. 2009), and Fig. 20, as well as of GCM data (Koshyk et al. 1999a; Hamilton et al. 2008), see also the preceding sections. A more conclusive approach is represented by the analysis of the 2D energy flux (blue curve in Fig. 21b), which in the KMCM is negative for the planetary scale and therefore consistent with an upscale 2D energy cascade.

The synoptic -3 regime just downscale of the KE injection range in the TLS resembles what is expected from QG turbulence: The KE spectrum is dominated by a downscale enstrophy cascade. This is strongly supported by the analysis

of the enstrophy flux within the model, which is positive for almost all scales smaller than the baroclinic scale (red curve in Fig. 21b).

In the context of macroturbulence the mesoscale -5/3 regime in the upper troposphere is a result of a downscale horizontal energy cascade, as suggested by the analysis of the quasi-2D and the total spectral fluxes due to horizontal advection, which will be discussed in the next section. It will be shown that the former vanishes in the mesoscales while the latter becomes dominant and positive.

Three theoretical concepts yield such a mesoscale forward energy cascade. The classical Kolmogorov 3D turbulence, however, relies on near homogeneous and isotropic flow. This requirement is definitely not fulfilled for the mesoscales in the TLS. Under the condition of an asymmetric enstrophy distribution between vertical levels, also QG turbulence may be able to generate such a spectral slope. According to Gkioulekas and Tung (2007), an explanation for both the -3 and the -5/3 slope could be found with this concept. However, QG dynamics hardly applies to wavenumbers $n > 200$ or equivalent wavelengths $\lambda < 200$ km.

The concept of stratified turbulence is not as limited in horizontal scales as the two aforementioned theories. The upper tropospheric mesoscale -5/3 slope could be interpreted as the result of stratified turbulence, if in addition to a strongly stratified background, which is met in the TLS (see the calculation of Froude numbers in Section 3.5), inertial and buoyancy forces are of the same order of magnitude (Lindborg 2006), and the vertical resolution is sufficiently high. The present analysis of both forces will show that this is indeed the case for certain regions (both spectrally and vertically) of the upper troposphere. It reveals that the development of stratified turbulence in the upper troposphere strongly depends on a vertical pressure flux from the middle troposphere and with that the KE spectra of the middle and upper troposphere should be interpreted in one and the same context.

4.1.4 Quasi-geostrophic turbulence, stratified turbulence and vertical energy transfer in the troposphere

In the context of stratified turbulence the focus lies on inertial and buoyancy forces, which are represented in the analysis by the contributions of horizontal advection and adiabatic conversion, respectively, to the KE budget. In Fig. 26

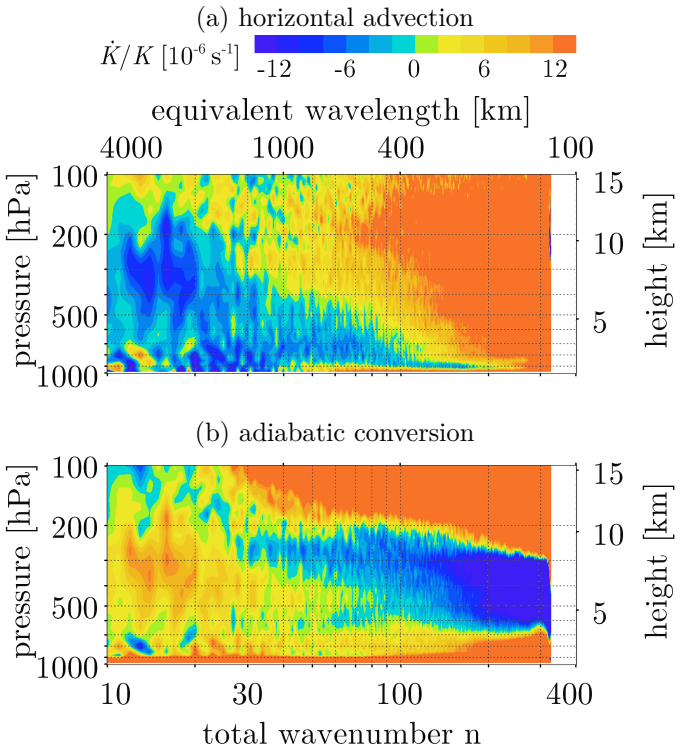

Fig. 26: Contributions to the KE budget of (a) horizontal advection and (b) adiabatic conversion, weighted by KE from KMCM T330L100, averaged over 17 days. Both panels have the same color scale.

these contributions are displayed in a vertical cross section of the TLS. The blue colors indicate a decrease and the red colors an increase of KE in time due to the respective contributions.

It turns out from Fig. 26a that horizontal advection is transferring KE toward the smaller scales at all altitudes. The wavenumber range where this contribution is close to zero changes with height. In the lower troposphere this transition occurs around wavenumbers of $n \approx 100$, in the middle troposphere around $n \approx 70$ and in the upper troposphere around $n \approx 20$. In the lower stratosphere, where KE injection dramatically decreases, the net downscaling due to horizontal advection ceases to be important.

The cross section in Fig. 26b reveals that in the mesoscales KE is decreased in the middle troposphere and increased in the lower and especially in the upper troposphere due to adiabatic conversion resulting from a net vertical pressure flux away from the middle troposphere. This process strongly influences any KE cascade in the tropospheric mesoscales. The interpretation of horizontal KE

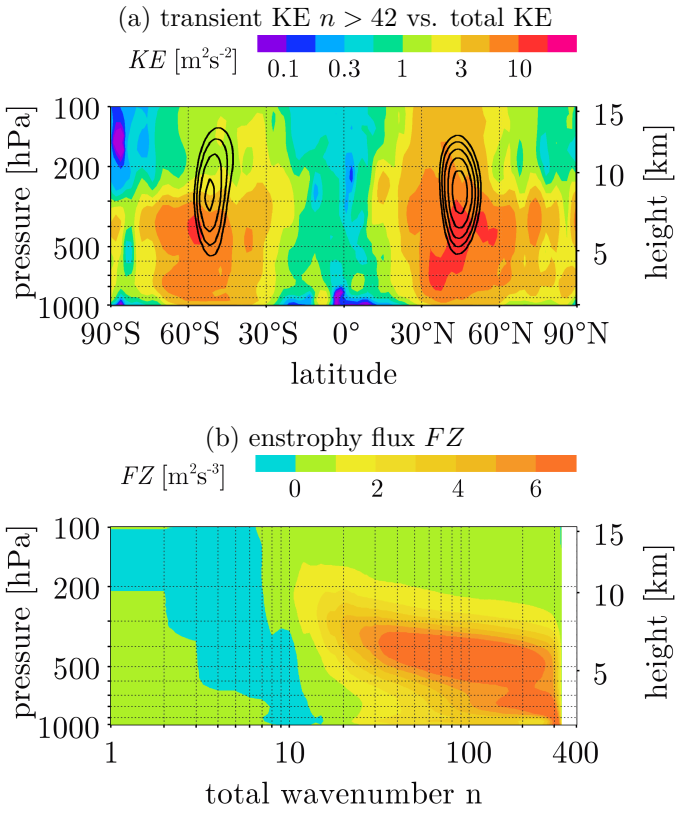

Fig. 27: Vertical cross sections of (a) the zonally averaged mesoscale transient kinetic energy (wavenumbers $n > 42$) together with contour lines of the zonally averaged total kinetic energy (logarithmic contours from 500 to 1000 m^2s^{-2}) and (b) the enstrophy flux FZ_{ln}, from KMCM T330L100, averaged over 17 days, for troposphere and lower stratosphere. The maximum total KE lies in the tropospheric jet around 250 hPa (10 km), the maximum mesoscale transient KE and the maximum enstrophy flux at 500 to 400 hPa (5.5 to 7 km).

cascades has to incorporate this vertical KE transfer, which explains the different mesoscale behavior of the KE spectrum in the middle and upper troposphere, as will be further discussed below.

Although the maximum of KE occurs in the upper troposphere within the tropospheric jet, the mesoscale transient KE has its maximum considerably lower, namely between 500 and 400 hPa as can be seen from Fig. 27a. Also the maximum enstrophy cascade forms at these heights in the middle troposphere as shown in the vertical cross section in Fig. 27b. This can also be seen from Figs. 28a and c, where the enstrophy flux (green curves) in the middle troposphere is considerably larger than in the upper troposphere. Relying on QG turbulence theory for

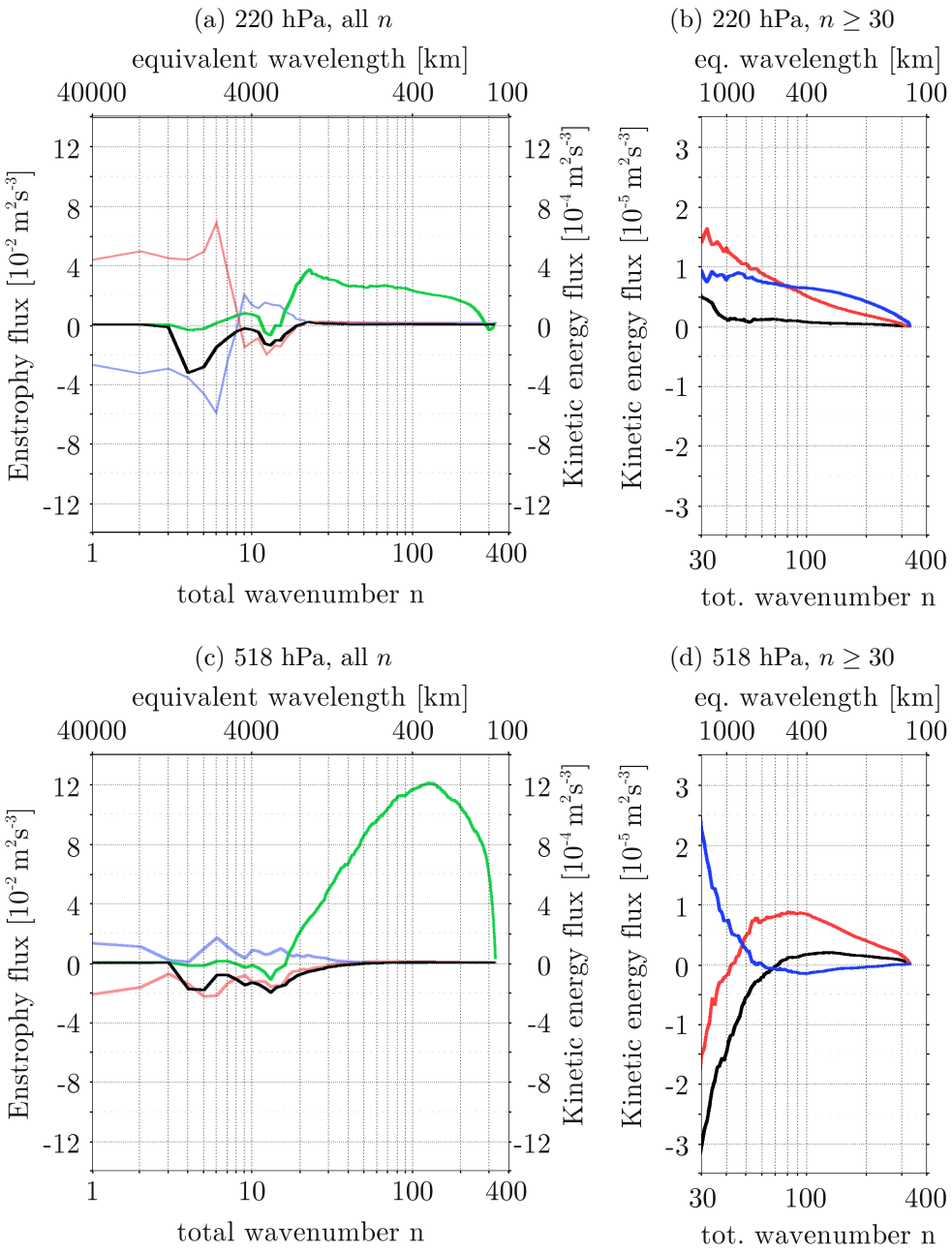

Fig. 28: Enstrophy and kinetic energy fluxes in (a,b) the upper troposphere at 220 hPa (11 km) and (c,d) the middle troposphere at 518 hPa (5 km), enstrophy flux in green, 2D energy flux in black, total energy flux due to horizontal advection (inertial forces) in red, due to adiabatic conversion (buoyancy forces) in blue. The scaling of the whole spectra in (a,c) is 40 times the scaling of the small-scale spectra in (b,d).

the sub-synoptic scales and keeping in mind the mesoscale transient KE as in Fig. 27a, the maximum enstrophy cascade is also accompanied by a maximum energy cascade, though hidden.

The question arises, why this energy cascade does not dominate the mesoscale KE spectrum of the middle troposphere as it does in the upper troposphere. To a large extent the answer lies in the aforementioned vertical pressure flux in the mesoscales due to adiabatic conversion. The KE cascade in the mesoscales of the middle troposphere is decreased by adiabatic conversion which is represented by the blue curve in Fig. 28d and is negative for the mesoscales. Vice versa the KE cascade in the upper troposphere is increased by the vertical pressure flux convergence (positive blue curve in Fig. 28b).

Here, the enstrophy cascade is less powerful. On the contrary, the additional input into the mesoscales due to adiabatic conversion lifts the KE cascade to a level at which it easily dominates the enstrophy cascade, giving the KE spectrum the characteristic -5/3 slope. At the same time, the spectral fluxes due to adiabatic conversion and horizontal advection have the same order of magnitude, allowing for the development of stratified turbulence in the model.

In Fig. 29 the weighted difference between KE fluxes due to horizontal advection (FK^{HA}) and adiabatic conversion (FK^{AC}) is shown in a vertical cross section of the TLS for two different vertical level spacings in the model: T330L100 with a 250 m vertical interval and T330L30 with about 1300 m vertical interval. It becomes clear that the same order of magnitude (blue colors) for the smaller scales is reached only in two narrow vertical bands in the lower troposphere around 850 hPa (1.5 km) and the upper troposphere around 220 hPa (11 km). These are the only regions, where stratified turbulence may be expected to develop in the model. In these regions the vertical pressure flux convergence has its positive maximum, too. Here, vertical advection is not considered.

It is important to mention that the narrow bands of equal order of inertial and buoyancy forces in the TLS consist of about five model levels in the T330L100 run, see again Fig. 29a, which may be sufficient to represent stratified turbulence. The same behavior is also indicated in the T330L30 run, but at one model level only. Although the vertical cross section of the T330L30 run in Fig. 29b looks quite similar to the one of the T330L100 run, any interpretation toward stratified turbulence is flawed, because adiabatic conversion changes sign from the tropo-

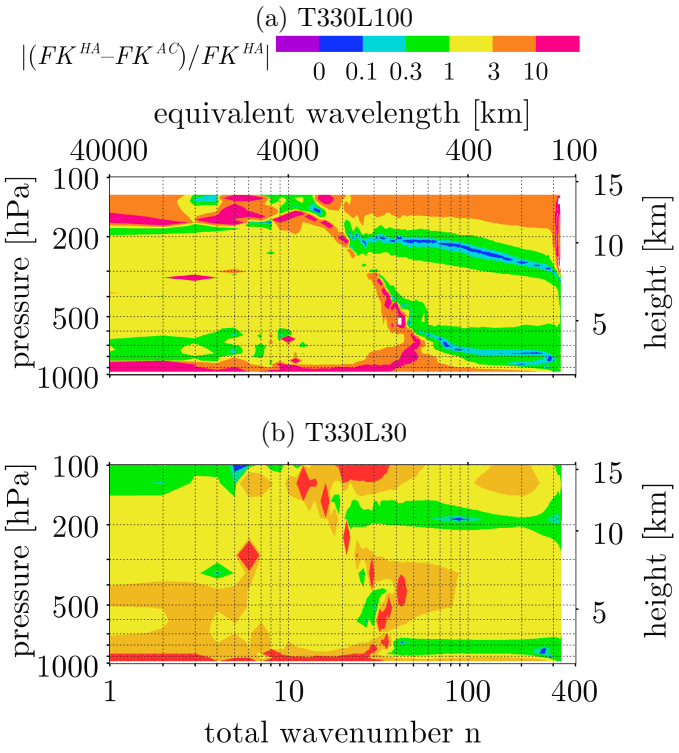

Fig. 29: Weighted difference $|(FK^{HA} - FK^{AC})/FK^{HA}|$ between inertial forces and buoyancy forces in the troposphere for (a) the T330L100 run and (b) the T330L30 run, a value of zero implies a ratio of the order of one. Both panels have the same color scale.

sphere to the stratosphere, whereas horizontal advection stays positive, and as such, one model level has to show something like equally important inertial and buoyancy forces. A vertical level spacing larger than 1 km as in the T330L30 setup is definitely not resolving the development of stratified turbulence. In contrast, the 250 m vertical spacing of levels in the T330L100 setup may be sufficient to allow for stratified turbulence in a narrow altitude range.

The present spectral analysis of the KE budget reveals that stratified turbulence in the upper troposphere (and perhaps in the lower troposphere as well) is very much dependent on the KE injection and the mesoscale adiabatic conversion in the middle troposphere. In fact, as is illustrated in Fig. 30, KE is transferred both spectrally downscale and vertically upward from the baroclinic scales in the middle troposphere to the mesoscales in the upper troposphere.

In the following these results shall be compared in more detail to the findings of Lindborg (2006). His box model is designed to resolve the scales where strati-

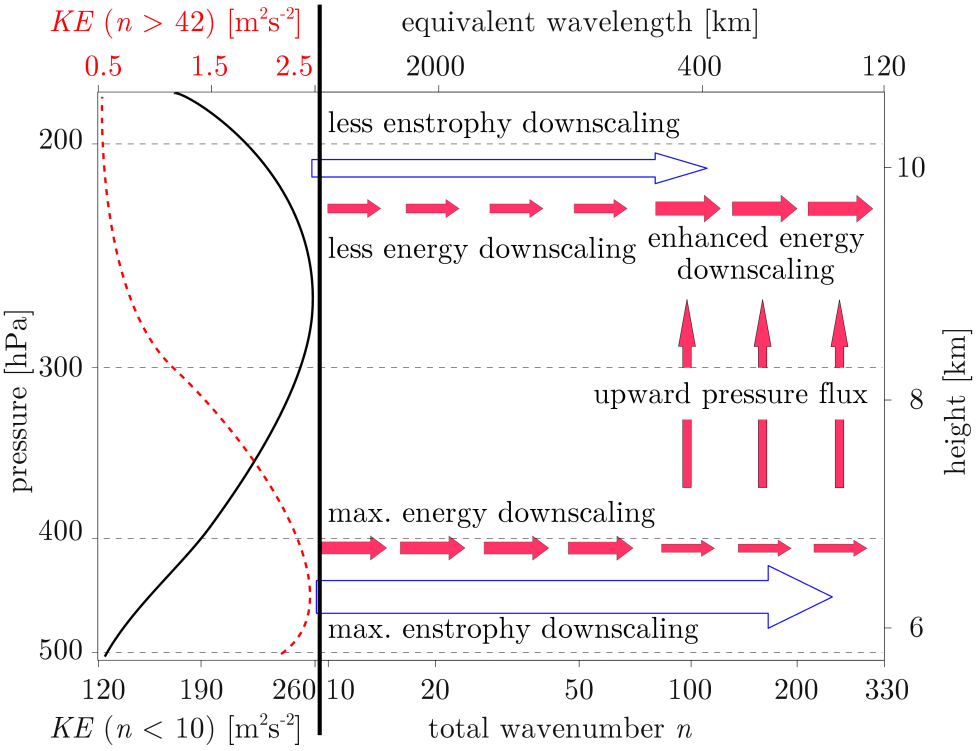

Fig. 30: Schematic of the vertical transfer of synoptic-scale middle tropospheric KE to the upper tropospheric mesoscales due to horizontal downscaling *and* vertical pressure flux in the mesoscales. In the upper troposphere this increases the downscale KE cascade enough, such that it dominates over the enstrophy cascade. This comes to the expense of the middle tropospheric KE cascade, which is decreased and stays hidden behind the enstrophy cascade for all resolved wavenumbers. The panel on the left shows the total large-scale KE (black solid line, $n < 10$) and the total small-scale KE (red dashed line, $n > 42$) from the T330L100 run.

fied turbulence occurs down to the outer scale of 3D turbulence. This implies a vertical grid spacing of $\Delta z \leq 20$ m and a horizontal grid spacing of $\Delta x \leq 500$ m, the overall horizontal extension of the box model being around 400 km. The forcing is applied at the largest scales of the model only, i.e., around 100 km horizontal wavelength, where kinetic energy is injected into the purely two-dimensional horizontal modes. Only a small amount is left for the large-scale vertical modes to trigger initial vertical shear zones, which promote the transfer of KE from the horizontal to the vertical modes. The boundary conditions are periodic in all three dimensions.

In the present mechanistic GCM we apply very high horizontal and vertical resolutions to resolve the large-scale part of the mesoscales. Although we are able to interpret also this mesoscale part of the kinetic energy spectrum, we are still far away from the spatial resolution of Lindborg's box model. Our "forcing" is due to conversion of available potential energy into kinetic energy (Lorenz 1955) in the context of a complete simulation of the Lorenz energy cycle (Becker 2003). In particular, kinetic energy is injected at the baroclinic scale, which is far outside the scales of stratified turbulence. Furthermore, this generation of KE occurs well below the region where the kinetic energy spectrum of the mesoscales is close to a -5/3 slope. The model has, of course, no periodic boundary conditions in the vertical direction.

Compared to Lindborg's box model we want to reflect on two distinctive features which eventually lead to an answer, why we believe to diagnose stratified turbulence in our GCM in a narrow layer within the upper troposphere. First, in the KMCM there is a clear separation both in the horizontal scale and the vertical location between the kinetic energy injection range and the region where stratified turbulence may occur. That means, Lindborg's box model is virtually allocating only a small portion of KMCM's pseudo 2D space (vertical hybrid layers vs. total horizontal wavenumber), namely around the 220 hPa model level and for wavenumbers $n > 100$, with most of it outside of our resolved scales. Second, we diagnose a strong vertical interaction influencing the kinetic energy budget, which stems from adiabatic conversion (see Figs.26b and 30) and would not play a role in Lindborg's model due to the periodic boundary conditions in the vertical.

Current GCMs evidently lack the high spatial resolution, especially in the vertical direction, of Linborg's box model. The T330L100 run of the KMCM does not represent an exception in this respect. Nevertheless this resolution setup is already capable of successfully mirroring the large-scale part of Lindborg's box model, and, together with the vertical interaction within the KMCM, especially the vertical transfer of kinetic energy, this allows for the interpretation of stratified turbulence within the KMCM.

4.1.5 The role of gravity waves in the model troposphere and lower stratosphere

As mentioned earlier the KMCM has been specifically designed to allow for self-consistent generation, propagation, and dissipation of GWs within the resolved scales. The model setups allow for both inertio-GWs and mid-frequency GWs to develop. Some of these vertically and horizontally propagating GWs can already be seen in snapshots of the T210L190 run. Such a snapshot is displayed in Fig. 6, demonstrating that GW events may not be confined to the TLS region. An extended diagnosis of GWs in the middle atmosphere will be given in Section 4.2. It is expected, however, that a large portion of the GWs generated in the troposphere do not leave the TLS. Those will be subject to the following considerations.

In addition to Fig. 6, the snapshot of a T330L100 run as shown in Fig. 31 displays even more evidence of GWs within the TLS. Moreover, the vertically propagating waves between 20°W and 40°W in Fig. 31b, which are presumably generated by the breaking Rossby wave over the Northern Atlantic evident in Fig. 31a, are confined to the TLS. The lower one of the two wave trains stays within the lower troposphere, the upper one reaches to the lower stratosphere at 100 hPa (16 km).

In contrast to the snapshots in grid-space, the analysis of the KE spectrum does not directly show the contributions of GWs. The divergent component of the KE is often attributed as a proxy for GWs (Koshyk and Hamilton 2001). Although this is a rather crude estimate, it is worthwhile to consider the height-dependence of the spectral KE budget from this perspective.

On the one hand the T330L100 spectra exhibit a rather strong divergent component, especially in the upper troposphere, whereas on the other hand the T330L30 spectra do not, see Figs.32 and 16a. Nevertheless, in both runs some 20 to 30 % of the total KE of the mesoscales are represented by the divergent component throughout the whole troposphere, which as a first approximation could be taken as an estimate for the maximum importance of GWs with respect to the general mesoscale tropospheric KE spectrum. However, it is only in the T330L100 run that, starting from 300 hPa (9 km) upward, the divergent component contributes more than 50 % to the mesoscale KE. The better vertical resolution of this run allows a larger part of the GW spectrum, particularly waves with larger

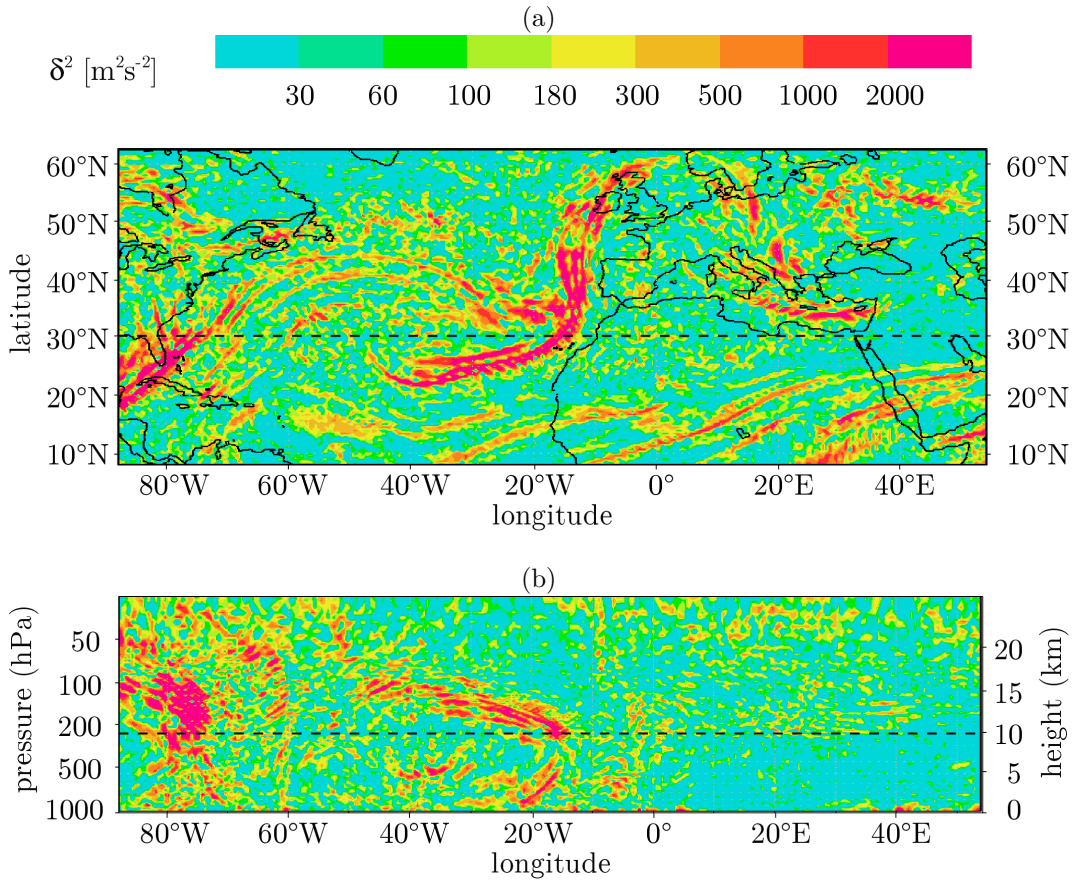

Fig. 31: Squared divergence from one snapshot of KMCM T330L100 for the Northern Atlantic region: (a) map view at 220 hPa (11 km), (b) cross section at 30°N.

vertical wavenumbers, to develop. The T330L30 setup, in contrast, biases the shorter vertical wavelengths, which are not resolved, toward longer wavelengths. In other words, the resolved GW spectrum is artificially shifted toward higher frequencies with a nevertheless too strong contribution of the rotational flow.

Another possibility to assess the role of GWs is the analysis of the KE budget. For this reason let us have a look at the GW kinetic energy equation, which is explained in more detail in Appendix C. We rearrange (C.10) such that the GW kinetic energy can be expressed as:

$$\overline{\mathbf{v}' \cdot \partial_t \mathbf{v}'} = -\overline{\mathbf{v}' \cdot (\overline{\mathbf{v}} \cdot \nabla)\, \mathbf{v}'} - \overline{\mathbf{v}' \cdot w' \partial_z \overline{\mathbf{v}}} - \overline{\mathbf{v}' \cdot \frac{\nabla p'}{\rho_r}} + \overline{\mathbf{v}' \cdot \mathbf{R}'}\,, \tag{37}$$

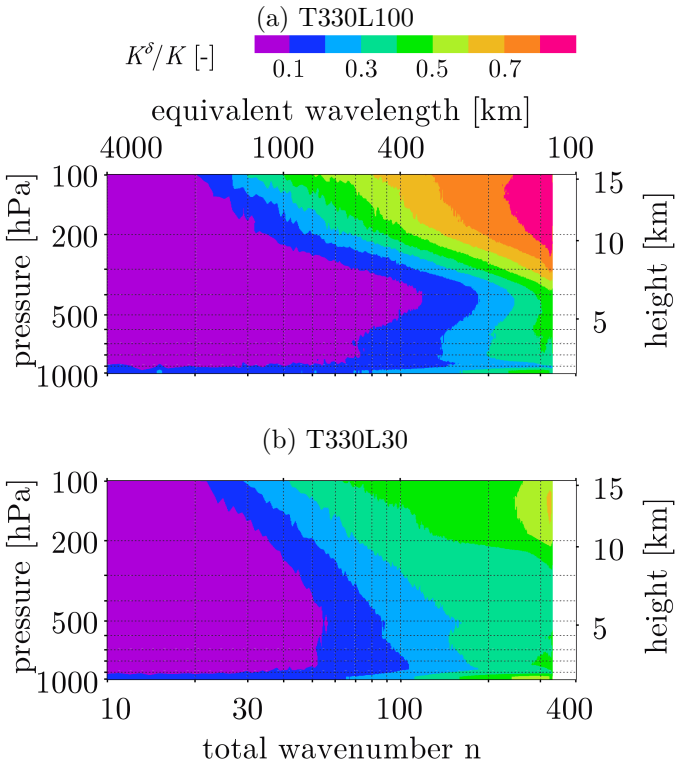

Fig. 32: Ratio of the divergent component of KE and the total KE for (a) the T330L100 run and (b) the T330L30 run. The color scale is the same for both panels.

and substitute the first term on the right-hand side of (37) $-\overline{\mathbf{v}' \cdot (\overline{\mathbf{v}} \cdot \nabla)\, \mathbf{v}'}$ with $-\overline{\mathbf{v}} \cdot \nabla(\overline{\mathbf{v}'}/2)$:

$$\overline{\mathbf{v}' \cdot \partial_t \mathbf{v}'} = -\overline{\mathbf{v}} \cdot \nabla \left(\frac{\overline{\mathbf{v}'}}{2} \right) - \overline{\mathbf{v}' \cdot w' \partial_z \overline{\mathbf{v}}} - \overline{\mathbf{v}' \cdot \frac{\nabla p'}{\rho_r}} + \overline{\mathbf{v}' \cdot \mathbf{R}'}\,. \tag{38}$$

Note that $\overline{\mathbf{v}}$ is the horizontal velocity of the mean flow, the primed variables are associated with the GWs. In (38), the first, second and fourth term on the right-hand side, representing horizontal and vertical advection and momentum diffusion all describe the interaction of the GW scale with the other scales, namely the larger non-GW scales and the subgrid scale. The third term, the adiabatic conversion, represents the vertical exchange of KE within the GW scales. This has already been important for the interpretation of stratified turbulence. In the

climatological mean the left-hand side is zero and thus the adiabatic conversion term is balanced by the total advection and the momentum diffusion:

$$-\overline{\mathbf{v}' \cdot \frac{\nabla p'}{\rho_r}} = \overline{\mathbf{v}} \cdot \nabla \left(\frac{\overline{\mathbf{v}'}}{2} \right) + \overline{\mathbf{v}' \cdot w' \partial_z \overline{\mathbf{v}}} - \overline{\mathbf{v}' \cdot \mathbf{R}'} \,. \tag{39}$$

Neglecting the vertical advection term for now, the generation of GWs is associated with a negative adiabatic conversion and GW dissipation with a positive adiabatic conversion. Accordingly, in Fig. 26b the blue colored region between 600 and 250 hPa (middle and upper troposphere) is subject to a net GW generation and the red colored regions below (lower troposphere) and above (uppermost troposphere and lower stratosphere) are subject to a net GW dissipation. In other words, in a climatological sense GWs are propagating from the middle troposphere toward the lower troposphere and toward the lower stratosphere, where most of them are dissipated again. Those which make it to the middle atmosphere are of great importance to mesospheric temperatures and the residual circulation. This will be discussed in the following Section 4.2.

4.2 Middle Atmosphere

In terms of horizontal kinetic energy, the lowermost stratosphere as part of the TLS region has already been covered in Section 4.1. At higher altitudes there is essentially no kinetic energy input due to conversion of available potential energy at large scales, as it is the case in the TLS. In the first part of this section we interpret the stratosphere as a passive layer in the sense of wave generation and damping: the energy spectrum is dominated by the interaction of the mean flow with any wave generated at lower levels and propagating into or through the stratosphere. In contrast to the stratosphere, most of the resolved mesoscale waves will dissipate in our model in the mesosphere. Of course, in reality mesoscale waves do also propagate further up into the thermosphere (Hines 1960; Fritts et al. 2008), but their wavenumbers are larger than our model's truncation wavenumber. In the second part of this section we will therefore focus on the energetics of GW breakdown in the upper mesosphere between 75 and 90 km. Our results for the middle atmosphere (stratosphere and mesosphere) are based on the T210L190 run with a vertical hybrid level interval of $\Delta z \approx 600$ m. In

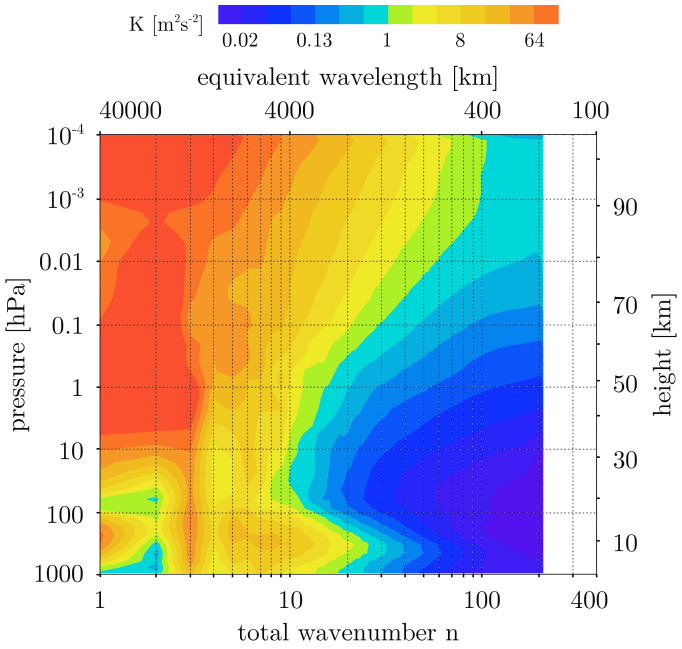

Fig. 33: Vertical cross section of the spectral KE up to the mesosphere from the T210L190 run, averaged over 16 model days.

addition to the spectra selected for display in this section, a more comprehensive collection of graphs and cross sections can be found in Appendix E.

4.2.1 Stratosphere

In Fig. 33 the vertical cross section of the spectral KE up to the lower thermosphere is shown. For the middle stratosphere at 10 hPa (30 km), the KE spectrum is presented in Fig. 34a. This differs substantially from its T330L100 tropospheric counterparts, see Fig. 25. The planetary scales up to $n \approx 5$ are stronger energized with increasing height. In the stratosphere, the rotational part exhibits a slope close to -3 for $10 < n < 25$ and dominates this range. Compared to the troposphere, the divergent part of K_{ln} becomes dominant at smaller wavenumbers ($n_T \approx 25$ at 30 km) and its slope is clearly shallower than -5/3. Furthermore, in the sub-synoptic scales and mesoscales the rotational component does no longer stick to the -3 regime. The latter corresponds to the behavior of the rotational component in the troposphere of the T330L30 simulation, where a coarse vertical resolution has been applied. However, as pointed out earlier, the concept of geostrophic turbulence that applies to the planetary and synoptic scales in the

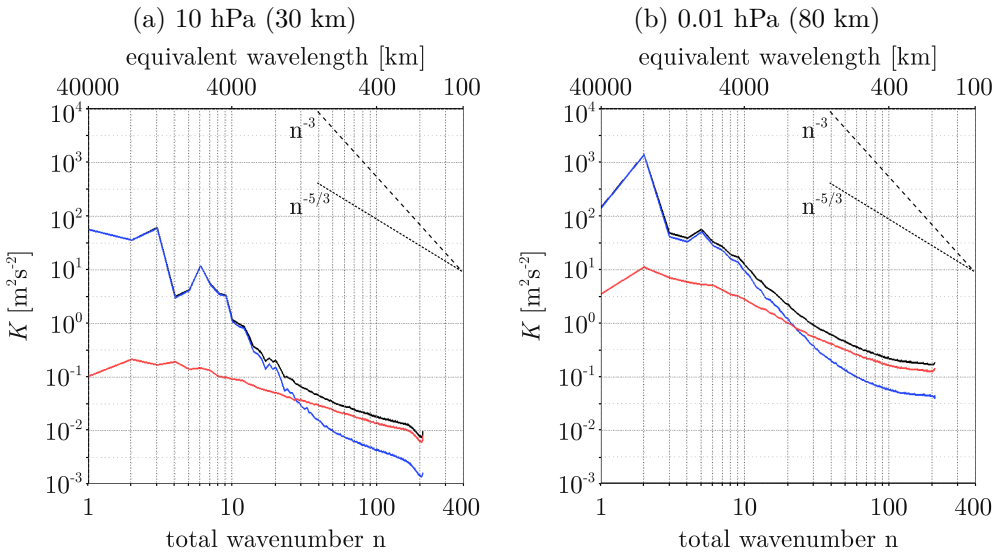

Fig. 34: Kinetic energy spectra from the T210L190 run, averaged over 16 model days, (a) middle stratospheric level at 10 hPa (30 km), (b) mesospheric level at 0.01 hPa (80 km), total KE in black, rotational component in blue, divergent component in red.

upper troposphere does not hold in the stratosphere, because no kinetic energy is generated by baroclinic Rossby waves. Instead, the whole KE spectrum is controlled by wave-mean flow interaction due to vertically propagating waves.

From Fig. 33 it becomes clear that the relative maximum of K_{ln} is shifted from $n \approx 3$ to 10 in the troposphere to $n \approx 2$ in the middle and upper stratosphere. This reflects the increasing importance of quasi-stationary planetary Rossby waves in the stratosphere. Since the winter hemispheric zonal wind in the stratosphere acts as a filter for Rossby waves according to the Charney-Drazin criterion, such a change of the KE spectrum with height is expected for the planetary scales (Charney and Drazin 1961; Andrews et al. 1987).

It also can be seen from Fig. 33, that the kinetic energy in the mesoscales is strongly decreasing with height in the lower stratosphere while it slowly increases again in the middle and upper stratosphere. From our point of view this is caused by strong damping of low-frequency mesoscale GWs in the UTLS. In the middle and upper stratosphere scale-selective damping occurs with respect to the vertical wavenumber. As a result, inertio-GWs, which typically have large horizontal

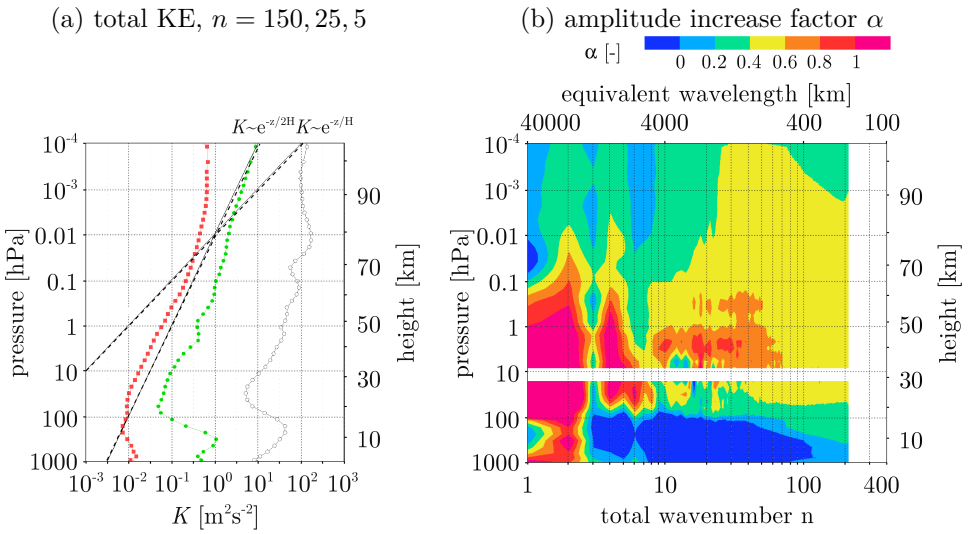

Fig. 35: (a) Vertical profile of the horizontal spectral KE for total wavenumbers $n = 5$ (gray), $n = 25$ (green) and $n = 150$ (red) and (b) vertical cross section of α in $K_{ln} \propto e^{\alpha \cdot z/H}$ from KMCM T210L190 averaged over 11 model days. In the stratosphere the curves in (a) follow more or less $e^{\alpha \cdot z/H}$, with $\alpha = 0.5$ and a scale height $H \approx 8$ km. This equivalent to the yellow color in (b).

scales compared to mid-frequency GWs are damped in the UTLS. Therefore the larger horizontal wavenumbers contain relatively more kinetic energy.

In Fig. 35a vertical profiles of the total horizontal KE for total wavenumbers $n = 5$, $n = 25$ and $n = 150$ are shown. The result for the latter one is similar to the one earlier derived by Watanabe et al. (2008) on the basis of the MIROC 3.2 middle atmosphere GCM: In the stratosphere the spectral KE increases with height according to $K_{ln} \propto e^{\alpha \cdot z/H}$ with $\alpha \approx 0.5$ and the scale height $H \approx 8$ km. The value of α depends on height and wavenumber, as can be seen in Fig. 35b, where the yellow color indicates values for α between 0.4 and 0.6. From the analysis of rocket soundings in the stratosphere, e.g., Fig. 10 in Eckermann et al. (1995), similar values for α can be derived at least for the site located at mid latitude (Primrose Lake).

The amplitude increase is substantially less than, at a first guess, the exponential decrease of density $\rho(z)$ might suggest ($\alpha = 1, K(z) \propto \rho_0/\rho(z)$ with a lower level reference density ρ_0). However, in the stratosphere, the background wind and the Brunt-Väisäla frequency N vary only slowly in the vertical at most times. The application of this approximation (the Liouville-Green or WKB ap-

proximation, Gill (1982); Nappo (2002)) to the equations of motion of GWs in the x-z-plane leads to a dependency of the GW zonal wind amplitude $\tilde{U}(z)$ on the background wind $\overline{u}(z)$ in the form

$$\tilde{U}(z) \propto \frac{1}{\sqrt{c_x(z) - \overline{u}(z)}} \cdot \sqrt{\frac{\rho_0}{\rho(z)}} \tag{40}$$

with the GW phase speed $c_x(z)$. Accordingly, the GW horizontal KE is dependent on $\overline{u}(z)$ as well with

$$K \propto \frac{1}{[c_x(z) - \overline{u}(z)]} \cdot \frac{\rho_0}{\rho(z)} \,. \tag{41}$$

Remember, in the x-z-plane the vertical wavenumber of mid-frequency GWs is represented by $|k_z(z)| = N(z)/|c_x(z) - \overline{u}(z)|$ (Fritts and Alexander 2003). This implies that GWs with phase speeds considerably larger than the background wind at a certain height assume small vertical wavenumbers and according to (41) the amplitude of their horizontal KE is smaller than expected from density decrease. Vice versa GWs with phase speeds close to but larger than the background wind assume large vertical wavenumbers and their horizontal KE could be very large. At some point, the vertical wavelength becomes too small to apply the WKB approximation, e.g., in the vicinity of critical layers, but in our model's stratosphere, the former conditions generally prevail. Hence, compared to the density decrease, a considerably smaller amplitude growth of the horizontal KE of GWs as illustrated by the red curve in Fig. 35a can be expected. In contrast to Watanabe et al. (2008) this comes just from considering the WKB approximation for GWs, no dissipative process is needed.

4.2.2 Mesosphere

In the mesosphere the evolution of the K_{ln} spectra are similar to the upper stratosphere: the spectrum is flattening with increasing height, small-scale kinetic energy is growing while KE of the planetary scales do no longer notably increase with height, compare Figs.34a and 34b. In addition the transition from a rotational to a divergent regime occurs at even larger scales ($n_T \approx 15$ at 80 km). The rotational and the divergent parts are within one order of magnitude throughout all wavenumbers. This is in contrast to stratosphere and troposphere, where

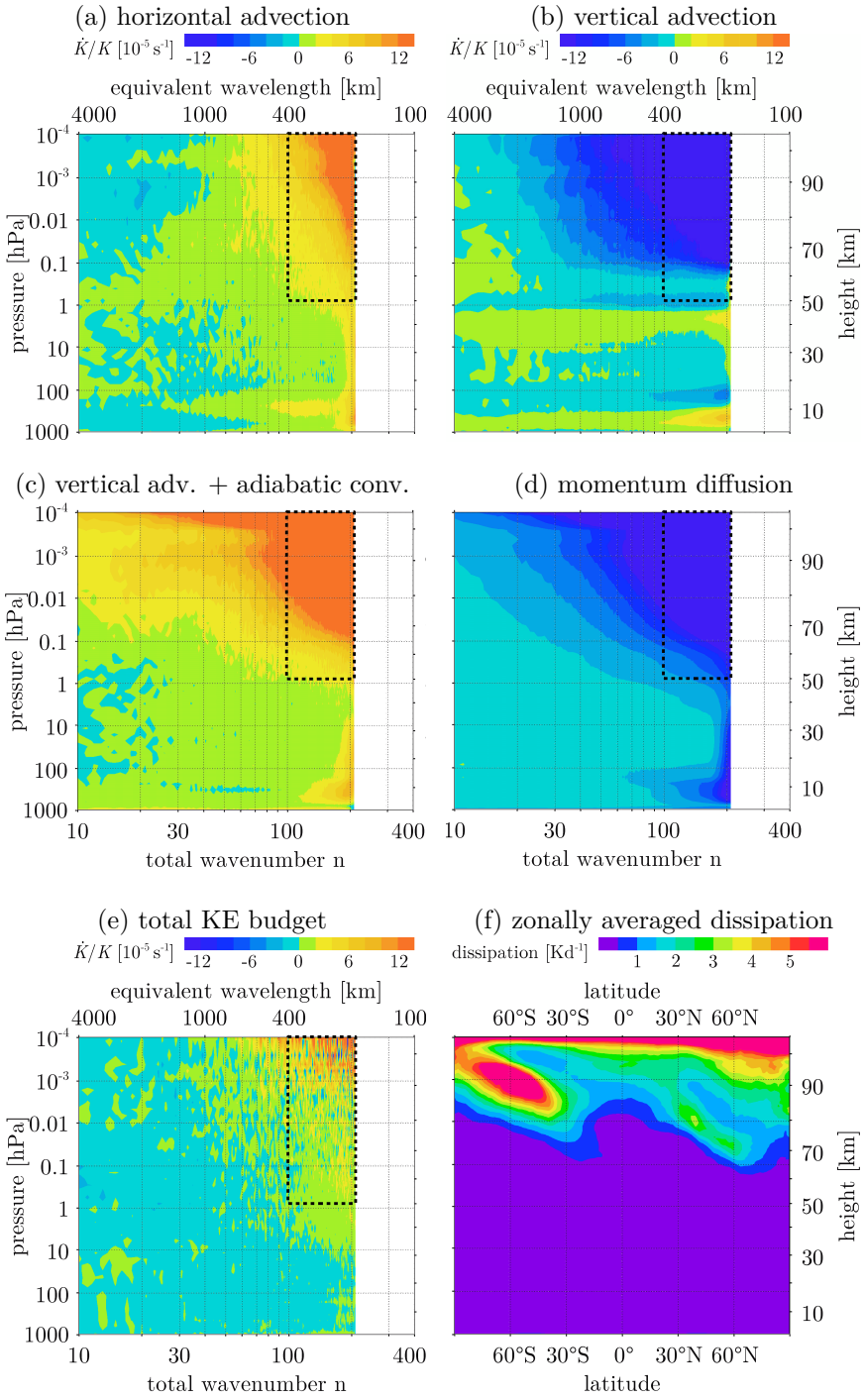

Fig. 36: From KMCM T210L190, averaged over 16 days: (a) horizontal advection, (b) vertical advection, (c) sum of vertical advection and adiabatic conversion, and (d) momentum diffusion contributions to (e) the total kinetic energy budget $\dot{K}_{ln}/K_{ln}$. The latitude-height section in (f) shows the zonally averaged total dissipation for reference. Panels (a) to (d) have the same color scale. The dotted rectangle refers to the mesospheric mesoscales.

the ratio $K_{ln}^{\xi}/K_{ln}^{\delta}$ may exceed 100 in the planetary and synoptic regime. These findings correspond well to the results of Koshyk and Hamilton (2001) for the stratosphere and lower mesosphere as simulated with the SKYHI model, see their Figs. 11 and 12.

The horizontal kinetic energy budget, already applied to analyze the TLS, helps to illuminate the breaking of GWs in the upper mesosphere as well, particularly the conversion of GW kinetic energy into mean flow kinetic energy and mean flow enthalpy. For this reason we use the GW kinetic energy equation in its stationary form (C.17) from Appendix C:

$$\underbrace{-\overline{\mathbf{v}'w'}\cdot\partial_z\overline{\mathbf{v}}-\frac{1}{\rho}\partial_z\overline{p'w'}+\frac{g}{\Theta}\overline{w'\Theta'}}_{\text{vertical advection and adiabatic conversion}} \quad = \quad \underbrace{-\overline{\mathbf{v}'\cdot\mathbf{R}'}}_{\text{momentum diffusion}}. \tag{42}$$

We derived this equation with the single-column approximation and assuming a climatological mean state for K_{ln}. We now want to check, whether these assumptions hold in the mesosphere. In Fig. 36 the necessary contributions to the spectral kinetic energy budget are shown up to the lower thermosphere for the KMCM T210L190 run, including 16 model days with 1024 snapshots. The averaged total budget $\dot{K}_{ln}/K_{ln}$ in Fig. 36e is reasonably close to zero below 0.001 hPa ($\approx$ 90 km), we therefore successfully describe a climatological mean state. In the mesosphere and for wavenumbers $n > 100$, indicated by the dotted rectangle, the contribution from horizontal advection in Fig. 36a is considerably weaker than the contributions from the two balancing terms in (42), i.e., momentum diffusion and the sum of vertical advection and adiabatic conversion, see Figs.36d and 36c. Hence, when assessing mean GW energetics in the KMCM, the single-column approach is justified since the gain of GW kinetic energy by adiabatic conversion plus vertical advection is balanced by momentum diffusion.

Coming back to (C.16) from Appendix C, the mean GW kinetic energy budget can also be described in terms of shear production, pressure work, buoyancy production and momentum diffusion:

$$0 = \underbrace{-\overline{\mathbf{v}'w'} \cdot \partial_z \overline{\mathbf{v}}}_{\text{shear production}} \underbrace{- \frac{1}{\rho} \partial_z \overline{p'w'}}_{\text{pressure work}} + \underbrace{\frac{g}{\Theta} \overline{\Theta' w'}}_{\text{buoyancy production}} + \underbrace{\overline{\mathbf{v}' \cdot \mathbf{R}'}}_{\text{momentum diffusion}} \tag{43}$$

$$\underbrace{\qquad\qquad\qquad\qquad}_{\text{energy deposition} > 0} \qquad < 0 \qquad < 0$$

These processes play a major role in our view of the interaction between GWs and the mean flow in the mesosphere which will be qualitatively interpreted in the following.

In the mean mesospheric GW kinetic energy budget (43), the momentum diffusion is always negative, as is the buoyancy production ($\overline{\Theta' w'} < 0$). The sum of shear production (or vertical advection) and adiabatic conversion (pressure work plus buoyancy production) must be positive in the mesosphere according to GW theory and corresponding GW parameterizations (Becker 2004; Shaw and Becker 2011). This is confirmed by our analysis of the spectral KE budget for the mesoscales based on the T210L190 version of the KMCM with realistic GW effects in the mesosphere (Becker 2011), as is seen in Fig. 36c. Hence, the energy deposition due to resolved GWs in the mesosphere is positive.

How do GWs contribute to the enthalpy of the mean flow? For this question we use the mean enthalpy equation (C.8) from Appendix C, which can be written in a simplified form as:

$$\dot{h} = A - \frac{g}{\Theta_r} \overline{\Theta' w'} + K_z \overline{(\partial_z \mathbf{v}')^2} \tag{44}$$

with all contributions from (C.8), which are not shown here, summarized in A. Here, the GW energy deposition from (43) can be directly inserted due to the identity $-\overline{\mathbf{v}' \cdot \mathbf{R}'} = K_z \overline{(\partial_z \mathbf{v}')^2} = \epsilon_{GW}$, which gives together with the single-column balance equation for the GW kinetic energy (C.18):

$$-\overline{\mathbf{v}'w'} \cdot \partial_z \overline{\mathbf{v}} - \frac{1}{\rho} \partial_z \overline{p'w'} = -\frac{g}{\Theta} \overline{\Theta' w'} + K_z \overline{(\partial_z \mathbf{v}')^2}\,, \tag{45}$$

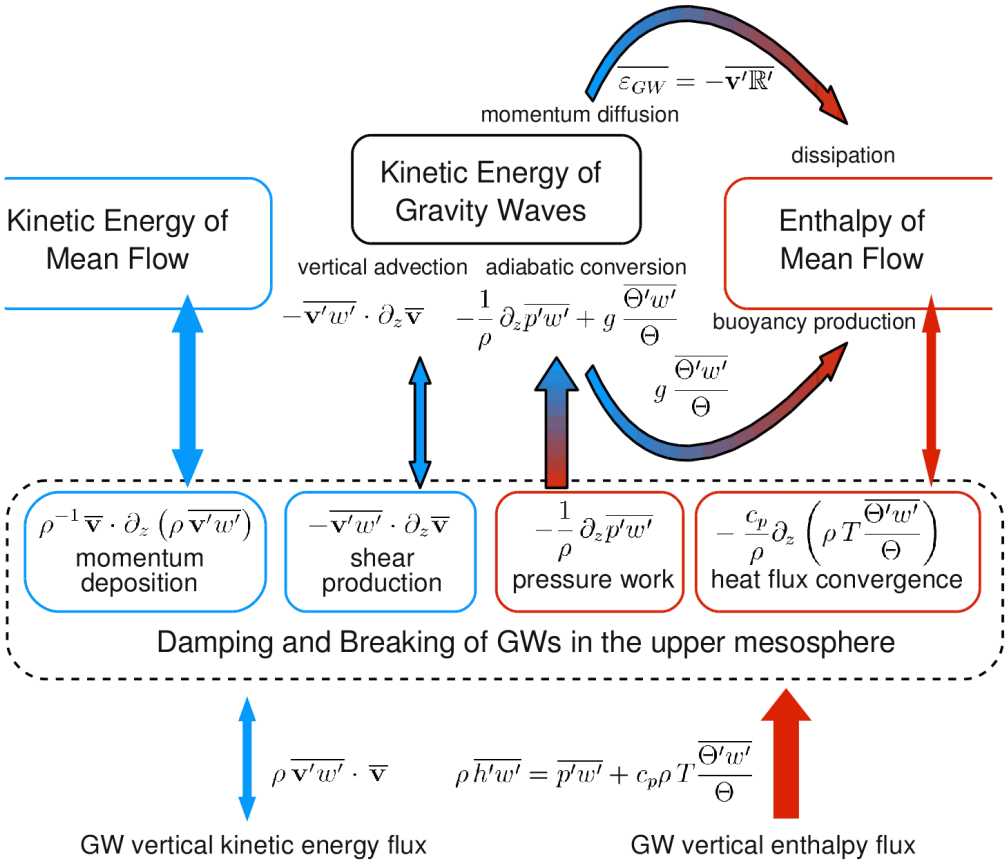

Fig. 37: Schematic picture of the energetics of GW breaking in the upper mesosphere extending the single-column approximation to the whole globally averaged mesosphere ("global column"), GW variables are primed, otherwise the variables represent the mean flow. See text for details.

and finally for the mean enthalpy equation:

$$\dot{h} = A - \overline{\mathbf{v}'w'}\cdot\partial_z\overline{\mathbf{v}} - \frac{1}{\rho}\partial_z\overline{p'w'}\,. \tag{46}$$

Thus the GW energy deposition contributes to the overall heating of the large-scale flow in the mesosphere in climate models with conventional resolution and parameterized GWs (Becker 2004, 2011).

The GW energetics in the upper mesosphere is illustrated in Fig. 37. During propagation from their generation region in the troposphere to the mesosphere, GWs are generally associated with a vertical flux of kinetic energy, which can be both upward and downward, depending on the background wind $\overline{\mathbf{v}}$. The GW vertical enthalpy flux, however, is only directed upward because $\overline{p'w'}$ is always

positive and $\overline{\Theta' w'}$ vanishes in conservative propagation. In the upper mesosphere the GWs are breaking and the GW vertical KE flux interacts with the KE of the mean flow via momentum deposition, see left-hand side of Fig. 37. Also, a shear production term arises. In our analysis this term is equivalent to the vertical advection and mostly negative in the upper mesosphere, see Fig. 36b. It should be noted that via these terms the GW KE may also act on the mean flow KE. The GW vertical enthalpy flux feeds via the pressure work term into the KE of the GWs. As mentioned above, $\overline{\Theta' w'}$ equals zero during propagation but is different from zero in the event of GW damping or breaking. Thus the heat flux convergence term on the right-hand side of Fig. 37 is also different from zero and feeds in or from the enthalpy of the mean flow. Together with the buoyancy production term, which transfers KE of GWs to the enthalpy of the mean flow, the pressure work forms the adiabatic conversion term of our analysis. At the same time, KE of GWs is also dissipated into heat, which is equivalent to the momentum diffusion in our analysis.

From the central part of Fig. 37 and from (42) it becomes clear, that in terms of the GW KE spectral budget the momentum diffusion is balanced by vertical advection and adiabatic conversion, provided that horizontal advection is negligible. Also, according to (43), (45) and (46), the energy deposition of GWs into the mean flow enthalpy equals the sum of momentum diffusion and buoyancy production, which in turn is balanced by vertical advection and the pressure work term.

To summarize Fig. 37: GWs generated in the troposphere may propagate upward to the upper mesosphere. The main energy transfer realized by these GWs is due to their associated vertical pressure flux, which is equal to the GW vertical enthalpy flux during conservative propagation without damping and breaking. In the upper mesosphere the GWs ultimately break down, but our analysis reveals, that their associated vertical pressure flux is not directly transferred to the mean flow enthalpy, but rather converted into KE of GWs in a first step and then dissipated in a second step (ϵ_{GW}). This is in contrast to standard parameterization schemes, where the energy deposition due to the pressure flux is directly written into the mean enthalpy equation.

This consideration shows that in fact the dissipative heating is associated with GWs in the upper mesosphere, because it is their KE that is mainly dissipated.

The absence of GWs would represent a serious gap in describing the large-scale sensible heat budget just because of their direct thermal effects.

Our interpretation relies on the applicability of the single-column approximation and steady-state conditions for GWs. Since our analysis considers a climatologically mean state and global wavenumber spectra, these assumptions are virtually extended over the whole globe, forming one temporally mean "global" column.

5 Conclusion

We used a mechanistic GCM (simplistic parameterizations of radiative and latent heating for permanent January conditions) to study the spectral horizontal kinetic energy budget per unit mass from the troposphere up to the mesopause region. We focused on the middle and upper troposphere as the region where most of the kinetic energy is generated by baroclinic waves and most of the mesoscale waves are excited by the forward cascades of enstrophy and energy. Additional emphasis has been put on the upper mesosphere where the global circulation is heavily influenced by mesoscale waves. The mesoscales are explicitly modeled in a consistent way at all levels, taking advantage of an advanced turbulent diffusion scheme and dispensing with a parameterization of GWs. Computer constraints imposed the use of two different model setups facilitating these two main objects.

Tropospheric macroturbulence requires a high spatial resolution and was studied with a T330 spectral truncation and 100 vertical levels up to 1 hPa, resulting in a vertical spacing of 250 m from above the boundary layer up to 100 hPa (15 km). To simulate the impact of mesoscale waves generated in the troposphere on the circulation in the mesosphere a somewhat coarser horizontal resolution is sufficient but a high vertical resolution up to the lower thermosphere is required. We used a T210 spectral truncation with 190 vertical levels, resulting in a vertical level spacing of 600 m up to 0.0001 hPa (105 km).

Analysis of the spectral horizontal kinetic energy budget revealed three different spectral regimes in the context of tropospheric macroturbulence: 1) a shallow slope in the planetary scales, where we found an upscale 2D kinetic energy flux, 2) a steep -3 slope in the synoptic scales which is the expression of a strong downscale 2D enstrophy flux, and 3) a shallow -5/3 slope in the mesoscales of the upper troposphere and lower stratosphere. In this regime any upscale quasi-2D energy cascade can be ruled out as an explanation. Instead, the mesoscale -5/3 slope is controlled by a forward horizontal energy cascade accompanied by strong buoyancy forces.

The transition from the enstrophy cascading to this non-2D energy cascading regime is marked by the equipartition of the horizontal kinetic energy in its rotational (almost constant -3 slope) and divergent (almost constant -5/3 slope) components, where in the mesoscales and from the upper troposphere on the latter even dominates. At the same time the enstrophy cascade is replaced by

the non-2D energy cascade within the mesoscales. This finding is consistent with the possible development of stratified turbulence in the upper troposphere.

Stratified turbulence requires a strongly stratified background and non-linear inertial forces and buoyancy forces have to be of the same order of magnitude. In terms of our GCM simulation these requirements are bound to a sufficient spatial resolution along with a small horizontal Froude number regime and equivalent contributions of horizontal advection and of adiabatic conversion to the horizontal kinetic energy flux.

We found that in the upper troposphere these contributions are indeed of the same order of magnitude for the mesoscales in a narrow vertical layer between 250 and 200 hPa (10.3 to 11.8 km). The T330L100 run ($\Delta z \approx 250$ m) covers this layer with seven model levels, the T330L30 run with barely one level ($\Delta z \approx 1300$ m). At other levels in the middle and upper troposphere the contributions do not fulfill this criterion in any of our simulations. In our model the development of stratified turbulence requires a high horizontal resolution (T330) which has to be complemented with a high vertical resolution (L100) as well.

Apart from the spatial resolution we would like to address an important aspect by which our GCM substantially differs from box model simulations or tank experiments with stratified turbulence. In the GCM, the kinetic energy injection at baroclinic scales leads to a dynamically consistent energy forcing far outside the wavenumber range where stratified turbulence may develop. Moreover, the maximum of this forcing is located somewhat lower in altitude and, hence, vertically separated from the upper tropospheric region of stratified turbulence. It is this spectral and vertical separation that sets the stage for the development of stratified turbulence in the model's upper troposphere as a result of an upward vertical pressure flux convergence and a weakened enstrophy cascade at this height. In contrast, the kinetic energy injection in tank experiments and box model simulations occurs right at the large-scale side of the stratified turbulence range and in the very same vertical domain.

How large is the impact of GWs on the tropospheric kinetic energy budget? In our GCM we can easily detect gravity wave events in grid-space. Most of these waves have phase speeds different from zero and are generated in the middle and upper troposphere in connection with large-scale planetary waves and a subsequent development of cyclones and anti-cyclones, which underlines the cru-

cial importance of frontal activity and geostrophic adjustment for the radiation of GWs in our model. As already pointed out, we found the vertical pressure flux to be important for the development of stratified turbulence in the upper troposphere. It is worth noting, that in the global mean and on climatological time scales, the vertical pressure flux corresponds to upward propagating GWs generated in the middle troposphere and deposing their energy in the upper troposphere. However, this horizontally and temporarily averaged picture does not enable us to deduce the reason for the behavior of the horizontal kinetic energy budget in any single case, especially not on a local scale. We may state that on this scale quasi-linear GWs can not be neglected, but it would be purely speculative to assign an active role in the spectral energetic of stratified turbulence in the TLS to them.

The stratosphere does not contain a major wavenumber focused kinetic energy source like the troposphere. The concept of macroturbulence cannot be applied here. Compared to the troposphere the maximum in the kinetic energy spectrum is shifted to the planetary waves (Rossby waves). The horizontal kinetic energy budget is largely dependent on the interaction of the vertically propagating waves with the background conditions. The increase of the mesoscale kinetic energy with height is roughly half as large as it could be expected due to decreasing density, which is the result of the background wind influencing the vertical wave propagation in the stratosphere.

The mesosphere is similar to the stratosphere in a way that there is no narrowband kinetic energy input. We found, however, that it differs from the stratosphere, and at the same time resembles some characteristics of the troposphere, because of the contributions to the horizontal kinetic energy budget. In our view the main reason for this behavior is the breaking of upward propagating tropospheric GWs and their influence on the large scale circulation in the mesosphere.

Our analysis of the horizontal kinetic energy budget illuminates this interaction. The upward propagating GWs transfer energy from the level of their generation, that means the troposphere, to the mesosphere. To the largest extent this is realized by the GW upward vertical pressure flux, which in turn gives rise to an increase of the kinetic energy of the GWs in the mesosphere. In the model this GW kinetic energy is deposed into the enthalpy of the mean flow via buoyancy production and momentum diffusion, which is equivalent to the GW

kinetic energy dissipation. Without the resolved GWs, e.g. in simple GW parameterizations, there is no occurrence of this "frictional heating", which is in fact observed in the real mesosphere.

Moreover it turns out that in the climatological mean the contribution of horizontal advection to the horizontal kinetic energy budget is negligible for large parts of the mesosphere. That means that the mesoscale momentum diffusion balances the positive adiabatic conversion plus vertical advection on these scales. This is similar to the description of mid-frequency GWs in single-column approximation. In other words, the climatological mean mesospheric GW kinetic energy budget can be described in one global single-column.

It should be noted that chronologically we first investigated the GW kinetic energy budget in the mesosphere, where the mesoscales are obviously dominated by quasi-linear GWs. It was only thereafter that we noticed similarities in the kinetic energy budget of the mesosphere to that of the upper troposphere and lower stratosphere. This encouraged us to apply this analysis also to these atmospheric layers, where the mesoscales are likely not dominated by quasi-linear GWs. In this way the successful mesospheric analysis of the horizontal spectral kinetic energy contributed substantially to a better understanding of the tropospheric horizontal kinetic energy cascades.

Acknowledgments

I wish to thank all people who supported me during the research leading to this thesis. I am indebted to Erich Becker, who not only guided me through the work and the writing as my supervisor but always lent me a helping hand even at times when his other two were busiest. I want to express special thanks to Axel Gabriel and Fabian Senf for their support during the writing of this thesis and the numerous discussions and inspirations on atmospheric physics and beyond. I am thanking Christoph Zülicke and Brigitte Wecke for the guidance and data retrieval in context with ECMWF's MARS system. Last but not least I would like to thank Erik Lindborg for the short but very fruitful discussion which brought the concept of stratified turbulence into my view.
The work has been partly founded by the *Deutsche Forschungsgemeinschaft* under grant BE 3208/2-1 (SAGES) and by the Leibniz Graduate School ILWAO.

A The additional horizontal diffusion scheme

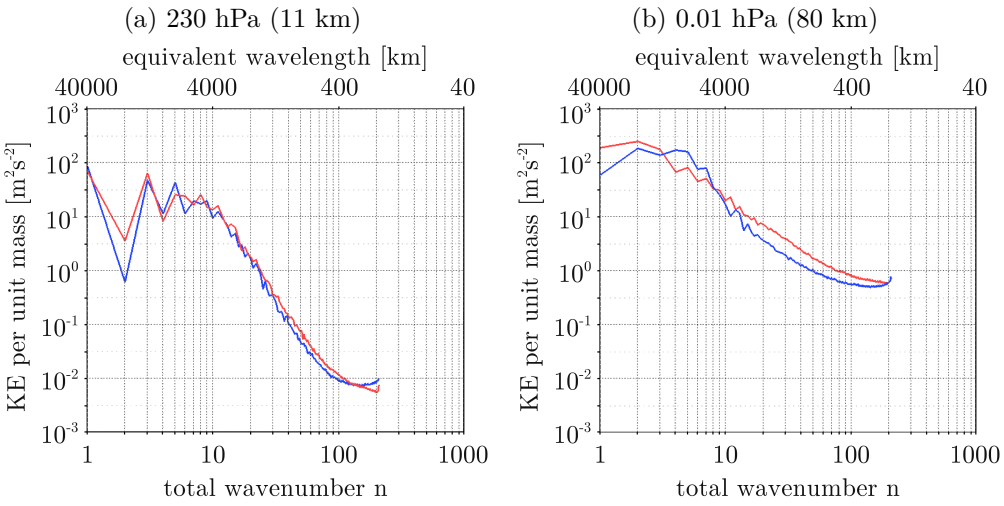

Fig. A.1: Horizontal kinetic energy spectra of the T210L190 run with two diffusion schemes: standard Smagorinsky-type in blue, Smagorinsky-type with additional diffusion in red; (a) for the tropospheric level 230 hPa (11 km), (b) for the mesospheric level 0.01 hPa (80 km).

In the present version of KMCM we apply an additional hyperdiffusion along with the standard Smagorinsky diffusion scheme. This mitigates the inability of the latter to simulate a realistic kinetic energy spectrum in the tropospheric mesoscales ("spectral blocking"). This is illustrated in Fig. A.1, where the blue curves show the kinetic energy spectra with only the Smagorinsky scheme applied, which leads to a bending up of the spectrum or "spectral blocking" in the mesoscales, while the red curves show the spectra with the additional diffusion in place, where this behavior is eliminated for most of the mesoscales apart from the very largest wavenumbers. In the following the additional diffusion shall be described in more detail.

In the conventional Smagorinsky scheme the tendency of the horizontal wind due to momentum diffusion $\mathbf{H}$ can be written as (Becker and Burkhardt 2007):

$$\mathbf{H} = \rho^{-1} \nabla \left(\rho K_h \mathbf{S}_h \right) \tag{A.1}$$

with the density ρ, the horizontal turbulent diffusion coefficient K_h and the strain tensor $\mathbf{S}_h$. In the vertical hybrid coordinate system as used in the KMCM, ρ is

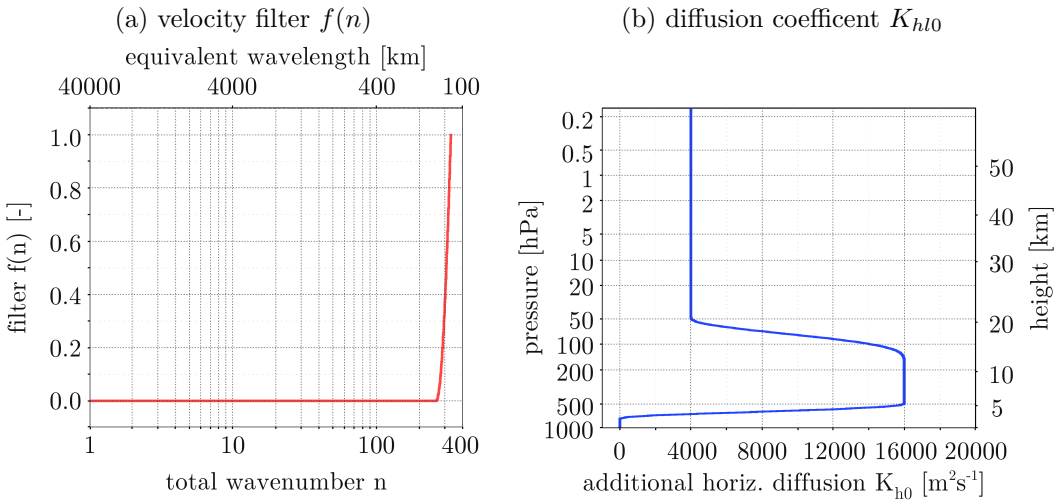

Fig. A.2: Coefficients for the additional spectrally filtered horizontal momentum diffusion of the T210L190 run: (a) $f(n)$ acts on the largest horizontal wavenumbers independently of the model level, (b) K_{hl0} is constant for all wavenumbers and most prominent in upper troposphere and lower stratosphere.

replaced by the pressure increment between two half levels Δp_l and $\mathbf{H}$ can be calculated on each level l:

$$\mathbf{H}_l = \Delta p_l^{-1} \nabla \left(\Delta p_l K_{hl} \mathbf{S}_{hl} \right) \tag{A.2}$$

with the following relations:

$$\begin{aligned}
K_{hl} &= l_{hl}^2 \sqrt{|\mathbf{S}_{hl}^2| + \mathbf{S}_{0l}^2} \left[1 + \alpha F\left(Ri\right) \right] , \\
\mathbf{S}_{hl} &= \left[(\nabla + \mathbf{e}_z / a_e) \circ \mathbf{v}_l \right] + \left[(\nabla + \mathbf{e}_z / a_e) \circ \mathbf{v}_l \right]^T - \nabla \cdot \mathbf{v}_l \left(\mathbf{e}_x \circ \mathbf{e}_x + \mathbf{e}_y \circ \mathbf{e}_y \right) , \\
\mathbf{v}_l &= \sum_{n=1}^{N} \frac{a_e^2}{n(n+1)} \sum_{m=-n}^{n} \left[\xi_{lnm} \left(\mathbf{e}_z \times \nabla Y_{nm} \right) + \delta_{lnm} \nabla Y_{nm} \right] .
\end{aligned} \tag{A.3}$$

Here, l_{hl} is the mixing length, $F(Ri)$ is a function of the Richardson number and α a scaling factor, $\mathbf{S}_{0l}$ corresponds to a minimum horizontal wind shear (Becker 2009). The horizontal velocity in grid-space on each model level $\mathbf{v}_l$ is computed from the spectral amplitudes of vorticity and divergence.

The total horizontal diffusion is defined as:

$$\mathbf{H}_l = \Delta p_l^{-1} \nabla \left(\Delta p_l K_{hl} \mathbf{S}_{hl} \right) + \Delta p_l^{-1} \nabla \left(\Delta p_l K_{h0l} \mathbf{S}_{hfl} \right) \tag{A.4}$$

with

$$\begin{aligned} K_{h0l} &= const \quad \text{for all } n \text{ at a given vertical level,} \\ \mathbf{S}_{hfl} &= \left[(\nabla + \mathbf{e}_z / a_e) \circ \mathbf{v}_{fl} \right] + \left[(\nabla + \mathbf{e}_z / a_e) \circ \mathbf{v}_{fl} \right]^T - \nabla \cdot \mathbf{v}_{fl} \left(\mathbf{e}_x \circ \mathbf{e}_x + \mathbf{e}_y \circ \mathbf{e}_y \right) , \\ \mathbf{v}_{fl} &= \sum_{n=1}^{N} f(n) \frac{a_e^2}{n(n+1)} \sum_{m=-n}^{n} \left[\xi_{lnm} \left(\mathbf{e}_z \times \nabla Y_{nm} \right) + \delta_{lnm} \nabla Y_{nm} \right] . \end{aligned} \tag{A.5}$$

The spectral filter $f(n)$ is shown in Fig. A.2a. For the T330 run it starts to deviate from zero at $n = 270$ and increases to unity at $n = 330$. The additional horizontal diffusion coefficient K_{h0} can be seen in Fig. A.2b.

Due to the stress tensor formulation of the conventional Smagorinsky term in (A.3) and the additional diffusion term in (A.5) both automatically fulfill the angular momentum conservation law.

B Spherical harmonics and computation of the equivalent wavelength

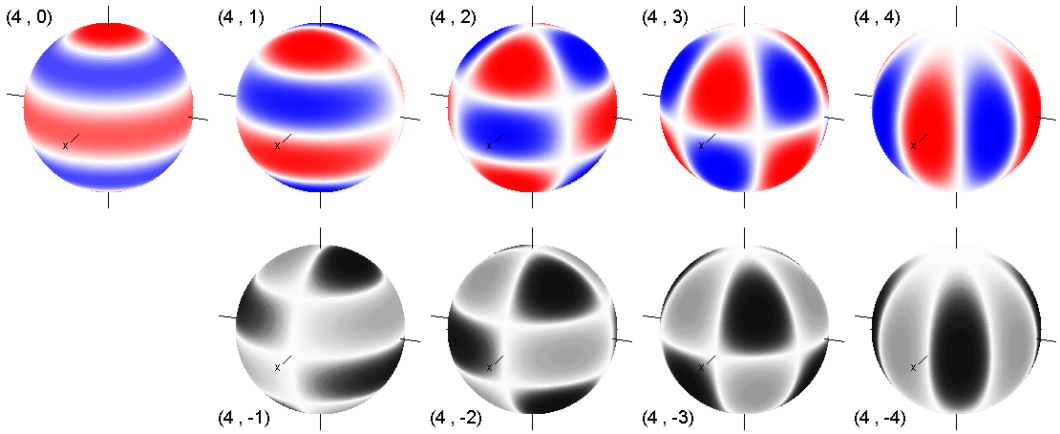

Fig. B.1: Visualization of spherical harmonics Y_{nm} of degree $n = 4$ and order m with $0 \leq m \leq 4$ in the upper half and $-4 \leq m \leq -1$ in the lower half (after *http://www.bpreid.com/poas.php*).

The projection on spherical harmonics Y_{nm} is a straightforward technique, see Washington and Parkinson (2005). Nevertheless, this appendix shall shortly present a short visual approach toward this transformation.

In our spectra, any quantity X_n comprises $2n+1$ coefficients of the form X_{nm} with $-n \leq m \leq n$. The global form of all Y_{nm} for $n = 4$ is shown in Fig. B.1.

In the context of planetary scale circulation patterns or large-scale weather systems this visualization helps to access how the coefficients for the particular zonal wavenumbers m contribute to the total wavenumber n. Even a zonal wavenumber $m = 0$ (leftmost panel in Fig. B.1), contributes to $n = 4$, since it represents a pattern typical for the large-scale tropospheric flow: weak in the tropics and polar regions, strong in the mid-latitudes.

For comparison with grid-point models such as SKYHI we need to compute a wavelength equivalent to the total spectral truncation wavenumber N on any great circle of Earth's surface (a_e = Earth's radius):

$$\lambda_{trunc} = \frac{4\pi a_e}{N} \,. \tag{B.1}$$

The motivation for (B.1) arises from the three spherical harmonics Y_{nm} with $m = 0$, $m = n$, and $m = -n$ as seen in Fig. B.1 on the far left-hand side with λ being a meridional wavelength and far right-hand side with λ being an equatorial wavelength, respectively. Assuming an optimal case, only two grid cells are needed in a grid-point model to resolve a given sinusoidal wave. A spectral truncation T210 therefore compares to a grid-point distance of about 95 km and T330 to 60 km. The equivalent wavelength of any particular total wavenumber $0 < n \leq N$ is computed accordingly as:

$$\lambda = \frac{4\pi a_e}{n} \,. \tag{B.2}$$

For an extended discussion of wave representation in grid-point models see Haltiner and Williams (1980), Lander and Hoskins (1997) or Davies and Brown (2001).

C Single-column GW kinetic energy equation and mean horizontal momentum and enthalpy equations in the anelastic approximation

The GW kinetic energy budget plays a major role in our interpretation in Chapter 4. Hereby the energy deposition into the enthalpy of the mean flow is of particular importance. In the following we therefore want to describe the mean flow enthalpy equation in anelastic approximation following Becker (2011). We also want to simplify the kinetic energy budget by applying the single-column approximation for GWs (negligible horizontal derivatives of mean quantities) and the climatological mean (negligible tendency of the total budget).

According to Becker (2011), his Eq. (4), the enthalpy equation in anelastic approximation in the z-system can be written as following:

$$\dot{h} = \frac{\dot{p}}{\rho_r} + \frac{g\left(\rho - \rho_r\right) w}{\rho_r} + Q_{ext} + \frac{c_p}{\rho_r}\partial_z\left(\rho_r \frac{T}{\Theta} K_z \partial_z \Theta\right) + K_z\left(\partial_z \mathbf{v}^2\right) , \tag{C.1}$$

with the enthalpy h, the external heating Q_{ext}, the specific heat capacity c_p, temperature T, and potential temperature Θ. We assume that turbulence is only represented by vertical diffusion and expanded the overall diabatic heating term Q in Eq. (4) of Becker (2004) into the three terms on the right-hand side of (C.1).

The hydrostatic approximation and the continuity equation are in their usual form:

$$0 = \partial_z p + g\rho\,, \tag{C.2}$$

$$0 = \nabla \cdot \mathbf{v} + \frac{1}{\rho_r}\partial_z\left(\rho_r w\right) . \tag{C.3}$$

We would like to prepare (C.1) in such a way that the GW energy deposition to the mean enthalpy becomes clear. Therefore we introduce the mean and GW

terms, i.e., $X = \overline{X} + X'$ to (C.1), multiply by ρ_r, implement the continuity equation (C.3) and average over the GW scales:

$$\begin{aligned}
&\partial_t\left(\rho_r\overline{h}\right) + \nabla\cdot\left(\rho_r\overline{h\mathbf{v}}\right) + \nabla\cdot\left(\rho_r\overline{h'\mathbf{v}'}\right) + \partial_z\left(\rho_r\overline{hw}\right) + \partial_z\left(\rho_r\overline{h'w'}\right) \\
&= \partial_t\overline{p} + \mathbf{v}\cdot\nabla\overline{p} + \overline{\mathbf{v}'\cdot\nabla p'} + \overline{w}\partial_z\overline{pw'}\partial_z\overline{p'} + g\left(\overline{\rho}-\rho_r\right)w + g\overline{\rho'w'} + \rho_r\overline{Q}_{ext} \\
&+ c_p\partial_z\left(\rho_r\frac{T_r}{\Theta_r}K_z\partial_z\Theta\right) + \rho_r K_z\left(\partial_z\overline{\mathbf{v}}\right)^2 + \rho_r K_z\overline{\left(\partial_z\mathbf{v}'\right)^2}\,.
\end{aligned} \tag{C.4}$$

The single-column approximation leads to:

$$\nabla\cdot\left(\rho_r\overline{h'\mathbf{v}'}\right) = 0\,, \tag{C.5}$$

and together with the assumption that vertical wavelengths do not exceed the scale height ($\nabla\cdot\mathbf{v}' + \partial_z w' = 0$) to:

$$\overline{\mathbf{v}'\cdot\nabla p'} + \overline{w'\partial_z p'} = \partial_z\overline{p'w'}\,. \tag{C.6}$$

With (C.5) and (C.6) inserted in (C.4), multiplying with ρ_r^{-1} and omitting the overlines for mean-flow terms we get:

$$\begin{aligned}
\dot{h} = &\frac{\dot{p}}{\rho_r} - \frac{1}{\rho_r}\partial_z\left(\rho_r\overline{h'w'}\right) + \frac{1}{\rho_r}\partial_z\overline{p'w'} + \frac{g\left(\rho-\rho_r\right)w}{\rho_r} + \frac{g}{\rho_r}\overline{\rho'w'} + Q_{ext} \\
&+ \frac{c_p}{\rho_r}\partial_z\left(\rho_r\frac{T_r}{\Theta_r}K_z\partial_z\Theta\right) + K_z\left(\partial_z\mathbf{v}\right)^2 + K_z\overline{\left(\partial_z\mathbf{v}'\right)^2}\,.
\end{aligned} \tag{C.7}$$

Here we substitute $h' = p'/\rho_r + c_p\Theta' T/\Theta_r$, and with the Boussinesq approximation for GWs also $\rho'/\rho_r = -\Theta'/\Theta_r$:

$$\begin{aligned}
\dot{h} = &\frac{\dot{p}}{\rho_r} + \frac{c_p}{\rho_r}\partial_z\left[\rho_r\frac{T_r}{\Theta_r}\left(K_z\partial_z\Theta - \overline{\Theta'w'}\right)\right] + \frac{g\left(\rho-\rho_r\right)w}{\rho_r} + Q_{ext} \\
&+ K_z\left(\partial_z\mathbf{v}\right)^2 - \frac{g}{\Theta_r}\overline{\Theta'w'} + K_z\overline{\left(\partial_z\mathbf{v}'\right)^2}\,.
\end{aligned} \tag{C.8}$$

This representation of the mean enthalpy equation allows for direct comparison with the energy deposition by GWs from the mean GW kinetic energy equation, which is described next.

For the deduction of the GW horizontal kinetic energy equation we start with the linear wave equation for horizontal momentum:

$$d_t \mathbf{v}' = \partial_t \mathbf{v}' + \overline{\mathbf{v}} \cdot \nabla \mathbf{v}' = -w' \partial_z \overline{\mathbf{v}} - \frac{\nabla p'}{\rho_r} + \frac{1}{\rho_r} \partial_z \left(\rho_r \partial_z \mathbf{v}' \right) \tag{C.9}$$

with the mean horizontal velocity $\overline{\mathbf{v}} = (\overline{u}, \overline{v}, 0)$, the reference density ρ_r, and the waves horizontal velocity $\mathbf{v}' = (u', v', 0)$, vertical velocity w', and pressure p'. As above we again omit the overline in mean-flow terms and replace $\overline{\mathbf{v}}$ with $\mathbf{v}$. To get the mean GW kinetic energy we multiply (C.9) with $\mathbf{v}'$, average in time and space and introduce $\mathbf{R}'$ for the momentum diffusion, substituting the last term on the right-hand side of (C.9):

$$\overline{\mathbf{v}' \cdot d_t \mathbf{v}'} = \overline{\mathbf{v}' \cdot \partial_t \mathbf{v}'} + \overline{\mathbf{v}' \cdot (\mathbf{v} \cdot \nabla) \mathbf{v}'} = -\overline{\mathbf{v}' \cdot w' \partial_z \mathbf{v}} - \overline{\mathbf{v}' \cdot \frac{\nabla p'}{\rho_r}} + \overline{\mathbf{v}' \cdot \mathbf{R}'}\,, \tag{C.10}$$

which can be re-written as:

$$d_t \frac{\overline{\mathbf{v}'^2}}{2} = -\overline{\mathbf{v}' w'} \cdot \partial_z \mathbf{v} \underbrace{- \frac{1}{\rho_r} \overline{\nabla \cdot (\mathbf{v}' p')}}_{=0} + \frac{1}{\rho_r} \overline{p' \nabla \cdot \mathbf{v}'} + \overline{\mathbf{v}' \cdot \mathbf{R}'}\,. \tag{C.11}$$

The single-column approximation leads to the neglect of the second term on the right-hand side of (C.11). Also, the total derivative d_t becomes a partial one ∂_t, i.e. $\overline{\mathbf{v}' \cdot (\mathbf{v} \cdot \nabla) \mathbf{v}'} \to 0$ in (C.10). We may rewrite the remaining pressure term in (C.11) with the continuity equation for GWs, $\nabla \cdot \mathbf{v}' + \partial_z w' = 0$:

$$\partial_t \frac{\overline{\mathbf{v}'^2}}{2} = -\overline{\mathbf{v}' w'} \cdot \partial_z \mathbf{v} + \frac{1}{\rho_r} \overline{p' (-\partial_z w')} + \overline{\mathbf{v}' \cdot \mathbf{R}'}\,, \tag{C.12}$$

which is equivalent to

$$\partial_t \frac{\overline{\mathbf{v}'^2}}{2} = -\overline{\mathbf{v}' w'} \cdot \partial_z \mathbf{v} - \frac{1}{\rho_r} \overline{\partial_z (p' w')} + \frac{1}{\rho_r} \overline{w' \partial_z p'} + \overline{\mathbf{v}' \cdot \mathbf{R}'}\,. \tag{C.13}$$

Our model is a hydrostatic model, that is for GWs: $\partial_z p' = -g \rho'$. Equation (C.13) then becomes:

$$\partial_t \frac{\overline{\mathbf{v}'^2}}{2} = -\overline{\mathbf{v}' w'} \cdot \partial_z \mathbf{v} - \frac{1}{\rho_r} \partial_z \overline{p' w'} - \frac{g}{\rho_r} \overline{\rho' w'} + \overline{\mathbf{v}' \cdot \mathbf{R}'}\,. \tag{C.14}$$

With the Boussinesq approximation for GWs ($\rho'/\rho_r = -\Theta'/\Theta_r$) we can replace density ρ with potential temperature Θ on the right-hand side of (C.14):

$$\partial_t \frac{\overline{\mathbf{v}'^2}}{2} = -\overline{\mathbf{v}'w'} \cdot \partial_z \mathbf{v} - \frac{1}{\rho}\partial_z \overline{p'w'} + \frac{g}{\Theta_r}\overline{\Theta' w'} + \overline{\mathbf{v}' \cdot \mathbf{R}'}\,. \tag{C.15}$$

At last the GW kinetic energy is assumed to be stationary over the climatological scale ($\partial_t(\overline{\mathbf{v}'^2}/2) \approx 0$) and we get:

$$\underbrace{0 = \underbrace{-\overline{\mathbf{v}'w'} \cdot \partial_z \mathbf{v}}_{\text{vertical advection}} \underbrace{- \frac{1}{\rho}\partial_z \overline{p'w'}}_{\text{pressure work}} + \underbrace{\frac{g}{\Theta_r}\overline{\Theta' w'}}_{\text{buoyancy production}}}_{\text{energy deposition}} + \underbrace{\overline{\mathbf{v}' \cdot \mathbf{R}'}}_{\text{momentum diffusion}}\,. \tag{C.16}$$

$$\underbrace{\underbrace{-\overline{\mathbf{v}'w'} \cdot \partial_z \mathbf{v} - \frac{1}{\rho}\partial_z \overline{p'w'} + \frac{g}{\Theta_r}\overline{\Theta' w'}}_{\text{vertical advection and adiabatic conversion}} \quad = \quad \underbrace{-\overline{\mathbf{v}' \cdot \mathbf{R}'}}_{\text{momentum diffusion}}}_{\text{adiabatic conversion}}\,, \tag{C.17}$$

and

$$\underbrace{-\overline{\mathbf{v}'w'} \cdot \partial_z \mathbf{v} - \frac{1}{\rho}\partial_z \overline{p'w'}}_{\text{energy deposition}} = -\frac{g}{\Theta_r}\overline{\Theta' w'} - \overline{\mathbf{v}' \cdot \mathbf{R}'}\,. \tag{C.18}$$

The GW energy deposition from (C.18) can now be used to replace the last two terms on the right-hand side of the mean enthalpy equation (C.8) due to the identity $-\overline{\mathbf{v}' \cdot \mathbf{R}'} = K_z \overline{(\partial_z \mathbf{v}')^2} = \epsilon_{GW}$. This is in particular discussed for the GW energy deposition in the mesosphere in Section 4.2.2. We also rely on (C.16) to (C.18) in our interpretation of tropospheric and mesospheric spectra in Chapter 4.

D Calculation of associated Legendre functions and their derivatives in KMCM

The associated Legendre functions $P_m^n(sin\,\varphi)$ and their derivatives are calculated recursively. This technique is well known, however, for high orders the recursive calculation presents a numerical problem due to the occurrence of sub-accuracy numbers. This appendix describes the solution to this problem as used in the KMCM.

Standard calculation

In low resolution versions of KMCM the associated Legendre functions are recursively computed (Bronshtein et al. 2007) as following:

$$P_m^n = \frac{sin\,\phi \cdot (2n-1) \cdot P_m^{n-1} - (n+m-1) \cdot P_m^{n-2}}{n-m}\,. \tag{D.1}$$

The derivative with respect to $sin\,\phi$ is computed as:

$$PA_m^n(sin\,\varphi) = sin\,\phi \cdot n \cdot P_m^n - (n+m) \cdot P_m^{n-1}\,. \tag{D.2}$$

Normalization takes place such that

$$\int_{-1}^{1} (P_{mNorm}^n)^2 dz = \int_{-1}^{1} (PA_{mNorm}^n)^2 dz = \frac{1}{2}\,. \tag{D.3}$$

This can be realized by using a normalization factor F_{mNorm}^n

$$P_{mNorm}^n = P_m^n \cdot F_{mNorm}^n\,, \tag{D.4}$$

with

$$F_{mNorm}^n = \sqrt{\frac{1}{4}(2n+1) \cdot \frac{(n-m)!}{(n+m)!}}\,. \tag{D.5}$$

The calculation works fine with our model up to total wavenumbers of $n \approx 85$ but runs into numerical problems for larger n. One obstacle is that the faculty term

$$\widehat{F}^n_{mFac} = \frac{(n+m)!}{(n-m)!} \tag{D.6}$$

becomes very large values (i.e. $> 10^{100}$), which will be numerically treated as positive infinity, leading to wrong normalization factors and therefore wrong associated Legendre functions and derivatives.

Implicit splitting of the normalization factor

To overcome this problem the normalization factor has to be split in two parts. Whenever during the recursive calculation loop the term F^n_{mFac} surpasses the threshold value F_{Tsh} it will be divided by F_{Tsh}. As a result F^n_{mFac} is kept in a numerically practicable bandwith. At the same time a counting factor F^n_{mCnt} will be increased by 1 enabling a backward calculation of the "real" faculty term $\widehat{F}^n_{mFac}$ at any time with

$$\widehat{F}^n_{mFac} = F^n_{mFac} \cdot {F_{Tsh}}^{F^n_{mCnt}} . \tag{D.7}$$

As an example the calculation is shown for $m = 30$ and $n = 90$ and a threshold of $F_{Tsh} = 10^{100}$:

$$\begin{aligned}
\widehat{F}^n_{mFac} &= \frac{(n+m)!}{(n-m)!} \\
&= \frac{120!}{60!} \\
&= 61 \cdot 62 \cdot \ldots \cdot 119 \cdot 120 \\
&= 8.03 \cdot 10^{116} \\
&= (8.03 \cdot 10^{16}) \cdot (10^{100})^1 \\
&= F^n_{mFac} \cdot {F_{Tsh}}^{F^n_{mCnt}} .
\end{aligned} \tag{D.8}$$

The left term on the right-hand side of (D.8) is the new F^n_{mFac} and has a numerically practicable value, the right term constitutes the counting part F^n_{mTsh}, here with an exponent F^n_{mCnt} of 1.

The normalization factor F^n_{mNorm} can now generally be expressed as

$$\begin{aligned} F^n_{mNorm} &= \sqrt{\frac{1}{4}(2n+1)\cdot\frac{1}{\widehat{F}^n_{mFac}}} \\ &= \sqrt{\frac{1}{4}(2n+1)\cdot\frac{1}{F^n_{mFac}\cdot {F_{Tsh}}^{F^n_{mCnt}}}} \\ &= \sqrt{\frac{(2n+1){F_{Tsh}}^{-F^n_{mCnt}}}{4F^n_{mFac}}} \\ &= \sqrt{\frac{(2n+1)}{4F^n_{mFac}}}\cdot {F_{Tsh}}^{-F^n_{mCnt}/2}\,. \end{aligned} \tag{D.9}$$

By introducing F^n_m with

$$F^n_m = \sqrt{\frac{(2n+1)}{4F^n_{mFac}}}\,, \tag{D.10}$$

equation (D.9) simplifies to

$$F^n_{mNorm} = F^n_m\cdot {F_{Tsh}}^{-F^n_{mCnt}/2}\,. \tag{D.11}$$

With the terms on the right-hand side of (D.11) readily in place for each (n,m) this implicit technique allows to compute the normalization of P^n_m and $PA^n_m(sin\,\varphi)$ for total wavenumbers larger than $n = 85$. However, for $n > 150$ the simple recursive formulation in (D.1) again encounters numerical problems as described in the next section.

Calculation of associated Legendre functions with UCAR routines

While the numerical problem related to the normalization has been solved as described above, the recursive formulation (D.1) for the calculation of P^n_m runs itself into numerical problems for $n > 150$.

We therefore implemented the recursive procedures `dalfk` and `dlftp`, both provided by the University Corporation for Atmospheric Research (UCAR) in their Fortran packages `alfpack` via *ftp.ucar.edu/dsl/lib/alfpack*, see Adams and Swarztrauber (1997) for details. These packages do not show the numerical prob-

lems of the simple approach in (D.1). Therefore, the KMCM utilizes the UCAR routine to calculate the associated Legendre functions but still relies on (D.2) for the derivatives. That includes the split normalization factor (D.11).

In the following the propagation of the split normalization factors throughout the calculation of the derivatives of the associated Legendre functions will be described. The result has been implemented in the KMCM module `clint`.

As already mentioned, the associated Legendre functions P_m^n are available via the UCAR routines from `alfpack` and are normalized using (D.3). The normalization factor F_m^n as well as F_{mCnt}^n are calculated in subroutine `facrout` of `clint`. The threshold value is set to $F_{Tsh} = 10^{100}$. To apply (D.2) one has to deduce the normalization as in (D.4):

$$P_m^n = P_{mNorm}^n \cdot \frac{1}{F_{mNorm}^n}\,, \tag{D.12}$$

The not yet normalized derivative is calculated using (D.2):

$$PA_m^n = sin\,\phi \cdot n \cdot P_m^n - (n+m) \cdot P_m^{n-1}\,, \tag{D.13}$$

and its normalization is according to (D.12):

$$PA_{mNorm}^n = PA_{mNorm}^n \cdot F_{mNorm}^n\,. \tag{D.14}$$

Together with (D.13) one gets

$$\begin{aligned} PA_{mNorm}^n &= \left(sin\,\phi \cdot n \cdot \frac{P_{mNorm}^n}{F_{mNorm}^n} - (n+m) \cdot \frac{{P_m^{n-1}}_{Norm}}{{F_m^{n-1}}_{Norm}} \right) \cdot F_{mNorm}^n \\ &= sin\,\phi \cdot n \cdot P_{mNorm}^n - (n+m) \cdot {P_m^{n-1}}_{Norm} \cdot \frac{F_{mNorm}^n}{{F_m^{n-1}}_{Norm}}\,. \end{aligned} \tag{D.15}$$

Applying (D.11) to the normalization factor in (D.15) one can write:

$$\begin{aligned} \frac{F_{mNorm}^n}{{F_m^{n-1}}_{Norm}} &= \frac{F_m^n \cdot {F_{Tsh}}^{-F_{mCnt}^n}}{F_m^{n-1} \cdot {F_{Tsh}}^{-{F_m^{n-1}}_{Cnt}}} \\ &= \frac{F_m^n}{F_m^{n-1}} \cdot {F_{Tsh}}^{-(F_{mCnt}^n - {F_m^{n-1}}_{Cnt})/2}\,. \end{aligned} \tag{D.16}$$

Plugging (D.16) back into (D.15) yields:

$$\begin{aligned} PA^n_{mNorm} &= nP^n{}_{mNorm} sin\,\phi - (n+m)P^{n-1}_m{}_{Norm} \frac{F^n_m}{F^{n-1}_m} F_{Tsh}{}^{-\left(F^n_{mCnt} - F^{n-1}_m{}_{Cnt}\right)/2} \\ &= F^n_m \left[n \frac{P^n_{mNorm}}{F^n_m} sin\,\phi - (n+m) \frac{P^{n-1}_m{}_{Norm}}{F^{n-1}_m} F_{Tsh}{}^{-\left(F^n_{mCnt} - F^{n-1}_m{}_{Cnt}\right)/2} \right] . \end{aligned} \tag{D.17}$$

Using

$$P^n{}_{mHelp} = P^n{}_{mNorm} \cdot \frac{1}{F^n_m} , \tag{D.18}$$

equation (D.17) further simplifies to

$$PA^n_{mNorm} = F^n_m \left[nP^n{}_{mHelp} sin\,\phi - (n+m)P^{n-1}_m{}_{Help} F_{Tsh}{}^{-\left(F^n_{mCnt} - F^{n-1}_m{}_{Cnt}\right)/2} \right] . \tag{D.19}$$

With (D.17) or (D.19) one may calculate PA^n_{mNorm} by using any reliably calculated $P^n{}_{mNorm}$ in a straightforward manner without restrictions to the maximum total wavenumber.

E Collection of horizontal spectra and vertical cross sections

In this appendix a larger collection of kinetic energy spectra and cross sections will be shown. The motivation for this collection is, first, to shortly address some findings which would have gone beyond the scope of the main part of this thesis and, second, to provide a more comprehensive representation of the analyzed data for reference.

The following set of figures consists of the spectra for KE, the KE budget, the contributions to the KE budget from horizontal advection, vertical advection, adiabatic conversion and total momentum diffusion, the 2D kinetic energy and enstrophy fluxes, and the non-2D kinetic energy fluxes due to the particular contributions to the KE budget as mentioned above. All quantities are plotted against the total horizontal wavenumber n. The flux pictures are shown for the troposphere only. In addition to the wavenumber range $1 \leq n \leq 330$ they are also presented for $10 \leq n \leq 330$ to enhance the mesoscales.

The geometric altitude presented together with the pressure of the models hybrid levels corresponds to the U.S. Standard Atmosphere 1976 as calculated with *http://www.luizmonteiro.com/StdAtm.aspx* except for the three uppermost levels in the mesosphere, which have been estimated using CIRA 86 zonal pressure-height data (Fleming et al. 1990).

The troposphere is represented by a 17 day T330L100 run at the following levels:

$$
\begin{aligned}
150 \text{ hPa} &\approx 13.6 \text{ km}, \\
206 \text{ hPa} &\approx 11.6 \text{ km}, \\
229 \text{ hPa} &\approx 10.9 \text{ km}, \\
254 \text{ hPa} &\approx 10.3 \text{ km}, \\
304 \text{ hPa} &\approx 9.1 \text{ km}, \\
350 \text{ hPa} &\approx 8.1 \text{ km}, \\
402 \text{ hPa} &\approx 7.2 \text{ km}, \\
447 \text{ hPa} &\approx 6.4 \text{ km}, \\
499 \text{ hPa} &\approx 5.6 \text{ km}, \\
608 \text{ hPa} &\approx 4.1 \text{ km}, \\
718 \text{ hPa} &\approx 2.8 \text{ km}, \\
815 \text{ hPa} &\approx 1.8 \text{ km}.
\end{aligned}
$$

Stratosphere and mesosphere are represented by a 16 day T210L190 run at the following levels, the lowermost level at 166 hPa overlaps with the uppermost level from the tropospheric part at 150 hPa:

$$\begin{aligned}
0.0001 \text{ hPa} &\approx 105 \text{ km},\\
0.0004 \text{ hPa} &\approx 97 \text{ km},\\
0.001 \text{ hPa} &\approx 90 \text{ km},\\
0.005 \text{ hPa} &\approx 84 \text{ km},\\
0.01 \text{ hPa} &\approx 80 \text{ km},\\
0.1 \text{ hPa} &\approx 66 \text{ km},\\
1 \text{ hPa} &\approx 48 \text{ km},\\
6 \text{ hPa} &\approx 35 \text{ km},\\
12 \text{ hPa} &\approx 30 \text{ km},\\
44 \text{ hPa} &\approx 21 \text{ km},\\
119 \text{ hPa} &\approx 15 \text{ km},\\
166 \text{ hPa} &\approx 13 \text{ km}.
\end{aligned}$$

In the following, let us address some features, which have not been extensively discussed in the main part.

The spectral KE in the lower troposphere at 718 hPa (2.8 km) and 815 hPa (1.9 km), Fig. E.3, exhibits a shallow mesoscale spectral regime close to -5/3. In contrast to the upper troposphere, Fig. E.2, where this behavior is due to dominant divergent modes (red curves), this is mainly caused by a deviation of the rotational modes (blue curves) from the -3 law toward a shallower regime.

The spectral KE budget shows that in the middle and upper troposphere, the contributions of horizontal advection and adiabatic conversion, which play a major role in the concept of mesoscale stratified turbulence, are in near balance in the planetary and synoptic scale, compare the blobs for $1 \leq n \leq 10$ in Figs. E.1c and E.1e and the red and blue curves for $1 \leq n \leq 30$ in Figs. E.4b-f and E.5a-d. This is consistent with the KE injection due to the breaking of baroclinic waves at this height. It this therefore not surprising that this spectral behavior strongly decreases toward the lower stratosphere, Fig. E.4a, and toward the lower troposphere, Fig. E.5e, where the KE injection is substantially smaller or even absent.

The KE spectra in the stratosphere and mesosphere, Figs. E.13 and E.14, nicely show the increasing importance of the divergent modes (red curves) with height. Also, the shape of the KE spectrum changes from the 3-regime structure in the lower stratosphere, Fig. E.13f, to a shape with rather two different spectral

slopes in the lower thermosphere, Fig. E.14a. It seems, that with the decreasing importance of the rotational modes, the steep part of the KE spectrum in the synoptic and sub-synoptic scale is more and more eroded with increasing height toward the lower thermosphere.

Last but not least the cross sections of vertical advection and adiabatic conversion in Fig. E.12 both show a change in sign from the upper stratosphere to the lower mesosphere. This is attributed to the change in sign in the vertical derivative of the averaged zonal wind $\partial_z \overline{u}$ across the stratopause at 50 hPa.

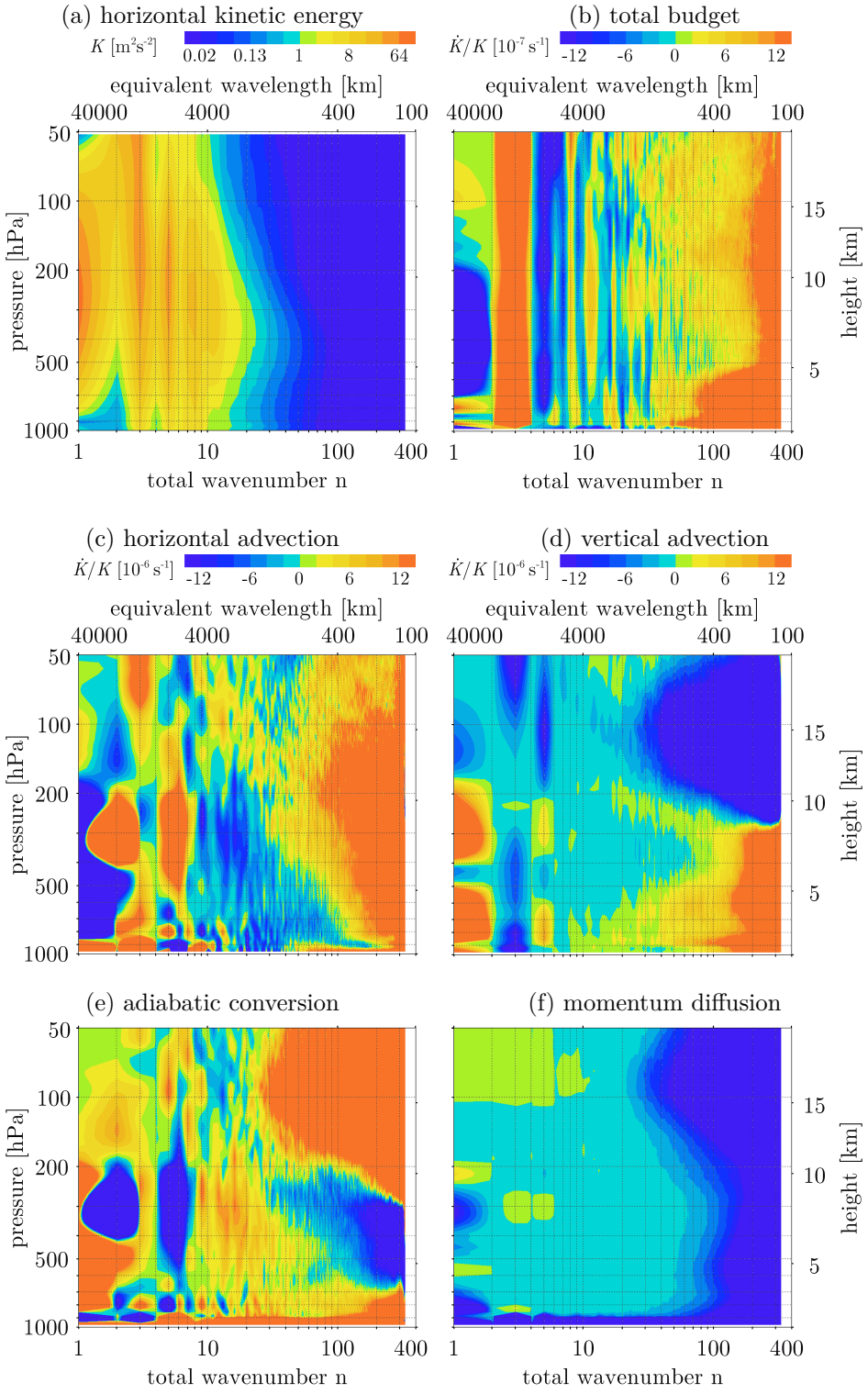

Fig. E.1: Tropospheric cross sections of (a) K_{ln}, (b) its normalized total budget $\dot{K}_{ln}/K_{ln}$, (c)-(f) contributions to $\dot{K}_{ln}/K_{ln}$ according to (22) - (24), from KMCM T330L100, averaged over 17 days. Panels (c) to (f) have the same color scale.

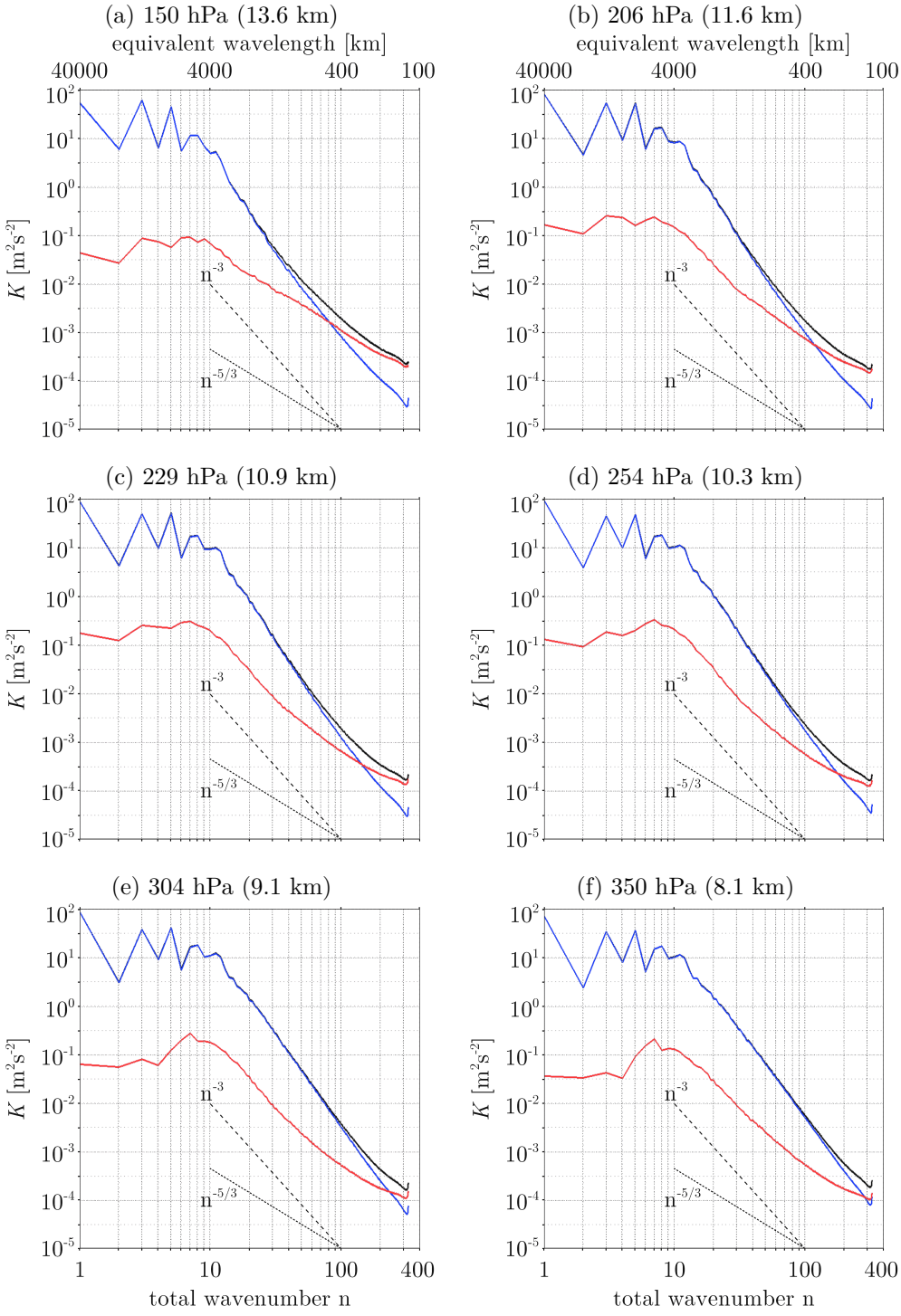

Fig. E.2: Upper tropospheric spectra of horizontal kinetic energy K_{ln} (black curve) and its rotational part (blue curve) and divergent part (red curve) between 150 hPa and 350 hPa, from KMCM T330L100, averaged over 17 days.

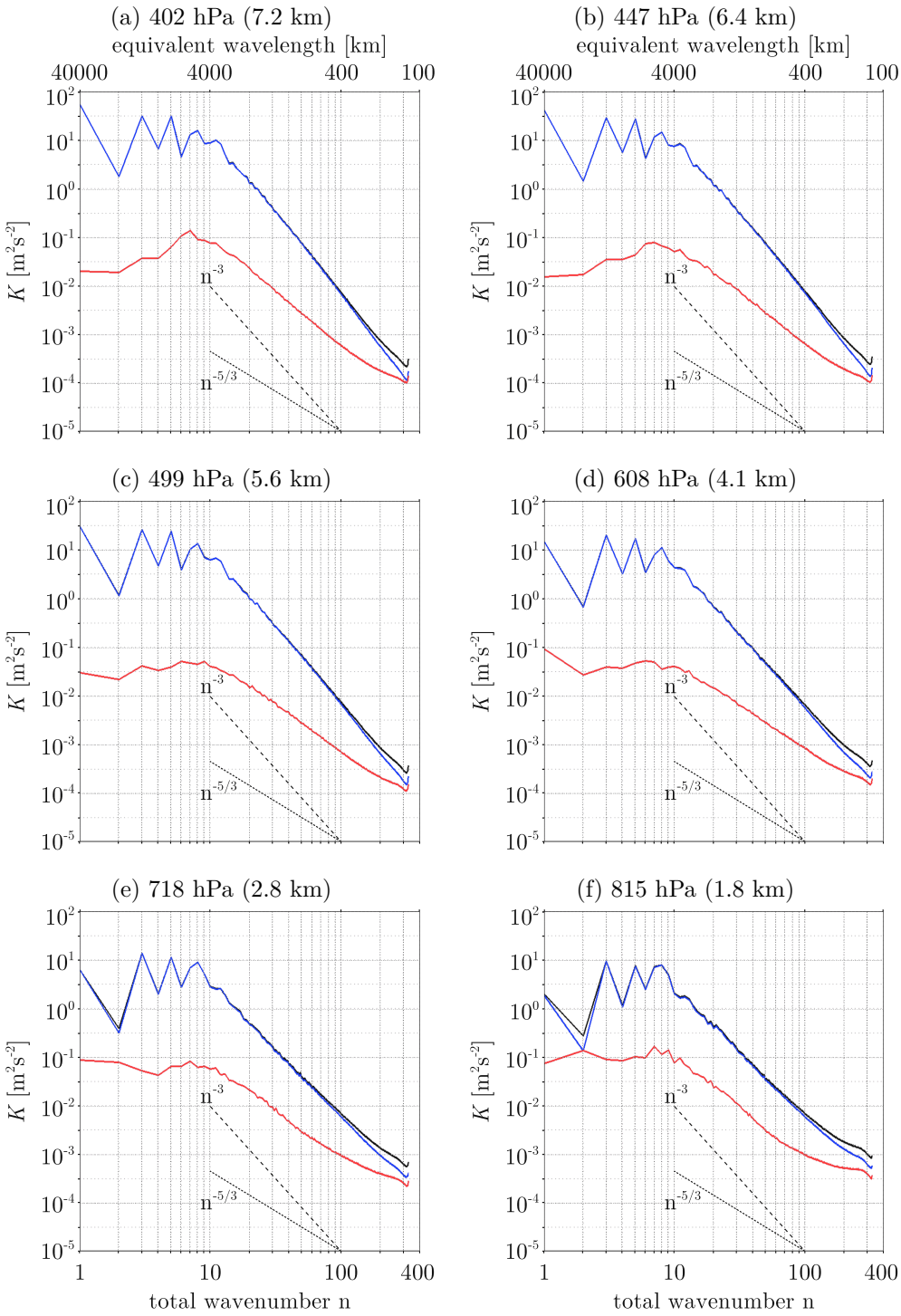

Fig. E.3: Same as Fig. E.2 but for middle and lower tropospheric levels from 402 hPa to 815 hPa.

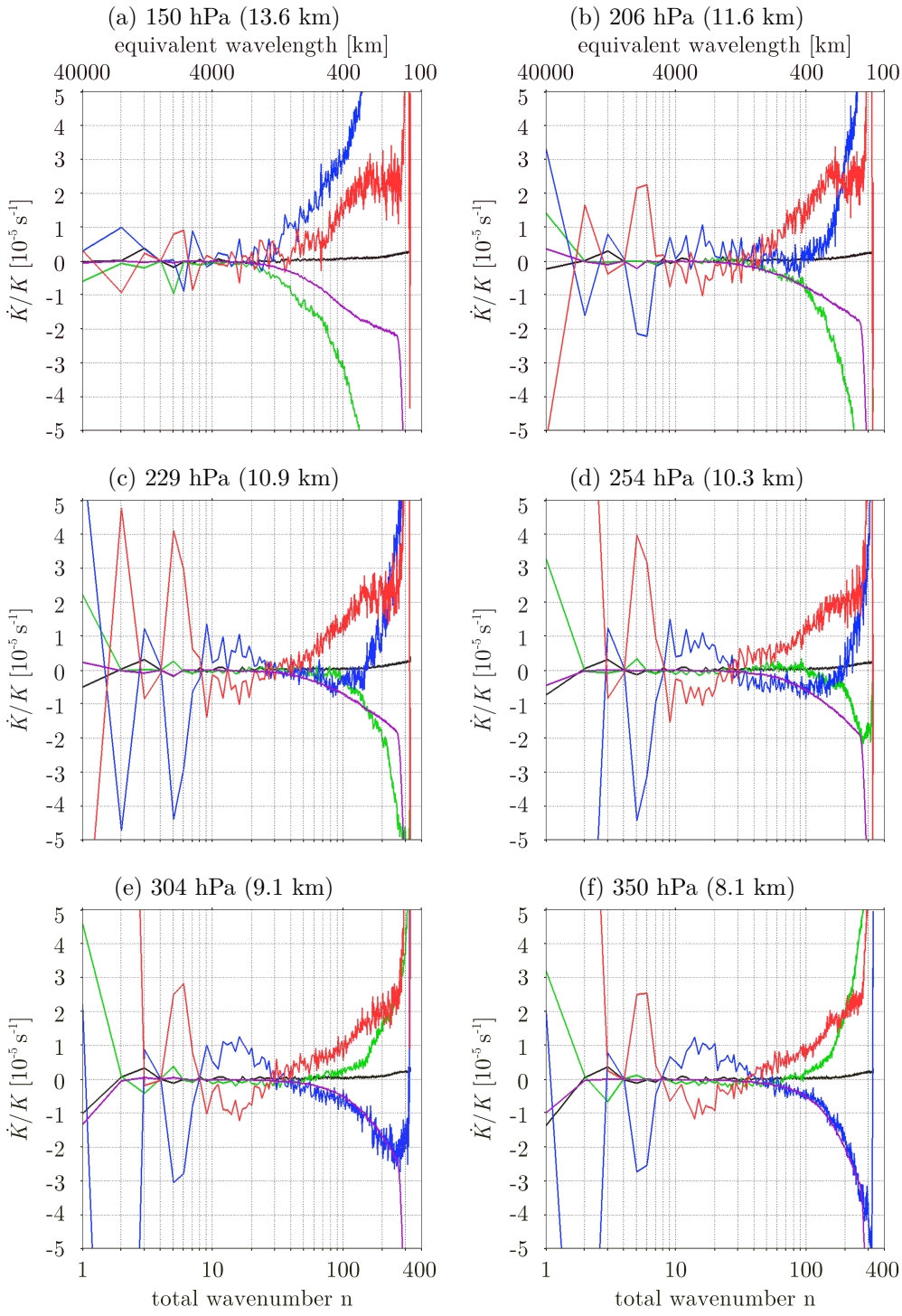

Fig. E.4: Upper tropospheric spectra of contributions to the normalized total budget of horizontal kinetic energy $\dot{K}_{ln}/K_{ln}$ (black curve) due to horizontal advection (red), vertical advection (green), adiabatic conversion (blue), and momentum diffusion (purple) between 150 hPa and 350 hPa, from KMCM T330L100, averaged over 17 days.

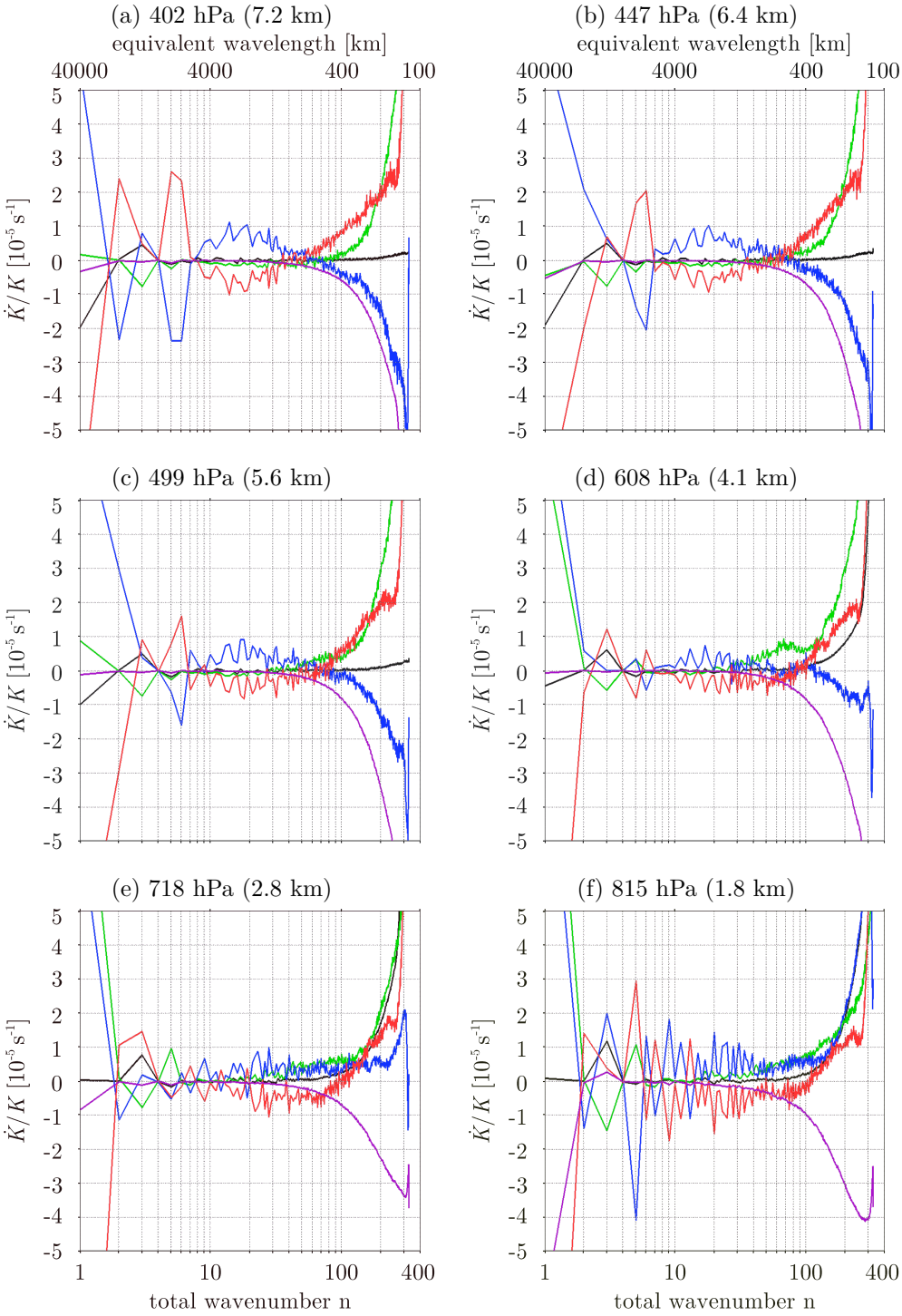

Fig. E.5: Same as Fig. E.4 but for middle and lower tropospheric levels from 402 hPa to 815 hPa.

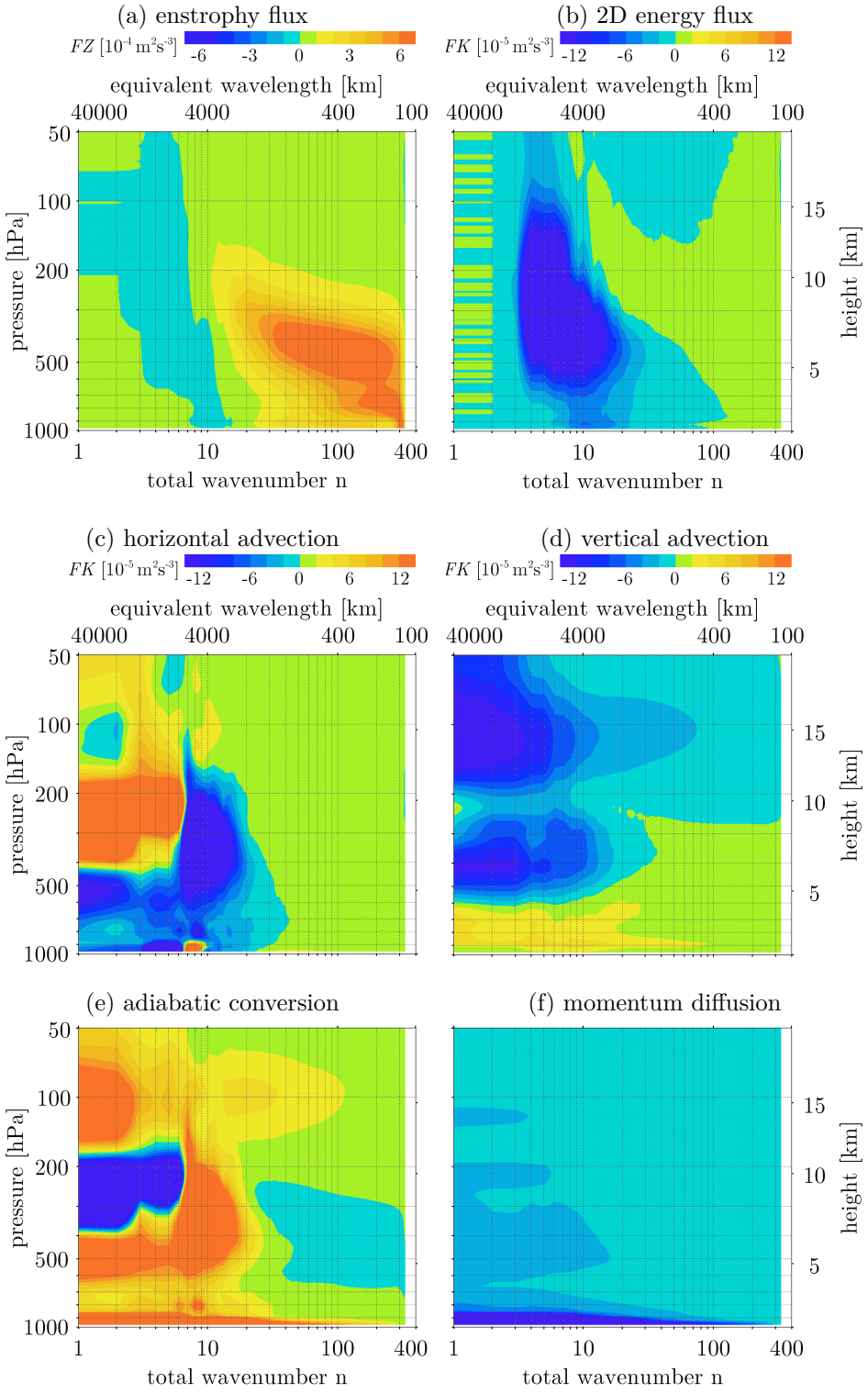

Fig. E.6: Tropospheric cross sections of (a) enstrophy flux as in (35), (b) 2D energy flux as in (34), (c)-(f) contributions (all with the same color scale) to the non-2D energy flux according to (34), from KMCM T330L100, 17 day average.

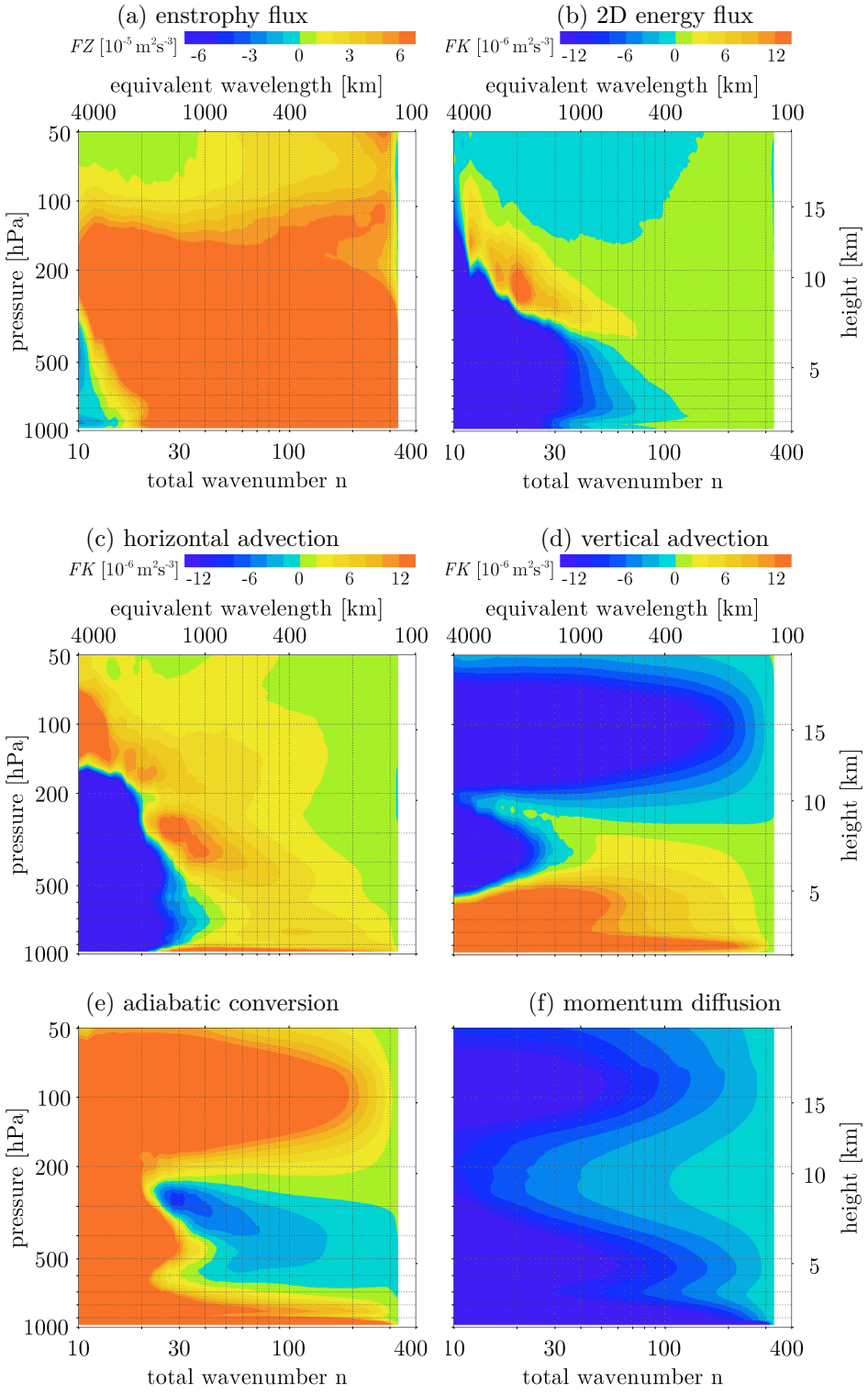

Fig. E.7: Same as Fig. E.6, but for total wavenumbers $n \geq 10$ only and with 1/10 of the scale for enhancement of the mesoscales.

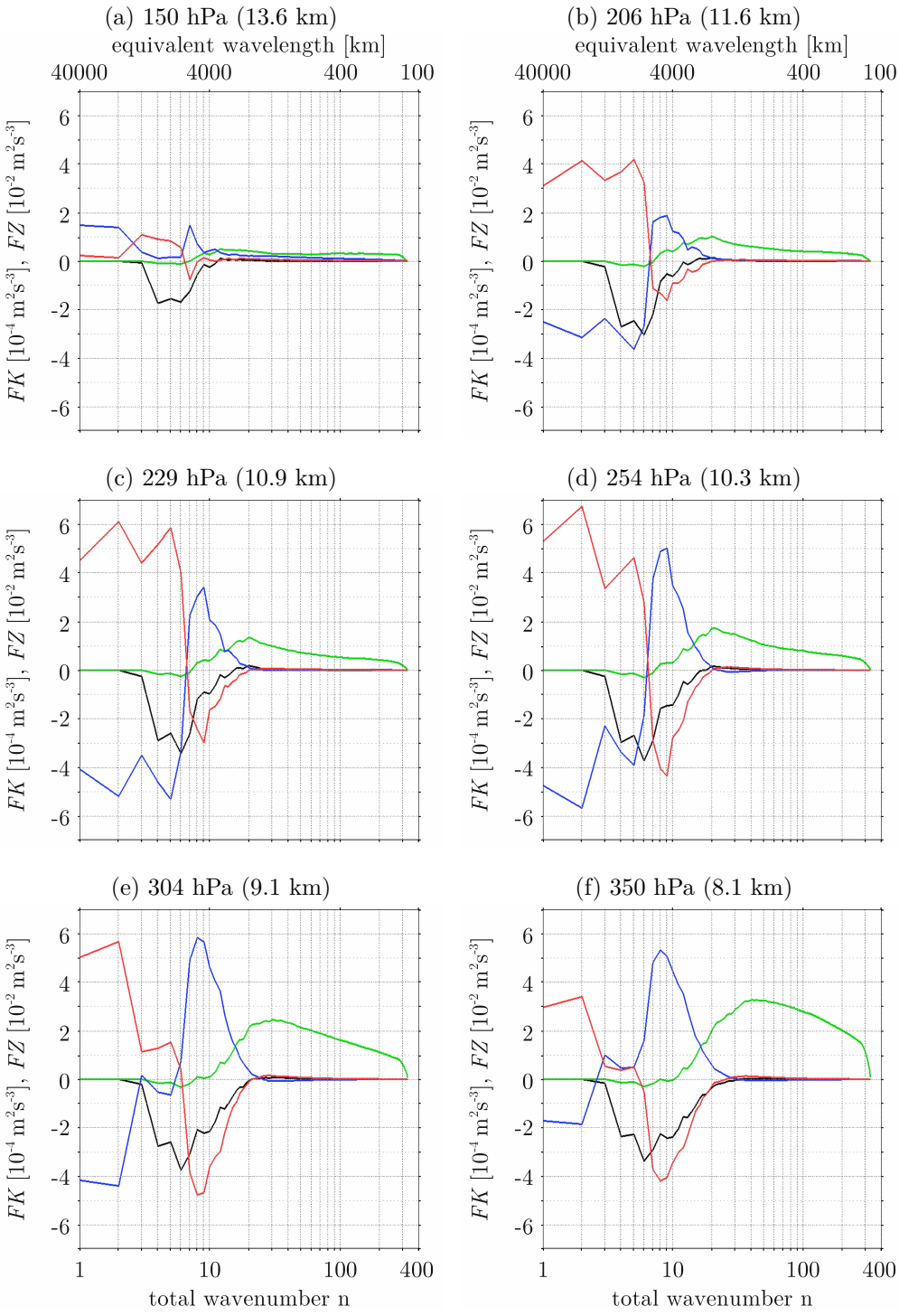

Fig. E.8: Upper tropospheric spectra of enstrophy flux (green) and 2D energy flux (black) and non-2D energy fluxes due to horizontal advection (red) and adiabatic conversion (blue) between 150 hPa and 350 hPa, from KMCM T330L100, averaged over 17 days.

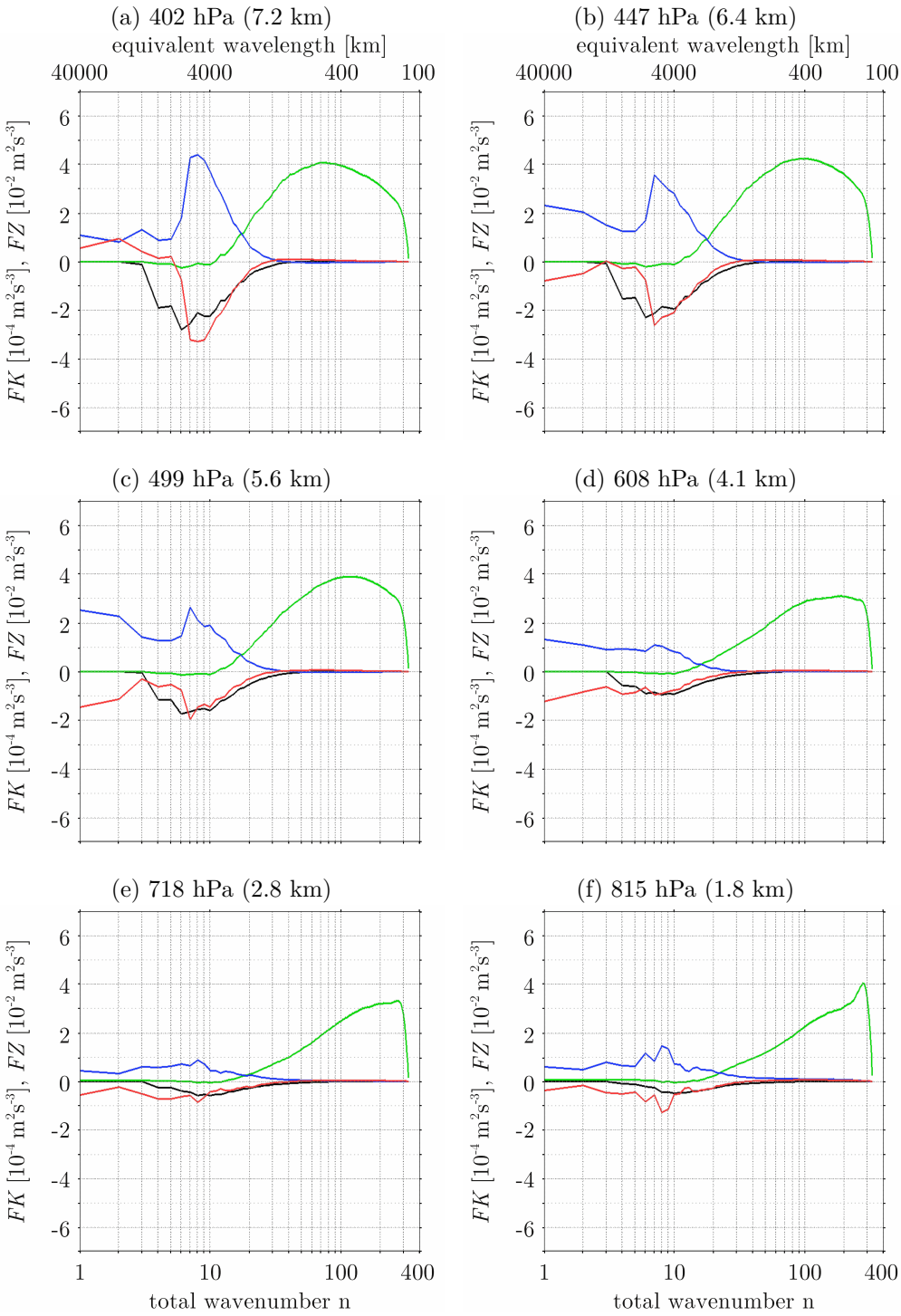

Fig. E.9: Same as Fig. E.8 but for middle and lower tropospheric levels from 402 hPa to 815 hPa.

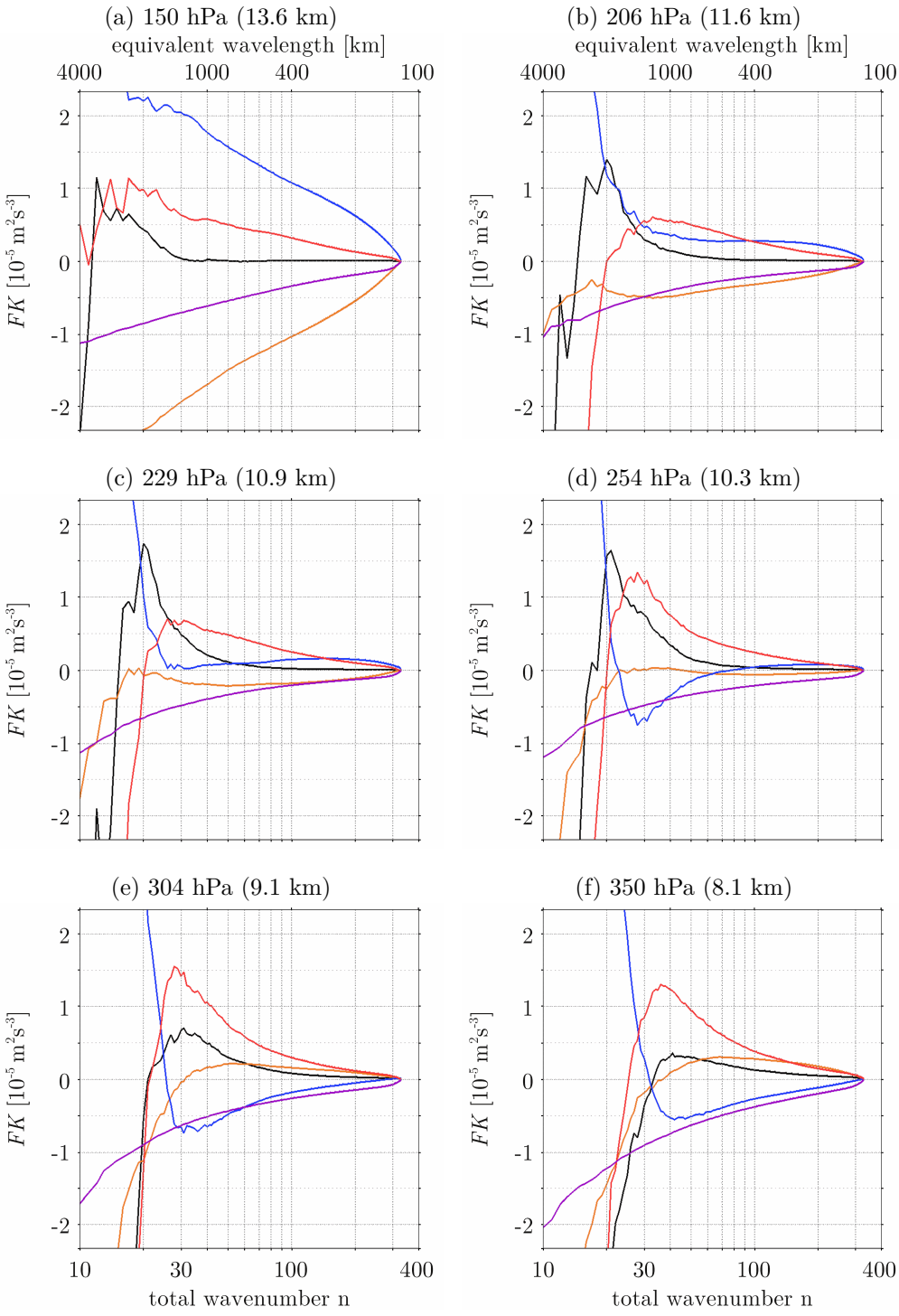

Fig. E.10: Upper tropospheric spectra of 2D energy flux (black) and non-2D energy fluxes due to horizontal advection (red), adiabatic conversion (blue), vertical advection (orange) and total momentum diffusion (purple) between 150 hPa and 350 hPa, from KMCM T330L100, averaged over 17 days. Only total wavenumbers $n \geq 10$ are displayed and scaling of the y-axis is only 1/30 of Fig. E.8.

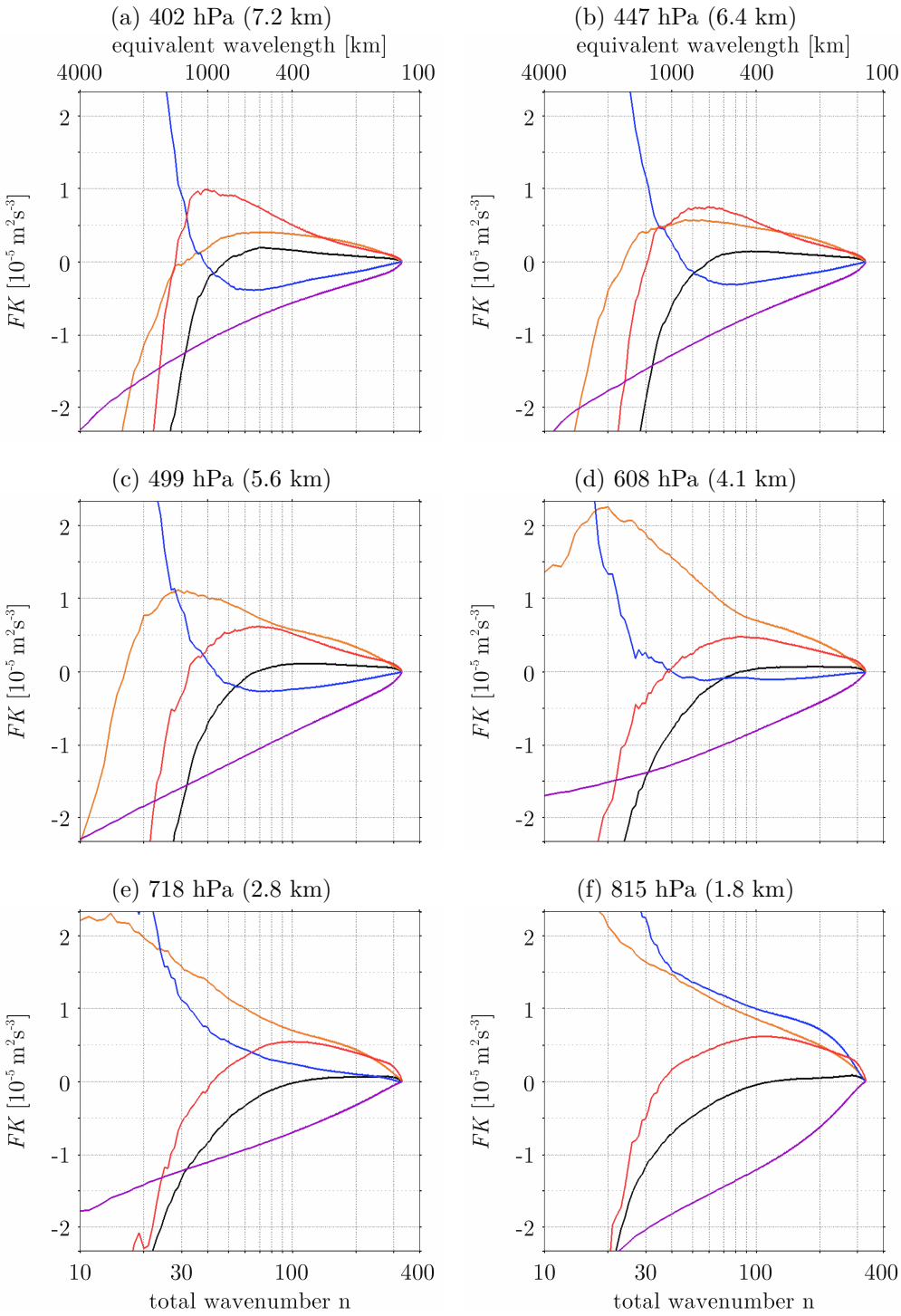

Fig. E.11: Same as Fig. E.10 but for middle and lower tropospheric levels from 402 hPa to 815 hPa.

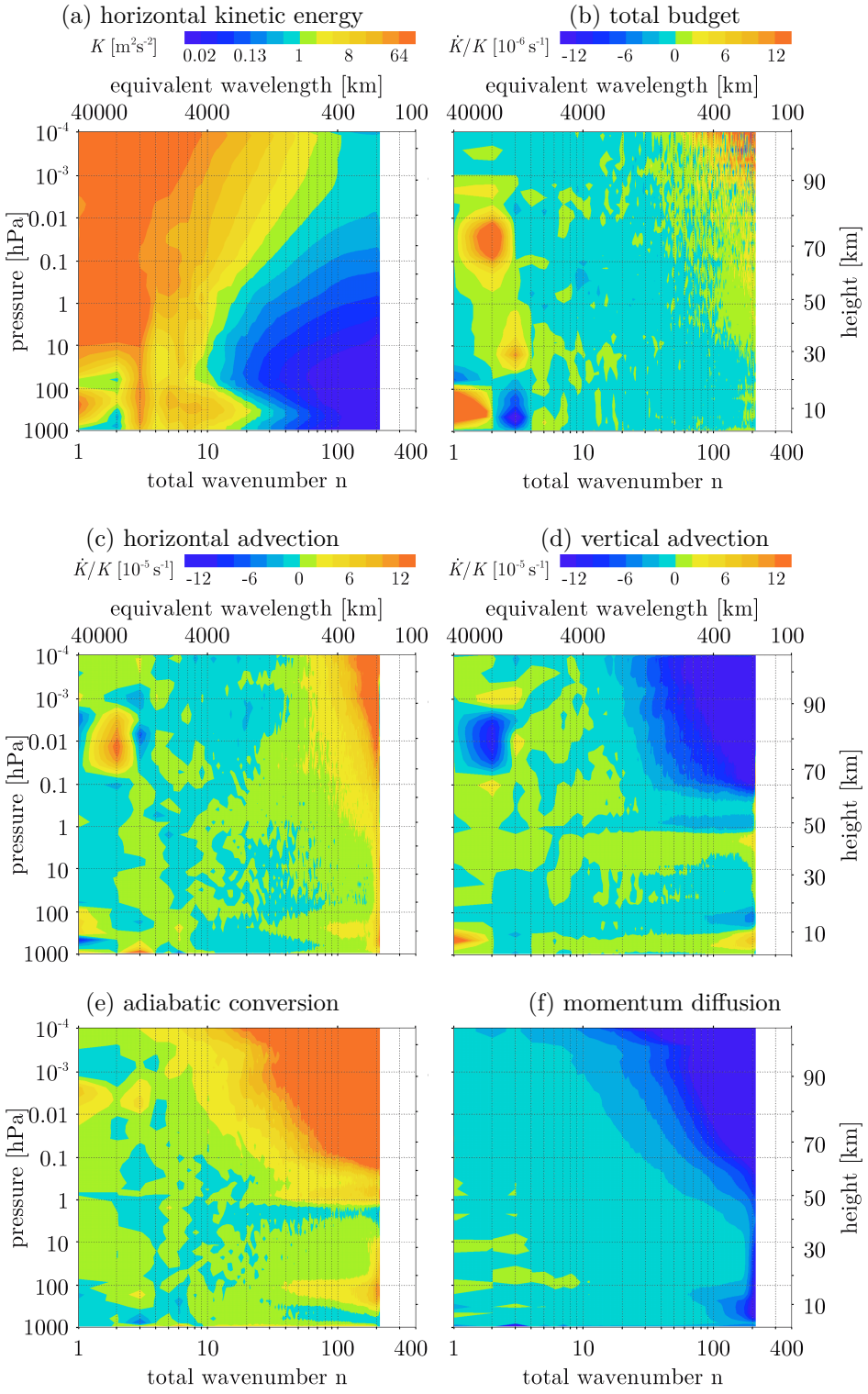

Fig. E.12: Vertical cross sections up to the lower thermosphere of (a) K_{ln}, (b)-(f) $\dot{K}_{ln}/K_{ln}$ and its contributions (all with the same color scale) according to (22) - (24), from KMCM T210L190, averaged over 16 days. Except for (a) the scales are 10 times the scales in Fig. E.1.

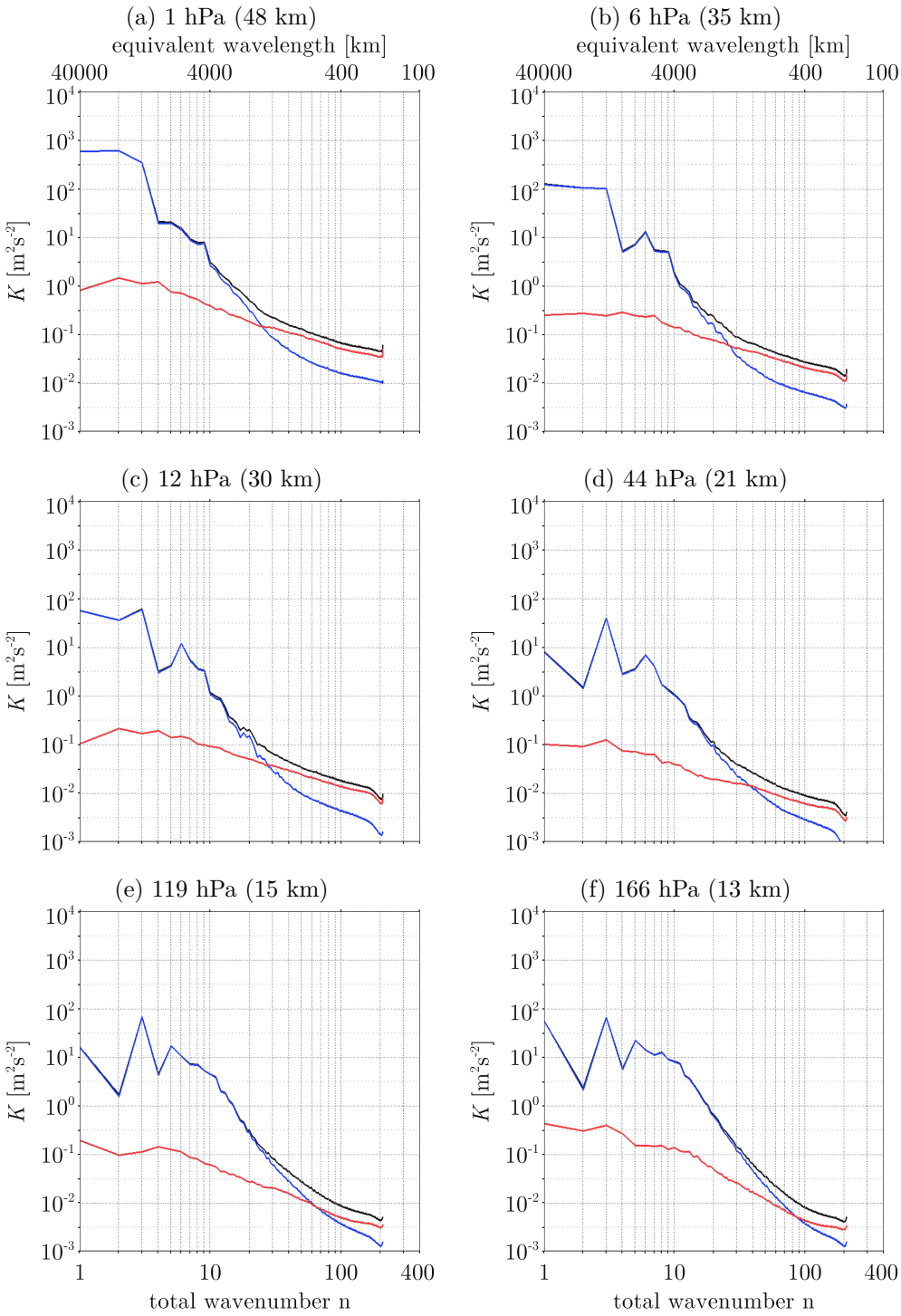

Fig. E.13: Stratospheric spectra of horizontal kinetic energy K_{ln} (black) and its rotational (blue) and divergent (red) components between 1 hPa (48 km) and 166 hPa (13 km), from KMCM T210L190, averaged over 16 days. The scaling of the y-axis is shifted up by 2 decades compared to Figs.E.2 and E.3.

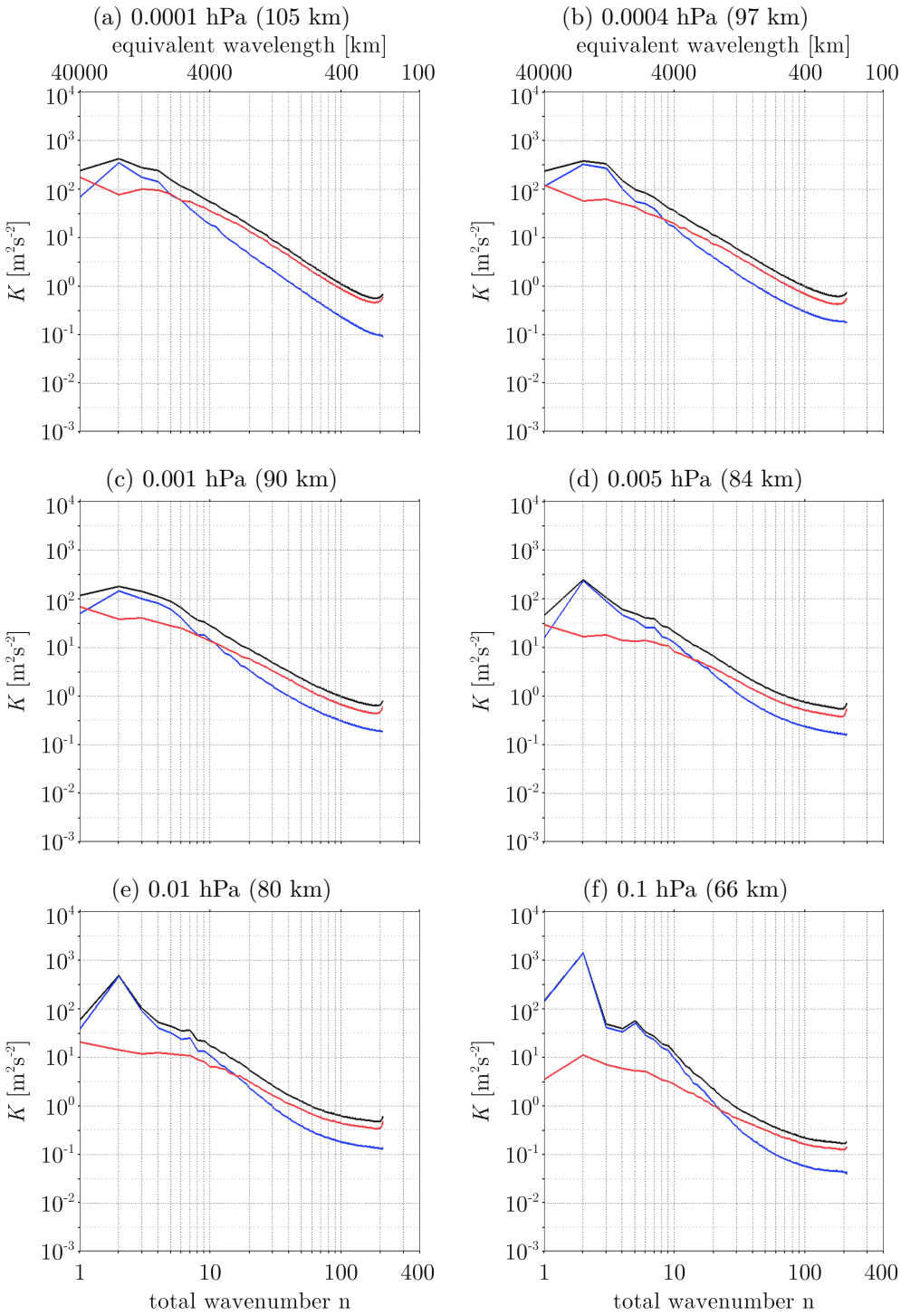

Fig. E.14: Same as Fig. E.13 but for lower thermospheric and mesospheric levels between 0.0001 hPa (105 km) and 0.1 hPa (66 km).

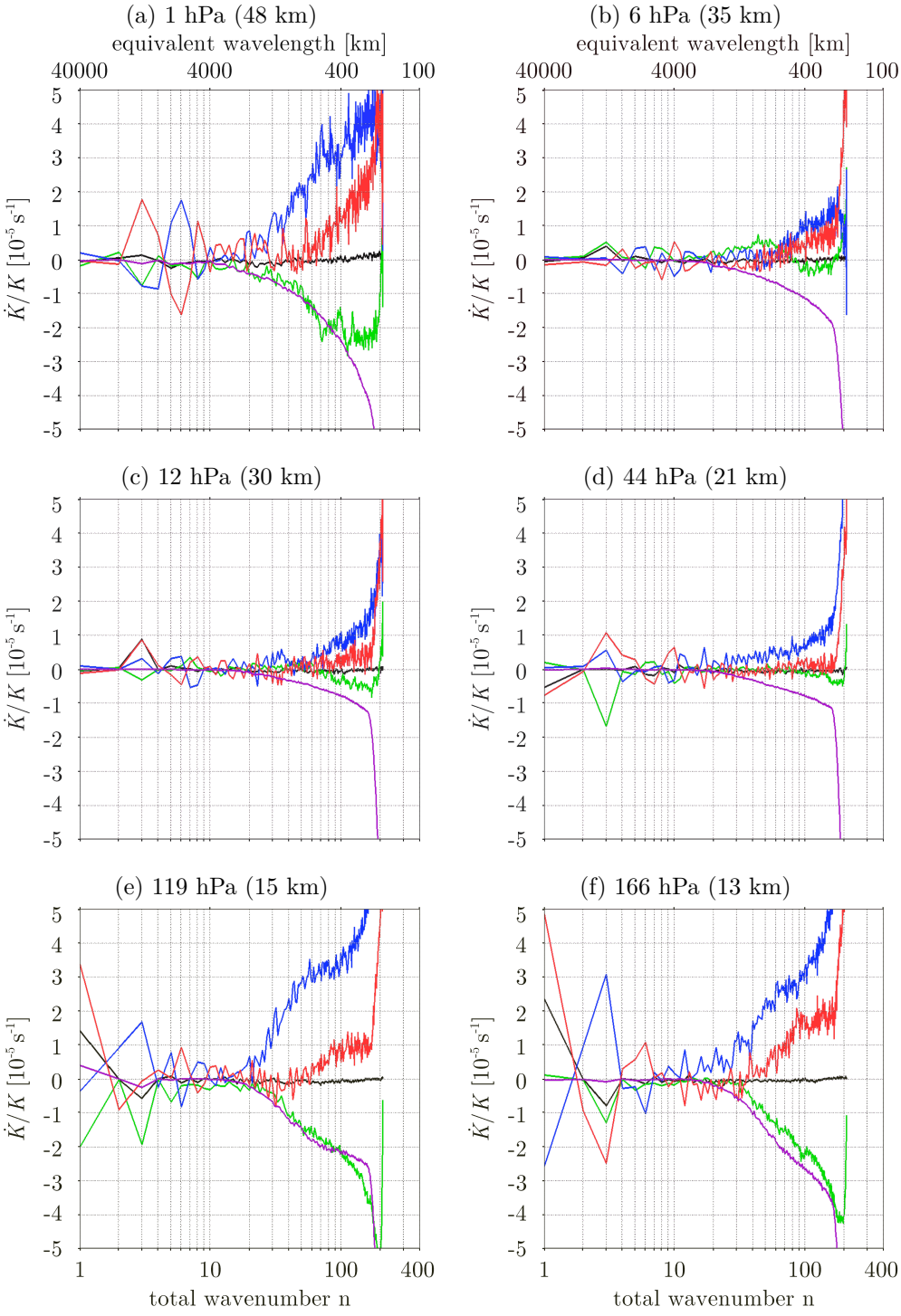

Fig. E.15: Stratospheric spectra of contributions to the normalized total budget of horizontal kinetic energy $\dot{K}_{ln}/K_{ln}$ (black curve) due to horizontal advection (red), vertical advection (green), adiabatic conversion (blue), and momentum diffusion (purple) between 1 hPa (48 km) and 166 hPa (13 km), from KMCM T210L190, averaged over 16 days, the scale is the same as in Figs.E.4 and E.5.

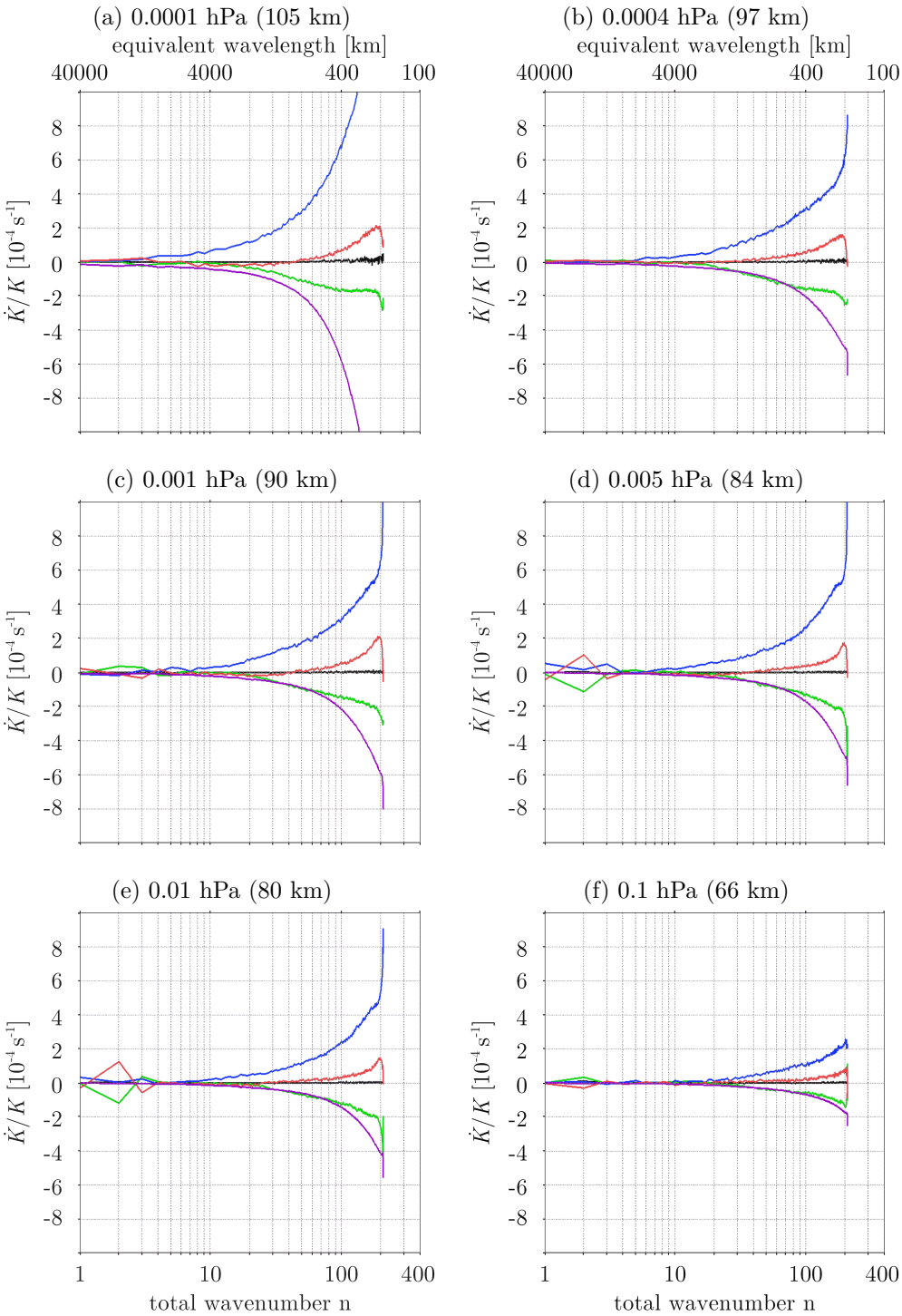

Fig. E.16: Same as Fig. E.15 but for lower thermospheric and mesospheric levels between 0.0001 hPa (105 km) and 0.1 hPa (66 km), the scale is 25 times the scale of Fig. E.15.

References

Achatz, U., 2007: Gravity-wave breaking: Linear and primary nonlinear dynamics. *Adv. Space Res.*, **40 (6)**, 719–733.

Adams, J. and P. Swarztrauber, 1997: Spherepack 2.0: A model development facility. Tech. rep., NCAR Technical Note NCAR/TN-436-STR.

Alexander, M. J., et al., 2010: Recent developments in gravity-wave effects in climate models and the global distribution of gravity-wave momentum flux from observations and models. *Q.J.R. Meteorol. Soc.*, **136 (650)**, 1103–1124.

Andrews, D. G., J. R. Holton, and C. B. Leovy, 1987: *Middle Atmosphere Dynamics*, International Geophysics Series, Vol. 40. Academic Press, 489 pp.

Baldwin, M. P. and T. J. Dunkerton, 2001: Stratospheric harbingers of anomalous weather regimes. *Science*, **294 (5542)**, 581–584.

Becker, E., 2001: Symmetric stress tensor formulation of horizontal momentum diffusion in global models of atmospheric circulation. *J. Atmos. Sci.*, **58 (3)**, 269–282.

Becker, E., 2003: *Energetics of turbulent momentum diffusion and gravity wave breakdown in general circulation models of the atmosphere*. IAP, Kühlungsborn, 108 pp.

Becker, E., 2004: Direct heating rates associated with gravity wave saturation. *J. Atmos. Sol. Terr. Phys.*, **66**, 683–696.

Becker, E., 2009: Sensitivity of the upper mesosphere to the Lorenz energy cycle of the troposphere. *J. Atmos. Sci.*, **66 (3)**, 647–666.

Becker, E., 2011: Dynamical control of the middle atmosphere. *Space Science Reviews*, **in press**, 1–32.

Becker, E. and U. Burkhardt, 2007: Nonlinear horizontal diffusion for GCMs. *Mon. Wea. Rev.*, **135**, 1439–1454.

Becker, E. and D. C. Fritts, 2006: Enhanced gravity-wave activity and interhemispheric coupling during the MaCWAVE/MIDAS northern summer program 2002. *Ann. Geophys.*, **24 (4)**, 1175–1188.

Berner, J., G. Shutts, and T. P. M. Leutbecher, 2009: A spectral stochastic kinetic energy backscatter scheme and its impact on flow-dependent predictability in the ecmwf ensemble prediction system. *J. Atmos. Sci.*, **66**, 603–626.

Billant, P. and J.-M. Chomaz, 2001: Self-similarity of strongly stratified inviscid flows. *Phys. Fluids*, **13**, 1645.

Blumen, W., 1978: Uniform potential vorticity flow: Part I. Theory of wave interactions and two-dimensional turbulence. *J. Atmos. Sci.*, **35 (5)**, 774–783.

Boer, G. and T. Shepherd, 1983: Large-scale two-dimensional turbulence in the atmopshere. *J. Atmos. Sci.*, **40**, 164–184.

Bronshtein, I. N., K. A. Semendyayev, G. Musiol, and H. Mühlig, 2007: *Handbook of Mathematics*. Springer Verlag, 1164 pp.

Brune, S. and E. Becker, 2012: Indications of stratified turbulence in a mechanistic GCM. *J. Atmos. Sci.*, **submitted**.

Charney, J. and P. Drazin, 1961: Propagation of planetary-scale disturbances from lower into the upper atmosphere. *J. Geophys. Res.*, **66**, 83–109.

Davies, L. A. and A. R. Brown, 2001: Assessment of which scales of orography can be credibly resolved in a numerical model. *Quart. J. Roy. Meteor. Soc.*, **127 (574)**, 1225–1237.

Dunkerton, T., 1979: On the mean meridional mass motions of the stratosphere and mesosphere. *J. Atmos. Sci.*, **35**, 2325–2333.

Eckermann, S. D., I. Hirota, and W. K. Hocking, 1995: Gravity wave and equatorial wave morphology of the stratosphere derived from long-term rocket soundings. *Q.J.R. Meteorol. Soc.*, **121 (521)**, 149–186.

Fleming, E. L., S. Chandra, J. J. Barnett, and M. Corney, 1990: Zonal mean temperature, pressure, zonal wind and geopotential height as functions of latitude. *Adv. Space Res.*, **10 (12)**, 11–59.

Fritts, D. and M. Alexander, 2003: Gravity wave dynamics and effects in the middle atmosphere. *Rev. Geophys.*, **41(1)**.

Fritts, D. C., L. Wang, and J. Werne, 2009: Gravity wave-fine structure interactions: A reservoir of small-scale and large-scale turbulence energy. *Geophys. Res. Lett.*, **36 (19)**, L19 805.

Fritts, D. C., et al., 2008: Gravity wave and tidal influences on equatorial spread F based on observations during the Spread F Experiment (SpreadFEx). *Ann. Geophys.*, **26 (11)**, 3235–3252.

Gill, A., 1982: *Atmosphere-Ocean Dynamics*, International Geophysics Series, Vol. 30. Academic Press, 679 pp.

Gkioulekas, E. and K. K. Tung, 2007: Is the subdominant part of the energy spectrum due to downscale energy cascade hidden in quasi-geostrophic turbulence? *Discrete and Continuous Dynamical Systems-Series B*, **7 (2)**, 293–314.

Goldberg, R. A., et al., 2006: The MaCWAVE program to study gravity wave influences on the polar mesosphere. *Ann. Geophys.*, **24 (4)**, 1159–1173.

Haltiner, G. J. and R. T. Williams, 1980: *Numerical Prediction and Dynamic Meteorology*. Wiley, 496 pp.

Hamilton, K., Y. Takahashi, and W. Ohfuchi, 2008: Mesoscale spectrum of atmospheric motions investigated in a very fine resolution global general circulation model. *J. Geophys. Res.*, **113**, D18 110, 19 pages.

Hecht, J. H., C. Fricke-Begemann, R. L. Walterscheid, and J. Höffner, 2000: Observations of the breakdown of an atmospheric gravity wave near the cold summer mesopause at 54N. *Geophys. Res. Lett.*, **27 (6)**, 879–882.

Held, I. M., R. T. Pierrehumbert, S. T. Garner, and K. L. Swanson, 1995: Surface quasi-geostrophic dynamics. *J. Fluid Mech.*, **282**, 1–20.

Hines, C., 1960: Internal atmospheric gravity waves at ionospheric heights. *Can. J. Phys*, **38**, 1441–1481.

Kolmogorov, A. N., 1941: Die lokale Struktur der Turbulenz in einer inkompressiblen zähen Flüssigkeit bei sehr großen Reynoldsschen Zahlen. *Sammelband zur statistischen Theorie der Turbulenz*, Akademie-Verlag, 1958, 71–76.

Koshyk, J., B. Boville, K. Hamilton, E. Manzini, and K. Shibata, 1999a: Kinetic energy spectrum of horizontal motions in middle-atmosphere models. *J. Geophys. Res.*, **104**, 27 177–27 190.

Koshyk, J. and K. Hamilton, 2001: The horizontal kinetic energy spectrum and spectral budget simulated by a high-resolution troposphere-stratosphere-mesosphere GCM. *J. Atmos. Sci.*, **68**, 329–348.

Koshyk, J., K. Hamilton, and J. Mahlmann, 1999b: Simulation of the $k^{-5/3}$ mesoscale spectral regime in the GFDL SKYHI general circulation model. *Geophys. Res. Lett.*, **26**, 843–846.

Kraichnan, R., 1967: Inertial ranges in two-dimensional turbulence. *Phys. Fluids*, **10**, 1417–1423.

Körnich, H., G. Schmitz, and E. Becker, 2006: The role of stationary waves in the maintenance of the northern annular mode as deduced from model experiments. *J. Atmos. Sci.*, **63 (11)**, 2931–2947.

Lander, J. and B. J. Hoskins, 1997: Believable scales and parameterizations in a spectral transform model. *Mon. Wea. Rev.*, **125 (2)**, 292–303.

Li, T., C.-Y. She, H.-L. Liu, and M. T. Montgomery, 2007: Evidence of a gravity wave breaking event and the estimation of the wave characteristics from sodium lidar observation over Fort Collins, CO (41°N, 105°W). *Geophys. Res. Lett.*, **34 (5)**, L05 815.

Lindborg, E., 2006: The energy cascade in a strongly stratified fluid. *J. Fluid Mech.*, **550**, 207–242.

Lindborg, E., 2009: Two comments on the surface quasigeostrophic model for the atmospheric energy spectrum. *J. Atmos. Sci.*, **66 (4)**, 1069–1072.

Lindzen, R., 1981: Turbulence and stress owing to gravity wave and tidal breakdown. *J. Geophys. Res.*, **86**, 9707–9714.

Lorenz, E., 1955: Available potential energy and the maintenance of the general circulation. *Tellus*, **7**, 157–167.

Nappo, C., 2002: *An Introduction to Atmospheric Gravity Waves*, International Geophysics Series, Vol. 85. Academic Press, 279 pp.

Nastrom, G. and K. Gage, 1985: A climatology of atmospheric wavenumber spectra of wind and temperature observed by commercial aircraft. *J. Atmos. Sci.*, **42**, 950–960.

Nastrom, G., K. Gage, and W. Jasperson, 1984: Kinetic energy spectrum of large- and mesoscale atmospheric processes. *Nature*, **310**, 36–38.

O'Sullivan, D. and T. J. Dunkerton, 1995: Generation of inertia gravity waves in a simulated life cycle of baroclinic instability. *J. Atmos. Sci.*, **52 (21)**, 3695–3716.

Preusse, P., S. Eckermann, J. Oberheide, M. Hagan, and D. Offermann, 2001: Modulation of gravity waves by tides as seen in CRISTA temperatures. *Adv. Space Res.*, **27 (10)**, 1773–1778.

Preusse, P., et al., 2006: Tropopause to mesopause gravity waves in August: measurement and modeling. *J. Atmos. Sol. Terr. Phys.*, **68**, 1730–1751.

Rapp, M., B. Strelnikov, A. Müllemann, F.-J. Lübken, and D. C. Fritts, 2004: Turbulence measurements and implications for gravity wave dissipation during the MaCWAVE/MIDAS rocket program. *Geophys. Res. Lett.*, **31 (24)**, L24S07.

Richardson, L. F., 1922: *Weather Prediction by numerical process.* University Press, 236 pp.

Riley, J. J. and E. Lindborg, 2008: Stratified turbulence: A possible interpretation of some geophysical turbulence measurements. *J. Atmos. Sci.*, **65 (7)**, 2416–2424.

Senf, F. and U. Achatz, 2011: On the impact of middle-atmosphere thermal tides on the propagation and dissipation of gravity waves. *J. Geophys. Res.*, **in press**.

Shaw, T. A. and E. Becker, 2011: Comments on "A spectral parameterization of drag, eddy diffusion, and wave heating for a three-dimensional flow induced by breaking gravity waves". *J. Atmos. Sci.*, **68 (10)**, 2465–2469.

Simmons, A. and D. Burridge, 1981: An energy and angular momentum conserving vertical finite-difference scheme and hybrid vertical coordinates. *Mon. Wea. Rev.*, **109**, 758–766.

Smagorinsky, J., 1963: General circulation experiments with the primitive equations. *Mon. Wea. Rev.*, **91 (3)**, 99–164.

Straus, D. and P. Ditlevsen, 1999: Two-dimensional turbulence properties of the ECMWF reanalyses. *Tellus*, **51A**, 749–772.

Takahashi, Y., K. Hamilton, and W. Ohfuchi, 2006: Explicit global simulation of the mesoscale spectrum of atmospheric motions. *Geophys. Res. Lett.*, **33**, L12 812.

Tulloch, R. and K. S. Smith, 2009: Quasigeostrophic turbulence with explicit surface dynamics: Application to the atmospheric energy spectrum. *J. Atmos. Sci.*, **66 (2)**, 450–467.

Tung, K. K. and W. W. Orlando, 2003: The k^{-3} and $k^{-5/3}$ energy spectrum of atmospheric turbulence: Quasigeostrophic two-level model simulation. *J. Atmos. Sci.*, **60**, 824–835.

Waite, M. L. and P. Bartello, 2004: Stratified turbulence dominated by vortical motion. *J. Fluid Mech.*, **517**, 281–308.

Washington, W. and C. Parkinson, 2005: *An Introduction to Three-Dimensional Climate Modeling*. University Science Books, 368 pp.

Watanabe, S., Y. Kawatani, Y. Tomikawa, K. Miyazaki, M. Takahashi, and K. Sato, 2008: General aspects of a T213L256 middle atmosphere general circulation model. *J. Geophys. Res.*, **113 (D12)**, D12 110.

Wu, D. L., P. Preusse, S. D. Eckermann, J. H. Jiang, M. de la Torre Juarez, L. Coy, and D. Y. Wang, 2006: Remote sounding of atmospheric gravity waves with satellite limb and nadir techniques. *Adv. Space Res.*, **37 (12)**, 2269–2277.